



저작자표시-비영리-변경금지 2.0 대한민국

이용자는 아래의 조건을 따르는 경우에 한하여 자유롭게

- 이 저작물을 복제, 배포, 전송, 전시, 공연 및 방송할 수 있습니다.

다음과 같은 조건을 따라야 합니다:



저작자표시. 귀하는 원저작자를 표시하여야 합니다.



비영리. 귀하는 이 저작물을 영리 목적으로 이용할 수 없습니다.



변경금지. 귀하는 이 저작물을 개작, 변형 또는 가공할 수 없습니다.

- 귀하는, 이 저작물의 재이용이나 배포의 경우, 이 저작물에 적용된 이용허락조건을 명확하게 나타내어야 합니다.
- 저작권자로부터 별도의 허가를 받으면 이러한 조건들은 적용되지 않습니다.

저작권법에 따른 이용자의 권리는 위의 내용에 의하여 영향을 받지 않습니다.

이것은 [이용허락규약\(Legal Code\)](#)을 이해하기 쉽게 요약한 것입니다.

[Disclaimer](#)

공학박사 학위논문

The growth behavior of thin-
film 2D TMDs materials and its
applications for future
electronics

이차원 전이금속 디칼코제나이드 박막물질의
성장거동과 미래전자소자로의 응용

2021 년 1 월

서울대학교 대학원

재료공학부 재료공학전공

한 상 섭

The growth behavior of thin-
film 2D TMDs materials and its
applications for future
electronics

- 이차원 전이금속 디칼코제나이드 박막물질
의 성장거동과 미래전자소자로의 응용 -

지도교수 오 규 환

이 논문을 공학박사 학위논문으로 제출함
2021년 1월

서울대학교 대학원
재 료 공 학
한 상 섭

한상섭의 박사 학위논문을 인준함

2020년 12월

위 원 장	이 관 형	(인)
부위원장	오 규 환	(인)
위 원	선 정 윤	(인)
위 원	정 연 응	(인)
위 원	정 희 석	(인)

Abstract

The Growth Behavior of Thin-Film 2D TMDs Materials and Its Applications for Future Electronics

Sang Sub Han

Material Science and Engineering

The Graduate School

Seoul National University

Two-dimensional (2D) transition-metal dichalcogenides (TMDs) in the form of MX_2 (M: transition metals, X: chalcogens) have drawn substantive scientific interests owing to their extraordinary structural and physical properties. Particularly, platinum (Pt)-based 2D chalcogenides present various appealing aspects absent in conventional 2D TMDs, including thickness-dependent semiconducting-to-metallic transition, superior air stability, and low synthesis temperature. Such properties of electrical property transition are known for related to the structure of the 2D TMDs layers. Despite much-devoted efforts, scalable and controllable synthesis of large-area 2D Pt-based 2D chalcogenides with well-defined layer orientation has not been established, leaving its projected structure–property relationship largely unclarified.

The extremely small thickness coupled with extraordinary electrical and

optical properties of 2D TMDs layer put it the best candidate of emerging stretchable and foldable electronics recently. Although intrinsically large strain limits are projected in them (i.e., several times greater than silicon), integrating 2D TMDs in their pristine forms does not realize superior mechanical tolerance greatly demanded in high-end stretchable and foldable devices of unconventional form factors.

The work described in this thesis focuses on understanding the synthesis of large area 2D TMDs layer, especially 2D PtSe₂ and PtTe₂ layers of interest for growth behavior related to their structural and electrical properties. This dissertation also covers a versatile and rational strategy to convert 2D TMDs of limited mechanical tolerance to tailored three-dimensional (3D) structures with extremely large mechanical stretchability accompanying well-preserved electrical integrity and modulated transport properties, through the transfer/integration and kirigami/serpentine patterning techniques.

In the first part, we investigate the structural evolution of large-area chemical vapor transition (CVT)-grown 2D PtSe₂ and PtTe₂ layers of tailored morphology and clarify its influence on resulting electrical properties. Specifically, we unveil the coupled transition of structural–electrical properties in 2D TMDs layers grown at a low temperature (i.e., 400 °C). The layer orientation of 2D PtSe₂ and PtTe₂ grown by the CVD selenization and tellurization of seed Pt films exhibits horizontal-to-vertical transition with increasing of Pt thickness. These growth transitions of PtSe₂ and PtTe₂ layers are a consequence of competing thermodynamic and kinetic factors dictated by accumulating internal strain. The exclusive role of the strain on dictating 2D

layer orientation has been quantitatively verified by the transmission electron microscopy (TEM) strain mapping analysis.

In the second part, we report two novel strategies to delaminate and integrate wafer-scale 2D TMDs layers of well-defined components and orientations using water. First, we report a generic and reliable strategy to achieve the layer-by-layer integration of large-area 2D TMDs and their heterostructure variations onto a variety of unconventional substrates. This new 2D layer integration method employs water only without involving any other chemicals, thus renders distinguishable advantages over conventional approaches in terms of material property preservation and integration size scalability. Second, we directly grew a variety of 2D TMDs layers on “water-dissoluble” single-crystalline salt wafers and precisely delaminated them inside water in a chemically benign manner. This manufacturing strategy enables the automated integration of vertically aligned 2D TMDs layers as well as 2D/2D hetero layers of arbitrary stacking orders on exotic substrates insensitive to their kind and shape. The original salt wafers can be recycled for additional growths, confirming high process sustainability and scalability. The generality and versatility of this approach have been demonstrated by developing proof-of-concept “all 2D” devices for diverse yet unconventional applications. These studies are believed to shed a light on leveraging opportunities of 2D TMDs layers toward achieving large-area mechanically reconfigurable devices of various form factors at the industrially demanded scale.

Lastly, we report a versatile and rational strategy to convert 2D TMDs of limited mechanical tolerance to tailored 3D structures with extremely large

mechanical stretchability accompanying well-preserved electrical integrity and modulated transport properties. We employed a concept of strain engineering inspired by paper-cutting arts, known as kirigami patterning and serpentine patterning, and developed 2D TMDs-based stretchable electronics. The vertically aligned metallic PtTe₂ and PtSe₂ layers were employed for the high-performance electronic heaters and high-stretchable (over 2000% stretch) conductors using our low-temperature direct growth method on polymeric substrates. The semiconducting PtSe₂ and MoS₂ layer were employed for large-area stretchable field-effect transistor (FET) electronic device and NO₂ gas sensor showing high-performance of sensitivity. These multifunctional 2D materials in unconventional yet tailored 3D forms are believed to offer vast opportunities for emerging electronics and optoelectronics.

Keywords: 2D TMDs layer, chemical vapor transition, layer orientation transition, water-assisted transfer, salts substrate, stretchable electronics, kirigami pattern, serpentine pattern

Student Number: 2013-20631

Table of Contents

Abstract	I
Table of Contents	V
List of Figures	XIII
Chapter 1. Introduction	1
1.1. Introduce of 2D TMDs Materials	1
1.2. Structure of 2D TMDs Layers.....	4
1.2.1. Atomic Structure of 2D TMDs Layers.....	4
1.2.2. Growth Orientation of 2D TMDs Layers	8
1.3. Transfer and Integration of 2D TMDs Layer	9
1.4. Engineering the Structure of 2D TMDs to be Mechanically Reconfigurable... ..	10
1.4.1. 3D texturing based on pre-structured polymeric templates.....	11
1.4.2. Strain engineering of large-area 2D TMDs by origami and kirigami patterning.	12
1.5. Reference	14
Chapter 2. Growth Behavior and its Properties of 2D TMDs Layers	20
2.1. Growth Behavior and Properties of 2D PtSe ₂ Layers	20
2.1.1. Introduction	20
2.1.2. Experimental Section	22
2.1.2.1. 2D PtSe ₂ Layer Growth	22
2.1.2.2. TEM/STEM Characterization.....	23
2.1.2.3. Raman Characterization	23

2.1.2.4. Device Fabrication and Electrical Measurement	23
2.1.2.5. DFT Calculation	24
2.1.2.6. XPS Characterization	24
2.1.3. Results and Discussion.....	25
2.1.3.1. Orientation Controlled Growth of PtSe ₂ Layers	25
2.1.3.2. Atomic-scale Structural Analysis of Orientation Transition.....	29
2.1.3.3. Chemical and Electronic Structures of 2D PtSe ₂ Layers	32
2.1.3.4. DFT calculation of various morphology and orientation 2D PtSe ₂	38
2.1.3.5. The Growth Mechanism of Horizontal-to-vertical 2D Layer Transition in PtSe ₂ Layer	41
2.1.4. Conclusion.....	44
2.1.5. Reference.....	44
2.2. Growth Behavior and Properties of 2D PtTe ₂ Layers	50
2.2.1. Introduction	50
2.2.2. Experimental Method	52
2.2.2.1. Synthesis of 2D PtTe ₂ Layers	52
2.2.2.2. TEM Characterization and Analysis.....	53
2.2.2.3. XRD Characterization	53
2.2.2.4. Electrical Characterization	54
2.2.2.5. AFM Characterization	54

2.2.2.6. Computational Details	54
2.2.3. Results and Discussion	55
2.2.3.1. Growth and Structural Analysis of PtTe ₂ Layers	55
2.2.3.2. Orientation Controlled Growth and the Mechanism of Orientation Transition of PtTe ₂ Layers	58
2.2.3.3. DFT calculation for various morphology and orientation of 2D PtTe ₂ Layers	71
2.2.3.4. Electronic Structures of 2D PtTe ₂ Layers	74
2.2.4. Conclusion.....	79
2.2.5. Reference.....	79
Chapter 3. Transfer and Integration of 2D TMDs Layers	85
3.1. Water-assisted Transfer method for 2D TMDs Layers.....	85
3.1.1. Introduction	85
3.1.2. Experimental Method	87
3.1.2.1. Synthesis of 2D TMDs Films	87
3.1.2.2. Structural Characterization	87
3.1.3. Results and Discussion.....	88
3.1.3.1. Procedure of Water-assisted 2D TMDs Layer Integration	88
3.1.3.2. Demonstration of Water-assisted 2D TMDs Layer Transfer and Integration	91
3.1.3.3. Principle of Water-assisted 2D TMDs Layer Separation	94

3.1.4. Conclusion.....	99
3.1.5. Reference.....	99
3.2. Water Dissoluble Salt Substrates for 2D TMDs Layer.....	103
3.2.1. Introduction	103
3.2.2. Experimental Section	104
3.2.2.1. Growth of 2D TMD Layers	104
3.2.2.2. Delamination and Integration of 2D TMD Layers	105
3.2.2.3. Structural and Chemical Characterization.....	106
3.2.3. Results and Discussion.....	106
3.2.3.1. The Manufacturing Process of the Water-assisted.....	106
3.2.3.2. Structural and Chemical Analysis of 2D TMDs Layer grown on Salt Substrates	110
3.2.3.3. The Diversity of Salt Substrates for 2D TMDs Growth and Delamination.....	113
3.2.3.4. The Heterogeneous Integration of Multiple 2D TMDs Layers	116
3.2.4. Conclusion.....	119
3.2.5. Reference.....	119
Chapter 4. Application to Stretchable Future Electronics.....	125
4.1. High Stretchable Electronic Device	125
4.1.1. Introduction	125
4.1.2. Experimental Method	127
4.1.2.1. Preparation of a Kirigami-Patterned PI Substrate	127

4.1.2.2. Two-Dimensional PtSe ₂ Layer Growth	128
4.1.2.3. Electrical and Optoelectrical Characterization	128
4.1.2.4. XPS and TEM/STEM Characterization.....	129
4.1.3. Results and Discussion.....	129
4.1.3.1. The Manufacturing Process of High Stretchable 2D PtSe ₂ /PI Kirigami Device	129
4.1.3.2. Structural and Chemical Analysis of 2D PtSe ₂ Layers	132
4.1.3.3. The Mechanical Properties of 2D PtSe ₂ /PI Device ...	135
4.1.3.4. FEM Simulation for the Optimization of Device Design	140
4.1.3.5. Stretchable FET Device of 2D PtSe ₂ /PI Layer	144
4.1.4. Conclusion.....	147
4.1.5. Reference.....	147
4.2. Stretchable Electronic Heater of 2D PtTe ₂ Layers	152
4.2.1. Introduction	152
4.2.2. Experimental Method.....	154
4.2.2.1. 2D PtTe ₂ Synthesis	154
4.2.2.2. Crystal Structure Characterization.....	155
4.2.2.3. Raman and Electrical Characterization	155
4.2.2.4. Heating performance Test.....	156
4.2.2.5. Kirigami-pattern Fabrication and Finite Element Method	156

4.2.3. Results and Discussion.....	157
4.2.3.1. 2D PtTe ₂ Layer Growth	157
4.2.3.2. Electrical and electrothermal properties of 2D PtTe ₂ layer	160
4.2.3.3. Flexibility of 2D PtTe ₂ Layer on PI Substrate	167
4.2.3.4. Kirigami-patterned stretchable heater based on 2D PtTe ₂	170
4.2.4. Conclusion.....	175
4.2.5. Reference.....	175
4.3. Stretchable High-Performance Gas Sensor	179
4.3.1. Introduction	179
4.3.2. Experimental Method	181
4.3.2.1. CVD Growth of VA-2D MoS ₂ Layers.....	181
4.3.2.2. VA-2D MoS ₂ Layer Transfer and Integration Process	181
4.3.2.3. AFM, UV–Vis, Raman, XPS, and TEM Characterizations	182
4.3.2.4. Device Fabrication and Electrical/Optical Characterization.....	182
4.3.2.5. Gas Sensing Characterization.....	182
4.3.2.6. FEM Simulation and DFT Calculation.....	183
4.3.3. Results and Discussion.....	184
4.3.3.1. The Sequential Growth, Integration, and Patterning Process of the VA-2D MoS ₂ Layers	184

4.3.3.2. Structural and Chemical Analysis of 2D VA-MoS ₂ Layers	188
4.3.3.3. Gas Sensing Performance of Serpentine VA-MoS ₂ Layers	192
4.3.3.4. FEM Simulation for Mechanical Stretching.....	198
4.3.3.5. DFT Calculations for the Superiority of VA-2D MoS ₂ Layers for NO ₂ Gas Sensing.....	201
4.3.4. Conclusion.....	205
4.3.5. Reference.....	205
Chapter 5. Total Conclusion.....	212
Abstract in Korean.....	215

List of Tables

Table 1. 1. Electronic and structural properties of different layered TMDs

Table 2. 1. Room-temperature conductivity values for horizontally-aligned 2D PtTe₂ layers synthesized via various approaches and other representative conductive 2D TMDCs.

Table 4. 1. Comparison of the electrothermal performance and the flexibility with the recently developed nanomaterial-based wear-able heaters

List of Figures

Figure 1.1. Illustration of 2D layer materials and examples of flexible smart systems.

Figure 1.2. (a) Typical structures of layered transition metal dichalcogenides. Cleavable 2H, 1T and 1T' structures in layered TMD are shown. (b) Bandgap of 2D layered materials varying from zero band gap of graphene (white color) to wide bandgap of hBN. The color in the column is presenting the corresponding wavelength of bandgap.

Figure 2.1. (a) Photograph of as-grown 2D PtSe₂ layers-on-SiO₂/Si substrates prepared with Pt of the noted thicknesses. (b–e) TEM characterization of 2D PtSe₂ layers grown with Pt of (b) 0.75 (c) 3 (d) 6, and (e) 10 nm. (f) EDS profiles obtained from 2D PtSe₂ layers prepared with 0.75 nm (top) and 10 nm (bottom) Pt seeds. (g) Coverage ratio of vertically aligned 2D PtSe₂ layers as a function of Pt thickness.

Figure 2. 2. (a–c) TEM/STEM characterization of horizontally aligned 2D PtSe₂ layers prepared with Pt of 0.75 nm; (a) low-magnification TEM. (b) HR-STEM. (c) Cross-sectional TEM. (d–f) TEM/STEM characterization of vertically aligned 2D PtSe₂ layers prepared with Pt of 8 nm; (d) low-magnification TEM. (e) HR-STEM. (f) Cross-sectional TEM.

Figure 2. 3. (a) Raman profiles of 2D PtSe₂ layers prepared with Pt seeds of various thicknesses. (b) Raman peak position difference as a function of Pt thickness. (c) Raman peak intensity ratio as a function of Pt thickness. (d) Plots of R vs V_{bg} obtained from 2D PtSe₂ FETs with varying Pt thicknesses. (e) Plots of the current ratio obtained at V_{bg} = ±60 V and conductance determined at V_{bg} = 0 V as a function of Pt thickness. (f) I_{ds}-V_{ds} characteristics under varying V_{bg} (step of 40 V) obtained from horizontally aligned 2D PtSe₂ layers. (g) I_{ds}-V_{bg} characteristics obtained at V_{ds} = 10 mV from the sample corresponding to (f).

Figure 2. 4. Electronic band structures and PDOSs of PtSe₂ of various structures. (a) 2D monolayer vs bulk. (b-d) Vertically aligned 2D layers of various layer lengths of (b) 7.9 (c) 10 (d) 20 Å. Vacuum of ~10 Å was inserted above the vertically aligned 2D PtSe₂ layers

Figure 2. 5. Illustration of two different growth scenarios for 2D PtSe₂ layers; (a,b) horizontally aligned 2D PtSe₂ layers grown by the selenization of thin Pt seed layers. (a) Selenization of discontinuous Pt nanoclusters. (b) Plane-view TEM image of discontinuous Pt nanoclusters deposited on an amorphous carbon film. (c) Corresponding HRTEM image revealing crystalline Pt nanoclusters (red circles). (d) Growth of 2D PtSe₂ horizontally expanding layers filling in the free volumes in between Pt nanoclusters. (e) Vertical growth of 2D PtSe₂ layers by selenizing

physically confined Pt nanoclusters of large thickness

Figure 2. 6. (a) Perspective (left), side (mid), and top (right) views of 1T-PtTe₂. Orange and blue balls represent Te and Pt atoms, respectively. The pink-shaded areas in the side and top views illustrate an octahedron atomic configuration. (b) Schematic illustration of the 2D PtTe₂ layer growth apparatus and procedure. (c) Camera image of a PtTe₂ sample on a SiO₂/Si wafer with a size of 1 cm × 6 cm. (d) Plane-view HAADF-STEM image of a 2D PtTe₂ basal plane. (e) Intensity profile corresponding to the red line in (d). (f) Cross-sectional HAADF-STEM image of 2D PtTe₂ layers with an interlayer spacing of 0.52 nm. (g) Representative cross-sectional STEM image of large-area, horizontally aligned 2D PtTe₂ multilayers. (h) EDS spectrum revealing a stoichiometry of Pt/Te = 1:2.

Figure 2. 7. (a–c): Schematics for growth characteristics of 2D PtTe₂ layers obtained by tellurizing (a) scattered Pt nanoclusters, (b) dense Pt nanoclusters, and (c) continuous Pt films. The mid and bottom rows of (a, b, and c) represent projected and side-views of resulting 2D PtTe₂ layers, respectively. (d–f): HAADF-STEM images of (d) holey layers with the pores indicated by the red arrow, (e) continuous layers, and (f) continuous layers with pronounced imaging contrast. (g–i): High-resolution HAADF-STEM images of (g) (110) lattice fringes in crystalline grains with a grain

boundary, (h) (110) lattice fringes from crystalline 2D basal planes of three distinct orientations, and (i) (001) lattice fringes denoting 2D layer vertical orientation. (j–l): Cross-sectional STEM images of (j) edge-terminated horizontally aligned 2D layers, (k) reorientation of 2D layers along with the top and bottom insets corresponding to the blue and red boxed regions, and (l) vertically aligned 2D layers along with the inset corresponding to the green boxed region. The scale bars of the insets are 1 nm.

Figure 2. 8. (a) DF-STEM image (left) and corresponding FFT pattern (right) of horizontally aligned 2D PtTe₂ multilayers constituting three crystalline grains composed of basal planes with distinct orientations. The blue, cyan, and pink-shaded spots in the FFT correspond to the grains denoted by the identical color in the DF-STEM image. The black squared diffraction spots in the FFT originate from the layer underneath the grains of A, B, and C. (b–d) GPA mapping and corresponding FFTs of grain boundaries formed by grains of (b) A + B, (c) C + A, and (d) B + C. The white dashed squares in (b–d) denote the dislocation cores exhibiting high strain.

Figure 2. 9. (a) XRD characterization of 2D PtTe₂ layers grown from Pt films of varying thickness. The red star mark denotes peaks from the growth substrate. (b) XRD peak intensity ratio of I(101)/I(001) as a function of Pt film thickness. (c) Representative STEM image of

crystalline grains constituting horizontally aligned 2D PtTe₂ layers. (d) Corresponding SAED pattern indicating that the indexed diffraction rings are normal to the [001] zone axis. (e) Representative STEM image of crystalline grains constituting a mixture of horizontally and vertically aligned 2D PtTe₂ layers. (f) Corresponding SAED pattern indicating a presence of both [001] and [101] zone axes. The blue highlighted diffraction rings correspond to those presented in (d), highlighting the crystallographic distinction of horizontally vs. vertically aligned 2D PtTe₂ layers

Figure 2. 10. (a) Side view of penta-layer (5L) PtTe₂ as a representative system for horizontally aligned multilayers. (b) Electronic band structure and DOS plots for 3L–6L. (c) Side view (top) and electronic band structures (bottom) of vertically aligned 2D PtTe₂ with Te-terminated edge configurations. (d) Side view (top) and electronic band structures (bottom) of vertically aligned 2D PtTe₂ with Pt-terminated edge configurations.

Figure 2. 11. (a) Thickness of 2D PtTe₂ layers as a function of Pt thickness. (b, c) Back-gate FET measurements of 2D PtTe₂ layers obtained from ~0.5 nm Pt thickness, showing (b) $I_{ds}-V_{ds}$ and (c) $I_{ds}-V_g$ transfer characteristics. (d) $I-V$ curves of 2D PtTe₂ prepared from various Pt thicknesses. (e) Conductance as a function of Pt thickness. (f) Conductivity as a function of Pt thickness showing a presence of

its thickness-dependent maximum point. The junction of the blue and red shading represents a transition of horizontal-to-vertical layer orientation. (g) Schematics of electron transports in horizontally vs. vertically aligned 2D PtTe₂ layers.

Figure 3. 1. Schematic to illustrate the water-assisted green integration of CVD-grown 2D TMD layers on arbitrary substrates

Figure 3. 2. (a) Image of 2D MoS₂ layers as-grown on SiO₂/Si and the corresponding cross-sectional HRTEM image. (b) Raman spectrum obtained from the 2D MoS₂ layers denoting their characteristic peaks. (c) Time-lapsed snapshot images to demonstrate the water-assisted spontaneous separation of 2D MoS₂ layers inside water. (d) Illustration of the water penetration process at the 2D MoS₂/SiO₂ interface along with the representative images of water contact angle measurements for 2D MoS₂ layers and SiO₂

Figure 3. 3. (a) Plane-view and (b) cross-sectional HRTEM images of vertically-aligned 2D MoS₂ layers grown on SiO₂. 2D MoS₂ layers are rooted in the SiO₂ surface (red highlight in (b)). (c) Cross-sectional HRTEM image of horizontally-aligned 2D MoS₂ layers grown on SiO₂. 2D basal planes are in contact with the SiO₂ surface. The inset shows a low magnification TEM image of the corresponding sample.

Figure 3. 4. Distinguishable characteristics of 2D MoS₂ layers on SiO₂

substrates upon water immersion when they are in two different surface states. (a) Pristine samples typically get submerged in water. (b) Aged samples yield the facile and spontaneous separation of 2D layers.

Figure 3. 5. (a,b) Schematic illustrations highlighting the feasibility of water-assisted delamination for (a) HA- and (b) VA-2D TMD layers, and their representative cross-sectional HRTEM images of 2D MoS₂ layers. The scale bars are 5 and 2.5 nm for (a,b), respectively. (c) Schematic illustration of stepwise processes for the water-assisted delamination and transfer of VA-2D TMD layers using salt crystals. (d) Representative images to highlight the sustainability of salt crystals throughout sequential steps of metal deposition, 2D TMD layers growth, and their delamination.

Figure 3. 6. (a) HRTEM image of VA-2D PtSe₂ layers delaminated from a NaCl substrate. The inset is the corresponding SAED pattern with indexed PtSe₂ crystalline planes. (b) Raman spectrum, (c) XPS spectra, and (d) EDS profile obtained from the same sample of delaminated VA-2D PtSe₂ layers. (e) HRTEM image of HA-2D PtSe₂ layers delaminated from a NaCl substrate. The inset is the corresponding low-magnification TEM image. (f) SAED pattern corresponding to the sample in (e). (g) EELS elemental map images obtained from the same sample.

Figure 3. 7. (a) HRTEM image of VA-2D PtSe₂ layers delaminated from a NaCl

substrate. The inset is the corresponding SAED pattern with indexed PtSe₂ crystalline planes. (b) Raman spectrum, (c) XPS spectra, and (d) EDS profile obtained from the same sample of delaminated VA-2D PtSe₂ layers. (e) HRTEM image of HA-2D PtSe₂ layers delaminated from a NaCl substrate. The inset is the corresponding low-magnification TEM image. (f) SAED pattern corresponding to the sample in (e). (g) EELS elemental map images obtained from the same sample.

Figure 3. 8. (a) Schematic illustration and working principle for the water-assisted automated integration of 2D TMD layers. (b) Top-to-bottom view of a home-built 2D layer integration stage describing its major components. (c) Time-lapsed snapshot images sequentially depicting the water-assisted automated integration of VA-2D PtTe₂ layers. (d) Heterogeneous integration of three-different VA-2D TMD layers on a PET substrate. The scale bar is 1 cm. (e) Mechanical flexibility of VA-2D TMD heterolayers. The sample is different from that in (d). (f) Raman spectral profiles obtained from a sample of 2D heterolayers composed of PtTe₂, MoS₂, and PtSe₂.

Figure 4. 1. Schematic of the fabrication processes for kirigami-patterned, vertically aligned 2D PtSe₂ layers on a flexible PI substrate.

Figure 4. 2. (a) Camera images showing a bare PI (left) and an as-grown 2D PtSe₂ layers-on-PI substrate prepared by the CVD selenization of

8 nm Pt (right). (b and c) XPS characterization of (b) Pt 4f and (c) Se 3d core levels obtained from 2D PtSe₂ layers on PI substrates. (d) Low-magnification plane-view TEM image of 2D PtSe₂ layers isolated from their PI growth substrates. (e) SAED indexing, (f) EDS spectrum profile, and (g) EDS mapping images obtained from the corresponding 2D PtSe₂ layers. (h) HRTEM image of the corresponding sample showing vertically aligned 2D PtSe₂ layers along with their schematic illustration (inset). (i) STEM image showing the edges of vertically aligned 2D PtSe₂ layers with an interlayer spacing of ~0.54 nm, corresponding to the schematic illustration in the inset

Figure 4. 3. (a) Variation of current in an optimized 2D PtSe₂/PI kirigami up to 2000% strain. The inset illustrates the corresponding kirigami design with $a = 17.2$ mm, $b = 0.4$ mm, and $c = 0.375$ mm. (b) Two-terminal I–V transport characteristics of the same kirigami compared at various strain levels. (c) Electrical failure obtained from another kirigami beyond ~2300% strain. (d) Cyclic test to show the variation in current with a large number of repeated stretchings measured at 3 V. (e) Camera images of the kirigami corresponding to (a) and (b) upon manual stretching up to 2000% strain. (f) Schematic of an LED continuity circuit using a 2D PtSe₂/PI kirigami as a stretchable conductor. (g) Demonstration of lighting up an LED by a 2D PtSe₂/PI kirigami stretched to 0 and 1500%.

Figure 4. 4. (a) Schematics showing the defining geometrical parameters for the unoptimized (left) vs optimized (right) kirigami patterns. (b, c) FEM simulations showing the strain distribution within the kirigami patterns of (b) unoptimized and (c) optimized parameters. (d) Graphical comparison of maximum in-plane principal strain vs stretch for the unoptimized (blue plot) vs optimized (red plot) kirigami patterns. The inset compares the simulated vs experimentally demonstrated images of kirigami patterns while their failure point is approximated to be ~ 0.1 times the maximum in-plane principal strain. (e–g) Plots of maximum in-plane principal strain vs stretch with varying geometrical parameters of (e) a, (f) b, and (g) c.

Figure 4. 5. (a) HRTEM image of horizontally aligned thin 2D PtSe₂ layers. (b) $I_{ds}-V_{ds}$ transfer characteristics from a back-gated FET based on horizontally aligned thin 2D PtSe₂ layers **con**Figure**d** on a SiO₂/Si wafer. (c) Schematic illustration of an electrolyte gating of a 2D PtSe₂/PI FET. (d) $I_{ds}-V_g$ and (e) $I_{ds}-V_{ds}$ transfer characteristics from a 2D PtSe₂/PI FET. The scale bar in the inset of (d) is 1 μ m. (f) $I_{ds}-V_g$ transfer characteristics from a 2D PtSe₂/PI kirigami FET. (g) Camera images of the kirigami FETs corresponding to (f).

Figure 4. 6. (a) Schematic of CVD growth of wafer-scale 2D PtTe₂ layers. (b) A photo of 2D PtTe₂ layers grown on a SiO₂/Si wafer on a size of 12 cm². (c) Thickness relation of initial Pt films vs. resulting 2D

PtTe₂ layers. (d) Raman spectra corresponding to the four spots marked on the sample in (b). (e) Cross-sectional TEM/EDS mapping images showing the spatial distribution of Pt and Te within 2D PtTe₂ layers. (f) EDS profile quantifying the atomic ratio of Pt and Te corresponding to (e).

Figure 4. 7. (a) Sheet resistances of 2D PtTe₂ layers prepared with Pt films of various thicknesses. (b) The temperature-dependent ratio of sheet resistance (R_s) normalized to the room-temperature sheet resistance ($R_{s,RT}$) obtained from PtTe₂-6nm sample.

Figure 4. 8. (a) Photos of 2D PtTe₂ layers-grown flexible PI substrates prepared with Pt films of various thicknesses. (b) The maximum temperature of 2D PtTe₂/PI samples prepared with various Pt thickness achieved at biases of 3, 5, and 7 V. (c) Time-dependent temperature fall/rise of the same samples in (b) obtained at 5 V. (d) Determination of the heating/cooling rate corresponding to (c). (e) Temperature variation obtained from a 2D PtTe₂-6nm/PI sample during the cyclic heating/cooling of 50 times at 4 V. (f) Representative IR images of the sample in (e) at three different cycle numbers. (g) Demonstration of the solar energy-driven operation of 2D PtTe₂/PI heaters. (h) Temperature variations achieved with 2D PtTe₂/PI heaters of various thickness driven by solar energy.

Figure 4. 9. (a) IR images of a PtTe₂-6nm/PI sample at various bending angles

obtained with the bending radius of 2 mm at 3 V. (b) Variation of the maximum temperature and relative resistance for the same sample in (a) as a function of bending angle and bending radius.

Figure 4. 10. (a) IR images of a 2D PtTe₂/PI Kirigami heater (insets) and the corresponding plots of T_{max} vs. strain rate. (b) Variations of T_{max} and R/R₀ obtained from the same sample in (a) during the cyclic stretch of 1,000 times with 70% of strain.

Figure 4. 11. (a) Demonstration of skin-attachable 2D PTe₂ layers-based Kirigami heaters in accordance with the mechanical motions of a human wrist. The IR images on the bottom panels show temperature distribution on the wrist when the heater was electrically biased. (b) IR images showing the temperature distribution of the wrists with (right) and without (left) attaching the heater.

Figure 4. 12. (a) Schematic illustration of fabrication steps for VA-2D MoS₂ layer-enabled stretchable sensors. (b) Demonstration of the VA-2D MoS₂ layer integration onto various polymeric substrates and serpentine-patterned sensors. The scale bars are 1 cm in all images.

Figure 4. 13. (a) Plane-view HRTEM image of VA-2D MoS₂ layers and the corresponding sample image (inset). The scale bar in the inset is 1 cm. (b) AFM height profile of VA-2D MoS₂ layers/PMMA interface and the corresponding topography image (inset). The

scale bar in the inset is 5 μm . (c) Optical transmittance spectra of PMMA and TOCN before/after integrating VA-2D MoS₂ layers. (d) Raman spectra from VA-2D MoS₂ layers in their pristine (black) and transferred (red) states. (e, f) XPS spectra for Mo and S binding energies of VA-2D MoS₂ layers: (e) Mo 3d core level before (black) and after (red) transfer and (f) S 2p core level before (black) and after (red) transfer.

Figure 4. 14. (a) Demonstration of lateral stretching in VA-2D MoS₂ layers. (b) I–V characterization corresponding to the sample in (a) with up to 40% strain. (c) Raman characterization corresponding to the sample in (a) before/after 40% stretching. (d) Electrical sensing of NO₂ gas with increasing concentration without stretching. (e) Concentration-dependent sensitivity. (f) NO₂ gas sensing with laterally stretched VA-2D MoS₂ layers at a 40% strain. (g) NO₂ sensing performance comparisons of this work vs other 2D MoS₂ layer-based sensors. (h) Demonstration of photocurrent generation in VA-2D MoS₂ layers at 0 and 40% strain.

Figure 4. 15. (a) Schematic of the serpentine pattern with dimensional parameters. (b) FEM images showing the spatial distribution of maximum principal strain and their consistency with the experimental observation. (c) Plots of stretch rate vs. resulting maximum principal strain corresponding to the two different locations in the inset image.

Figure 4. 16. DFT calculations for the adsorption states of NO₂ molecules with 2D MoS₂ layers in various configurations. (a) Snapshots of the relaxed configuration of the 2D MoS₂ layer basal plane viewed along the a- (top) and c-axis (bottom). (b) Snapshots of the relaxed configuration of VA-2D MoS₂ layers with NO₂ adsorbed to a S-exposed edge. (c) Snapshots of the relaxed configuration of VA-2D MoS₂ stretched along the b-axis (zigzag direction) by 10% of its original lattice constant with NO₂ adsorbed to a S-exposed edge. (d) Snapshots of the relaxed configuration of VA-2D MoS₂ layers with NO₂ adsorbed to a Mo-exposed edge. (e) Snapshots of the relaxed configuration of VA-2D MoS₂ stretched along the b-axis by 10% of its original lattice constant with NO₂ adsorbed to a Mo-exposed edge. In all Figures, the yellow-, purple-, gray-, and red-colored spheres indicate S, Mo, N, and O atoms, respectively.

Chapter 1. Introduction

This chapter is intended to introduce a framework in which proposed studies are conducted. It is intended to be used extensively while providing a broad view of the field of two-dimensional (2D) transition dichalcogenides materials (TMDs) materials. This chapter has consisted of discussions on the introduction of 2D TMDs layers, the structure of 2D TMDs layers, and the transfer and integration of 2D TMDs layers.

1.1. Introduce of 2D TMDs Materials

The development of low-dimensional nanomaterials (e.g., carbon nanotubes, one-dimensional (1D) nanowires, and two-dimensional (2D) layered materials) presents tremendous opportunities in the enrichment of life quality by bringing forth previously conceptually projected devices and technologies into reality. [1, 2, 3] Following the discovery of graphene, a monolayer of graphite, 2D layered materials have been gaining significant attention because of a large set of their unusual yet superior material properties enabled by coupling of extremely small physical dimension and van der Waals (vdW)-assisted anisotropic crystallinity.[4, 5, 6] These intrinsically unique features have prompted the expansion of 2D material libraries covering a broad spectrum of band structures from insulating to semiconducting and metallic,[6, 7, 8, 9, 10] e.g., hexagonal boron nitride (h-BN), black phosphorus (BP), silicene, TMDs, and transition metal carbides/nitrides (MXenes). Among these 2D material series, TMDs have received extensive attention because of their superior optical and electrical attributes, such as visible-wavelength band gap with intrinsic

tunability, high carrier mobility, and high on/off current ratio,[11, 12, 13, 14, 15, 16] many of which are unattainable in graphene.[6, 17] With the provision of these advantages, 2D TMDs have found extensive applications in a wide range of novel electronics and optoelectronics devices, e.g., near atom thickness circuitry, extremely low-power transistors, and tunable band gap energy accompanying its indirect-to-direct transition, which were foreseen to be challenging to realize otherwise.[6, 9, 10, 18, 19, 20] In addition to their electrical and optical merits, 2D TMDs also possess exceptional mechanical properties with high elasticity and flexibility, owing to their extremely small vertical thickness and large in-plane strain limits, allowing them to be applicable to mechanically reconfigurable devices such as flexible transistors, wearable sensors, and foldable displays[7, 8, 17] as shown in Figure 1. 1. The great success of graphene has been followed by an equally impressive surge for the development of other 2D materials that can form atomic sheets with extraordinary properties.

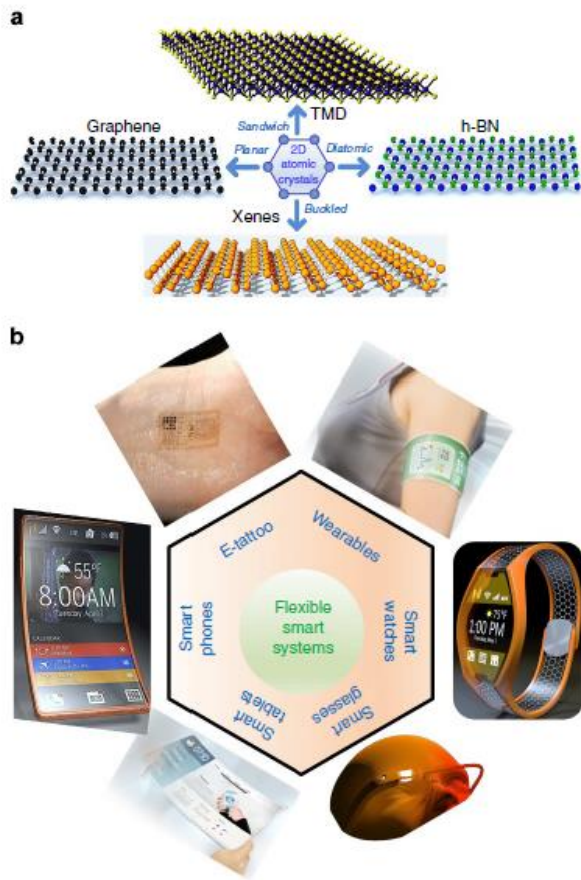


Figure 1. 1. Illustration of 2D layer materials and examples of flexible smart systems, adapted with permission from reference [21].

1.2. Structure of 2D TMDs Layers

1.2.1. Atomic Structure of 2D TMDs Layers

2D TMDs are layered materials in which each unit, MX_2 , consisted of a transition metal (M) layer sandwiched between two chalcogens (X) atomic layers. The structures of 2D TMDs can be categorized depending on the arrangement of the atoms as trigonal prismatic (hexagonal, H), octahedral (tetragonal, T) and their distorted phase (T') as shown in Figure 1. 2a. In H-phase 2D TMDs structure, each metal atom located in six branches out to two tetrahedrons in +z and -z directions while the hexagonal symmetry can be seen in the top view (Figure 1. 2a). Accordingly, chalcogen-metal-chalcogen arrangement along z-direction is considered as a single layer, and weak vdW interactions between each layer can make a mechanical exfoliation from bulk TMDs material to achieve a single layer flake. T-phase has a trigonal chalcogen layer at the top side of the metal atom and 180 degrees rotated at the bottom side of the metal atom in a single layer, which called trigonal antiprism, and results in the hexagonal arrangement of chalcogen atoms in the top view. Metal atoms are distorted further (or dimerized in one direction) showing the reduction of atomic displacement of chalcogen atoms along z-direction (δ), called T' -phase [22, 23].

As listed in Fig. 1.2b, 2D TMDs reveal a wide range of bandgap covering all visible and infrared range with the choice of material.[24] Most semiconducting 2D TMDs reveal direct bandgap in monolayer, whereas they are indirect bandgap in bulk form except few cases of GaSe and ReS_2 . [25, 26]. For example, monolayer dichalcogenides such as MoS_2 (1.8 eV), MoSe_2 (1.5 eV), (2H)-

MoTe₂ (1.1 eV), WS₂ (2.1 eV) and WSe₂ (1.7 eV) show direct bandgap, whereas bulk phases exhibit indirect gap with smaller energies. The stable phase of MX₂ material at room temperature is 2H phase, whereas 1T phase can be obtained by Li-intercalation[27] or electron beam irradiation.[28] The chemically exfoliated 1T MoS₂ phase is known to be 107 times more conductive than the semiconducting 2H phase.[29] In case of WTe₂, 1T or 1T' phase is more stable than 2H phase at room temperature.[30] Both 2H and 1T' phase in MoTe₂ can be easily modulated into each other because the cohesive energy difference between both phases is similar to each other. The electronic and structural characteristics of different layered TMDs are summarized in Table 1. 1.

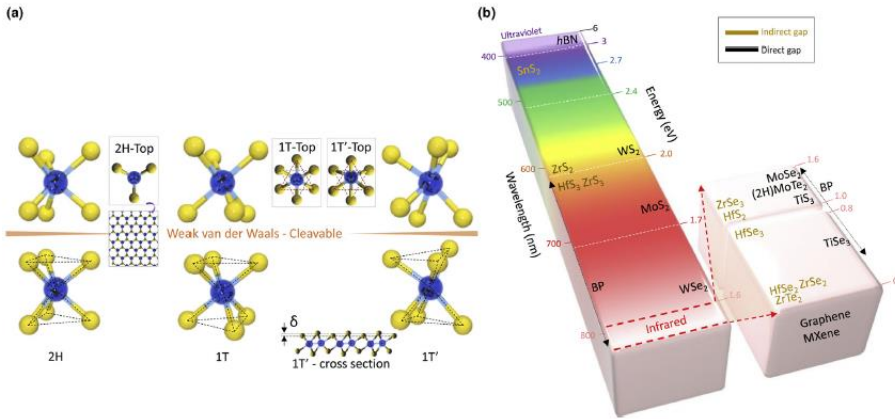


Figure 1. 2. (a) Typical structures of layered transition metal dichalcogenides. Cleavable 2H, 1T and 1T' structures in layered TMD are shown. (b) Bandgap of 2D layered materials varying from zero band gap of graphene (white color) to wide bandgap of hBN. The color in the column is presenting the corresponding wavelength of bandgap, adapted with permission from reference. [19]

Group	M	X	Electric Properties	Structural Property
4	Ti, Hf, Zr	S, Te	Semiconducting ($E_g = 0.2 \sim 2$ eV)	1T: TiS ₂ , TiSe ₂ , TiTe ₂
5	V, Nb, Ta	S, Se, Te	Narrow band metals or semimetals	2H: TaS ₂ , TaSe ₂ , NbS ₂ , NbSe ₂ 1T: VTe ₂ , TaTe ₂ , NbTe ₂
6	Mo, W	S, Se, Te	Sulfides and Selenides are semiconducting. Telurides are semi-metallic	2H: MoS ₂ , MoSe ₂ , MoTe ₂ , WS ₂ , WSe ₂ 1T: WTe ₂
7	Tc, Re	S, Se, Te	Small gap semiconductors	
10	Pd, Pt	S, Se, Te	Sulfides and Selenides are semiconducting. Telurides are metallic. PdTe ₂ is superconducting	

Table 1. 1. Electronic and structural properties of different layered TMDs, adapted with permission from reference [53].

1.2.2. Growth Orientation of 2D TMDs Layers

In addition to the structure depend on the arrangement of the atoms, the 2D TMDs layer can be categorized by growth orientation as horizontally aligned structure and vertically aligned structure. The 2D TMDs layers garnered significant interest owing to their unique structural tunability enabling two distinct layer orientations.[31, 32] The electric characteristics of the 2D TMDs layer depend on the alignment structure of layers, and the tunable band gap structure is revealed through density functional theory (DFT) calculations and experimental approaches.[32, 33] Accordingly, the versatility of 2D TMDs for technological applications strongly depends on the crystallographic orientation of the constituent 2D layers and their atomic configuration. For instance, horizontally oriented 2D TMDs layers exposing 2D basal planes on their surface present combined advantages of a large in-plane strain limit and near ballistic semiconducting transport, showing promise for high-performance flexible electronics.[34, 35] On the other hand, 2D TMDs with vertically-aligned layers exhibit numerous atomic dangling bonds on their 2D layer edge sites which are predominantly exposed on the surface.[31, 36] As a result, they are projected to exhibit superior chemical and/or physical adsorption-driven surface reactivity offering uniquely suited advantages for a wide range of applications such as chemical and electrochemical sensing.[37-39] In fact, it has been experimentally verified that they present significantly improved sensitivity for detecting various chemical species compared to the 2D TMDs basal planes of atomically saturated bonding.[40, 41]

1.3. Transfer and Integration of 2D TMDs Layer

2D TMDs layers have recently gained enormous interests owing to their near ideal combination of superior electrical and mechanical properties unattainable in any conventional materials.[42–44] For instance, they can tolerate significant mechanical deformation owing to unusually high in-plane strain limits - i.e. >5 times over covalently-bonded inorganic thin films, while preserving intrinsic semiconductor properties manifested by large ON/OFF current ratios demanded for modern transistors.[45, 46] Such property advantages project unexplored opportunities in a wide range of emerging technologies, particularly in digital electronics of unconventional form factors such as wearable and stretchable devices. As 2D TMD layers present weak vdW attraction to underlying growth substrates, the individual integration of them in a layer-by-layer manner achieving targeted electronic structures can be possible implicating new direction for 2D heterojunction structures with befitting band offsets.[47–49] For the exploration of 2D TMDs layer to novel technologies, there is a few critical prerequisites for the realization of the aforementioned advantages. First, it is required to develop viable strategies to transfer 2D TMDs layers from as-growth substrates and integrate them on target substrates for diverse functionalities like transparent, mechanically flexible, and stretchable substrates. Second, the intrinsic properties of the transferred 2D layers including structural, mechanical, and electrical properties need to be maintained properties of the origin 2D layers throughout their transfer and integration process and be uniformly preserved on a wafer scale. Lastly, for the technical diversity, the layer integration process should be generalized to 2D

TMDs layers, substrates of diverse materials, not limited to any particular types. In order to satisfy the requirements for the transfer and integration, the chemical etching methods of underlying growth substrates involving protection polymers (e.g., polymethyl-methacrylate (PMMA)) and subsequent chemical lift-off are being studied most actively.[50–52] However, such strategies use solution-based chemicals to etch both the protective layer and the growth substrate (e.g., silicon dioxide (SiO_2) or sapphire wafer), presenting the fragmentation of the individual 2D layers.[51] Therefore, they not only impose scalability limitations in that the 2D layers of multiple components are non-uniformly stacked in a controlled manner, but they are also difficult to apply to various unconventional substrates. In addition, the inherent material properties of 2D layers are often compromised and damaged by the chemicals used throughout their transfer and integration steps. For the successful transfer and integration of large area 2D TMD layers, new approaches are needed that demand the aforementioned requirements. To this end, techniques for delamination of 2D TMD layer materials from the growth substrate without an additional etchant or protection layer, and peeling techniques using water-soluble materials are being studied.

1.4. Engineering the Structure of 2D TMDs to be Mechanically Reconfigurable Form

Electrical performances of 2D TMD layers as active device components in mechanically reconfigurable electronics can be modulated by the mechanical deformation of their underlying integration substrates. This large degree of

mechanical tunability for both active (i.e. 2D TMDs) and passive (i.e. substrates) components in reconfigurable devices greatly broaden their versatility toward unprecedented areas of device applications. A variety of approaches to prepare for both 2D TMDs and underlying substrates in physical forms compatible with mechanically reconfigurable devices are discussed in the following subsection.

1.4.1. 3D texturing based on pre-structured polymeric templates.

Substantial efforts have been recently made toward converting intrinsically 2D TMDs layers to three-dimensional (3D) geometries in a way to increase their mechanical tolerance in both in- and out-of-plane directions. As a result, 2D TMDs can sustain physical forms more suitable for mechanically reconfigurable devices, which can more readily respond to externally exerted mechanical stimuli. One of the most commonly adopted approaches to obtain ‘out-of-plane’ flexibility in addition to their intrinsic in-plane deformability is to prepare 2D TMD layers onto pre-stretched elastomeric substrates followed by releasing the pre-applied strain.[54, 55] Consequently, 2D TMD layers can replicate three-dimensionally corrugated or crumpled structures, ensuring higher mechanical stretching and multiscale deformability. Okogbue et al utilized pre-stretched elastomeric substrates and directly integrated centimeter-scale 2D MoS₂ layers onto them by using the above discussed water-assisted transfer method. As a result, the original pattern geometry of the substrates became translated to the integrated 2D MoS₂ layers, realizing strain-tunable multi-functionalities in them.

1.4.2. Strain engineering of large-area 2D TMDs by origami and kirigami patterning.

The strain engineering concept adopting origami and kirigami patterns inspired by ancient Japanese paper cutting art has been utilized to create out-of-plane 3D structures out of in-plane 2D TMD layers. This idea is particularly suitable for developing device components in foldable electronics for futuristic wearable technologies [56]. The concept of origami and/or kirigami patterns enabled strain engineering is that the external strain developed with folding and twisting materials can be easily accommodated through an array of repeating patterns composed of thin rows on them. This concept was initially explored by creating graphene based large area origami structures, leading to the development of self-folding graphene oxide composites with dual-gradient structures. These origami materials developed by Mu et al exhibit mechanical deformability upon light and heat exposure; e.g. self-folding and swelling upon water absorption and shrinking under nearinfrared irradiation.[57] Kirigami patterning which is a variation of origami involves periodically-arranged straight cuts that are used to impart stretchability by converting applied stress to torsion at specific points between the cuts. The beam bending theory is used to model the relationship between the principal parameters in a kirigami cut and the critical tensile force, predicting maximum stretchability [58]. Despite of an effort to gain stretchability, the experimental realization of “stand-alone” 2D TMD-based kirigami patterning has been unavailable. This limitation is attributed to the technical difficulty associated with reliably handling extremely thin 2D layers in a free-standing form. As a result, limited success has been

demonstrated with the graphene kirigami of a very small dimension ($\leq 100 \mu\text{m}^2$) realized by highly sophisticated lithographic fabrication processes.[59] Directly integrating 2D TMDs into kirigami-patterned secondary substrates of high mechanical flexibility and electrical insulation (e.g., plastics) can be a viable alternative. Although it is desirable to grow 2D TMDs directly on flexible substrates for subsequent kirigami patterning, the intrinsically high growth temperatures inherent to most 2D TMDs have made this approach technically challenging.

1.5. Reference

- (1) J.J. Gooding., et al. Nanostructuring electrodes with carbon nanotubes: A review on electrochemistry and applications for sensing. *Electrochim. Acta* 50, 3049 (2005)
- (2) Y. Li., et al. Nanowire electronic and optoelectronic devices. *Mater. Today* 9, 18 (2006)
- (3) M. Trojanowicz., et al. Analytical applications of carbon nanotubes: A review. *TrAC, Trends Anal. Chem.* 25, 480 (2006)
- (4) M.J. Allen., et al. Honeycomb carbon: A review of graphene. *Chem. Rev.* 110, 132 (2009)
- (5) Y. Zhang., et al. Review of chemical vapor deposition of graphene and related applications. *Acc. Chem. Res.* 46, 2329 (2013)
- (6) G.R. Bhimanapati., et al. Recent advances in two-dimensional materials beyond graphene. *ACS Nano* 9, 11509 (2015)
- (7) C. Tan., et al. Recent advances in ultrathin two-dimensional nanomaterials. *Chem. Rev.* 117, 6225 (2017)
- (8) H. Zhang., et al. Ultrathin two-dimensional nanomaterials. *ACS Nano* 9, 9451 (2015)
- (9) S. Das., et al. Beyond graphene: Progress in novel two dimensional materials and van der Waals solids. *Rev. Mater. Res.* 45, 1 (2015)
- (10) F. Wang., et al. Synthesis, properties and applications of 2D non-graphene materials. *Nanotechnology* 26, 292001 (2015)
- (11) K.F. Mak., et al. Atomically thin MoS₂: A new direct-gap semiconductor. *Phys. Rev. Lett.* 105, 136805 (2010)
- (12) H.J. Conley., et al. Bandgap engineering of strained monolayer and bilayer

MoS₂. *Nano Lett.* 13, 3626 (2013)

(13) S. Susarla., et al. Quaternary 2D transition metal dichalcogenides (TMDs) with tunable bandgap. *Adv. Mater.* 29, 1702457 (2017)

(14) X. Duan., et al. Synthesis of WS₂xSe_{2-2x} alloy nanosheets with composition-tunable electronic properties. *Nano Lett.* 16, 264 (2016)

(15) X. Bao., et al. Band structure engineering in 2D materials for optoelectronic applications. *Adv. Mater. Technol.* 3, 1800072 (2018)

(16) H. Sahin., et al. Anomalous Raman spectra and thickness dependent electronic properties of WSe₂. *Phys. Rev. B* 87, 165409 (2013)

(17) L. Gao., et al. Flexible device applications of 2D semiconductors. *Small* 13, 1603994 (2017)

(18) C. Gong., et al. Electronic and optoelectronic applications based on 2D novel anisotropic transition metal dichalcogenides. *Adv. Sci.* 4, 1700231 (2017)

(19) W. Choi., et al. Recent development of two-dimensional transition metal dichalcogenides and their applications. *Mater. Today* 20, 116 (2017)

(20) M.S. Shawkat., et al. Two-dimensional/three-dimensional Schottky junction photovoltaic devices realized by the direct CVD growth of vdW 2D PtSe₂ layers on silicon. *ACS Appl. Mater. Interfaces* 11, 27251 (2019)

(21) Deji Akinwande., et al. Two-dimensional flexible nanoelectronics. *Nature Communications* 5, 5678 (2014)

(22) D.H. Keum, et al. Bandgap opening in few-layered monoclinic MoTe₂. *Nat. Phys.* 11 (2015) 482.

(23) M.N. Ali, et al. Large, non-saturating magnetoresistance in WTe₂. *Nature* 514 (2014) 205.

(24) F. Xia, et al. Two-dimensional material nanophotonics. *Nat. Photonics* 8

(2014) 899.

(25) O. Del Pozo-Zamudio, et al. Photoluminescence of two-dimensional GaTe and GaSe films. *2D Mater.* 2 (2015) 035010.

(26) S. Tongay, et al. Monolayer behavior in bulk ReS₂ due to electronic and vibrational decoupling. *Nat. Commun.* 5 (2014) 3252.

(27) R. Kappera, et al. Phase-engineered low-resistance contacts for ultrathin MoS₂ transistors. *Nat. Mater.* 13 (2014) 1128.

(28) Y.-C. Lin, et al. Atomic mechanism of the semiconducting-to-metallic phase transition in single-layered MoS₂. *Nat. Nanotechnol.* 9 (2014) 391.

(29) R. Kappera, et al. Metallic 1T phase source/drain electrodes for field effect transistors from chemical vapor deposited MoS₂ *APL Mater.* 2 (2014) 092516.

(30) K.-A.N. Duerloo, et al. Structural phase transitions in two-dimensional Mo- and W-dichalcogenide monolayers. *Nat. Commun.* 5 (2014) 4214.

(31) Y. Jung, J., et al. Metal seed layer thickness-induced transition from vertical-to-horizon growth of MoS₂ and WS₂. *Nano Letters* 14, 6842–6849 (2014)

(32) S. S. Han., et al. Horizontal-to-Vertical Transition of 2D Layer Orientation in Low-Temperature CVD-Grown PtSe₂ and Its Influences on Electrical Properties and Device Applications. *ACS Appl. Mater. Interfaces*, 11 (14), pp 13598–13607 (2019)

(33) M. Wang., et al. Wafer-Scale Growth of 2D PtTe₂ with Layer Orientation Tunable High Electrical Conductivity and Superior Hydrophobicity. *ACS Applied Materials & Interfaces* 12 (9), 10839-10851 (2020)

(34) D. Akinwande., et al. Two-dimensional flexible nanoelectronics. *Nat. Commun.* 5, 5678 (2014)

- (35) K. J. Yu., et al. Inorganic semiconducting materials for flexible and stretchable electronics. *npj Flexible Electron.* 1, 4 (2017)
- (36) D. Kong., et al. Synthesis of MoS₂ and MoSe₂ Films with Vertically Aligned Layers. *Nano Lett.* 13, 1341–1347 (2013)
- (37) B. Ni and X. Wang, Graphene-like WSe₂ nanosheets for efficient and stable hydrogen evolution. *Adv. Sci.* 2, 1500085 (2015)
- (38) Y. Tan., et al. The combinations of hollow MoS₂ micro@ nano-spheres: one-step synthesis, excellent photocatalytic and humidity sensing properties. *J. Mater. Chem. C* 2, 5422–5430 (2014)
- (39) J. Kibsgaard., et al. Engineering the surface structure of MoS₂ to preferentially expose active edge sites for electrocatalysis. *Nat. Mater.* 11, 963–969 (2012)
- (40) S.-Y. Cho., et al. Highly Enhanced Gas Adsorption Properties in Vertically Aligned MoS₂ Layers. *ACS Nano* 9, 9314–9321 (2015)
- (41) G. Deokar., et al. Large area growth of vertically aligned luminescent MoS₂ nanosheets. *Nanoscale* 9, 277–287 (2017)
- (42) Mak, K. F., et al. Atomically thin MoS₂: a new direct-gap semiconductor. *Phys. Rev. Lett.* 105, 136805 (2010).
- (43) Bhimanapati, G. R. et al. Recent Advances in two-dimensional materials beyond graphene. *ACS Nano* 9, 11509–11539 (2015).
- (44) Liu, Y. et al. Van der Waals heterostructures and devices. *Nature Reviews Materials* 1, 16042 (2016).
- (45) Akinwande, D., Petrone, N. & Hone, J. Two-dimensional flexible nanoelectronics. *Nat. Commun.* 5, 5678 (2014).
- (46) Gao, L. Flexible device applications of 2D semiconductors. *Small* 13,

1603994–n/a (2017).

(47). Pant, A. et al. Fundamentals of lateral and vertical heterojunctions of atomically thin materials. *Nanoscale* 8, 3870 (2016).

(48) Li, M.-Y., et al. Heterostructures based on two-dimensional layered materials and their potential applications. *Mater. Today* 19, 322–335 (2016).

(49) Das, S., et al. Beyond graphene: progress in novel two-dimensional materials and van der Waals solids. *Annu. Rev. Mater. Res.* 45, 1–27 (2015).

(50) Gurarlsan, A. et al. Surface energy-assisted perfect transfer of centimeter-scale monolayer and few-layer MoS₂ films onto arbitrary substrates. *ACS Nano* 8, 11522–11528 (2014).

(51) Lin, Y.-C. et al. Wafer-scale MoS₂ thin layers prepared by MoO₃ sulfurization. *Nanoscale* 4, 6637–6641 (2012).

(52) Liu, K.-K. et al. Growth of large-area and highly crystalline MoS₂ thin layers on insulating substrates. *Nano Lett.* 12, 1538–1544 (2012).

(53) M Chhowalla, et al. The chemistry of two-dimensional layered transition metal dichalcogenide nanosheets. *Nat. Chem.* 5, 263 (2013)

(54) Okogbue E., et al. Centimeter-scale periodically corrugated few-layer 2D MoS₂ with tensile stretch-driven tunable multifunctionalities. *ACS Appl. Mater. Interfaces* 10 30623–30 (2018)

(55) Kim M., et al. A stretchable crumpled graphene photodetector with plasmonically enhanced photoresponsivity. *Nanoscale* 9 4058–65 (2017)

(56) Hawkes E., et al. Programmable matter by folding *Proc. Natl. Acad. Sci. USA* 107 12441–5 (2010)

- (57) Mu J., et al. Origami-inspired active graphene-based paper for programmable instant self-folding walking devices *Sci. Adv.* 1 e1500533 (2015)
- (58) Tang Y., et al. Programmable kiri-kirigami metamaterials *Adv. Mater.* 29 1604262 (2017)
- (59) Blees, M. K., et al. Graphene kirigami. *Nature.* 524, 204–213 (2015)

Chapter 2. Growth Behavior and its Properties of

2D TMDs Layers

2.1. Growth Behavior and Properties of 2D PtSe₂ Layers

The contents of this section have been published in: Sang Sub Han, Jong Hun Kim, Chanwoo Noh, Jung Han Kim, Eunji Ji, Junyoung Kwon, Seung Min Yu, Tae-Jun Ko, Emmanuel Okogbue, Kyu Hwan Oh, Hee-Suk Chung, YounJoon Jung, Gwan-Hyung Lee & Yeonwoong Jung. “Horizontal-to-Vertical Transition of 2D Layer Orientation in Low-Temperature Chemical Vapor Deposition-Grown PtSe₂ and Its Influences on Electrical Properties and Device Applications” ACS Appl. Mater. Interfaces 11, 13598–13607 (2019).

2.1.1. Introduction

Recent efforts toward developing 2D TMDs of improved electrical and optoelectrical properties have triggered studies on other types of MX₂ where M is noble metals such as platinum (Pt) or palladium (Pd) instead of refractory materials. Among them, 2D platinum diselenide (2D PtSe₂) is a relatively less explored one in a layered crystallinity of MX₂ with close-packed arrays of Pt atoms in between Se atomic rows.[10–12] This material has recently drawn substantive research interests owing to several projected advantages which are absent in Mo- or W-based 2D TMDs particularly for electronics and optoelectronics;[1, 5–10] (1) it exhibits metallic carrier transport in bulk phase while its band gap opens up with transiting to 2D monolayer forms.[11–13] (2) Its theoretically predicted carrier mobility in a semiconducting phase reaches up to >1000 cm² V⁻¹ s⁻¹ at room temperature, [9, 14, 15] significantly higher than that of 2D MoS₂ [14, 16] and even comparable to that of black phosphorus (BP).[1, 10, 12, 17] (3) Unlike BP which is prone to significant oxidation, 2D

PtSe₂ is stable in air as it is based on a noble metal, Pt, which is highly oxidation-resistant.[9, 18] In addition to these intrinsically attractive material properties, 2D PtSe₂ is anticipated to offer distinguishable advantages in terms of their process capability over Mo (or W)-based 2D TMDs. The melting temperature of elemental Pt is less than ~2/3 of that of Mo (or W), and the reaction activation energy for the formation of PtSe₂ is significantly smaller than that for MoS₂ (or WS₂).[19–21] Accordingly, chemical vapor transition (CVT) growth of 2D PtSe₂ layers can happen at much lower temperature[10, 22–26] than what is demanded for growing 2D MoS₂ (or WS₂) layers. Despite these projected advantages, much of fundamental issues pertaining to the material properties and crystalline structures of 2D PtSe₂ layers still remain unclarified. Particularly, their morphological evolution during CVT growth and its influence on carrier transport properties have remained largely unexplored, although its clarification would be highly useful for broadening their technological versatility. Clearly understanding the correlation of structural morphology versus electrical characteristics in 2D PtSe₂ layers is highly timely as their applications are expanding to a variety of electronics including field-effect transistor (FET),[8–10, 15] broadband photo-detection,[1, 5–7, 27] photo-energy conversion,[26, 28] and piezoelectric sensing.[29]

In this study, we study the growth characteristics of large-area (> a few cm²) 2D PtSe₂ layers and investigate their direct correlation with carrier transport properties. We systematically grew 2D PtSe₂ layers by employing the CVD selenization of Pt seeds of controlled thickness and studied their near-atomic structural morphology. We observed that the crystallographic orientation of 2D

PtSe₂ layers transits from “horizontal-to-vertical” with increasing layer thickness, which happens even at the low growth temperature of 400 °C. Interestingly, this structural transition is accompanied by the drastic change of electrical transport properties as clarified by FET characterization. While vertically aligned 2D PtSe₂ layers exhibit metallic characteristics, strong FET gate responses were observed with horizontally aligned 2D PtSe₂ layers prepared with Pt of very small thickness (~0.75 nm). Intrinsically *p*-type FET mobility of ~625 cm²/V s was measured at room temperature, which is significantly higher than the mobility values observed with any previous studies on CVD-grown 2D PtSe₂ layers.[3, 9, 10, 27] DFT calculation was employed to further verify this experimentally observed coupled transition of 2D layer orientation and carrier transport characteristics. The calculation indicates that the band gap of 2D PtSe₂ layers.

2.1.2. Experimental Section

2.1.2.1. 2D PtSe₂ Layer Growth

2D PtSe₂ layers were CVD grown using a horizontal quartz tube furnace (Lindberg/Blue M Mini-Mite). Pt seeds of controlled thickness were deposited on growth substrates including SiO₂/Si wafers (300 nm; SiO₂ thickness) and PI films by an electron beam evaporator (Thermionics VE-100) at a fixed evaporation rate of 0.15 Å/s. Pt-deposited substrates were placed in the center zone of the CVD furnace, and an alumina boat containing Se powder was placed at the furnace upstream side (temperature ~200°C). The quartz tube was pumped down to a base pressure of ~1 mTorr and purged with argon (Ar) gas

to remove oxygen and organic residuals. Subsequently, it was heated to the growth temperature of 400 °C with total ramping time of 50 min and was maintained for another 50 min. During the growth reaction, the flow rate of Ar gas was maintained to be ~100 standard cubic centimeters per minute (SCCM) at a pressure of ~80 mTorr.

2.1.2.2. TEM/STEM Characterization

Structural and chemical analyses of as-grown 2D PtSe₂ layers were performed using FEI F30 TEM and JEOL ARM 200F Cs-corrected TEM. FEI F30 TEM operation was carried out at an accelerating voltage of 300 kV and JEOL ARM 200F TEM was operated at 200 kV. For plane-view TEM sample preparation, buffered oxide etchant and water were directly applied to 2D PtSe₂ layers grown on SiO₂/Si substrates and PI films, respectively. Exfoliated 2D PtSe₂ layers were directly integrated onto copper TEM grids by mechanically scooping them. Cross-sectional TEM samples were prepared by focused ion beam TEM lift-out techniques.

2.1.2.3. Raman Characterization

Raman characterization was performed using inVia confocal-Raman microscope system (Renishaw) in ambient conditions at room temperature. A laser source of 532 nm wavelength was used and the excitation power was set to be 1 mW to minimize any sample damage. Raman emission was collected and dispersed by a grating of 1800 lines-per-mm with the data accumulation duration of 10 s.

2.1.2.4. Device Fabrication and Electrical Measurement

For 2D PtSe₂ FET device fabrication, Cr (1 nm)/Au (70 nm) electrodes were

patterned on top of as-grown 2D PtSe₂ layers on SiO₂/Si substrates through a shadow mask by electron beam evaporation in a vacuum of 10⁻⁷ Torr. All electrical measurements were carried out at a home-built probe station using Keithley 4200 semiconductor parameter analyzer in ambient conditions at room temperature.

2.1.2.5. DFT Calculation

Wave functions were approximated with projector-augmented wave pseudo-potentials,[47] and the exchange–correlation functional was described by generalized gradient approximation of Perdew–Burke–Ernzerhof parameters.[48, 49] A cutoff energy of 500 eV was used and the geometry optimization was performed until the energy convergence satisfies the criterion of 1.0×10^{-5} eV/Å. In the case of bulk PtSe₂, unit cells and atomic positions were relaxed during the geometry optimization, while all the other 2D PtSe₂ structures were relaxed from the optimized geometry with fixed unit cells. The unit cells of pristine and vertical 2D PtSe₂ layers were set to be in hexagonal and orthorhombic lattices, respectively. During the calculation, the first Brillouin zone was sampled with the Monkhorst–Pack grid of $11 \times 11 \times 11$ k points for monolayer 2D PtSe₂ layers and bulk crystals and $7 \times 7 \times 3$ k points for vertically aligned 2D PtSe₂ layers. The lattice constant of PtSe₂ is set to be 3.78 Å, the thickness of each 2D layer is 2.58 Å, and the interplanar spacing between each layer is 5.12 Å. The monolayer of horizontally aligned 2D PtSe₂ is defined by setting ~15 Å vacuum between each layer.

2.1.2.6. XPS Characterization

XPS characterization was performed with a Thermo VG Scientific K-α

system equipped with an Al K α -ray source (1486.3 eV) in ultrahigh vacuum conditions. The energy resolution of the instrument is \sim 0.5 eV and 100 W X-ray spot of 400 μm^2 was used for surface scans with pass energy of 50 eV. All XPS peaks are calibrated using the binding energy of C 1s, 284.5 eV, and Shirley-typed background is subtracted for peak fitting.

2.1.3. Results and Discussion

2.1.3.1. Orientation Controlled Growth of PtSe₂ Layers

We grew 2D PtSe₂ layers by selenizing Pt-deposited SiO₂/Si substrates with Pt seeds of various thicknesses. Figure 2. 1a shows as-grown 2D PtSe₂ layers-on-SiO₂/Si substrates prepared under identical CVT conditions with Pt thickness of 0.75–10 nm. Each sample is 1 cm² in size and distinguishable optical color represents different 2D layer thickness. Transmission electron microscopy (TEM) characterization was employed to inspect the microstructure of 2D PtSe₂ layers and to verify the effect of Pt seed thickness on resulting 2D layer morphology. Figure 2. 1b–e compares the morphology of 2D PtSe₂ layers grown with Pt of 0.75, 3, 6, and 10 nm, respectively. All TEM images were taken at identical magnification, and their corresponding selective area electron diffraction (SAED) patterns are presented as bottom insets. Figure 2. 1b shows a TEM image of 2D PtSe₂ layers grown with Pt of 0.75 nm and the representative high-resolution scanning TEM (HR-STEM) image in the top inset obtained from the same sample better clarifies their poly-crystalline structure. It is evident that the material consists of multiple crystalline grains composed of horizontally stitching individual 2D layers of distinct crystallographic orientation. In 2D PtSe₂ layers prepared with increasing Pt

thickness, we start to observe an appearance of crystalline grains composed of vertically aligned 2D layers (Figure 2. 1c–e); for example, the red arrows in Figure 2. 1c denote the grains of vertically aligned 2D layers prepared with Pt of 3 nm. The density of the vertical 2D layer grains gradually increases with further increasing Pt thickness (Figure 2. 1c, d), and the sample prepared with 10 nm Pt (Figure 2. 1e) is observed to mostly consist of vertically aligned 2D layers. The top inset in Figure 2. 1e represents the HR-STEM image of vertically aligned 2D PtSe₂ layers which predominantly expose their 2D edge sites on the surface. This morphological transition of 2D layer orientation is also noticeable in SAED patterns. The SAED obtained from horizontally aligned 2D layers (Figure 2. 1b bottom inset) predominantly exhibit the ring patterns corresponding to (100) and (110) orientations within the 2D PtSe₂ hexagonal basal planes exposed on the surface.[15, 30] As 2D layers transit to vertical orientation, SAED starts to display the ring patterns corresponding to (001) crystalline planes, that is, c-axis of hexagonal PtSe₂ (Figure 2. 1c, d) exhibiting sharp contrast to the characteristics observed with horizontally aligned layers (Figure 2. 1b). As the degree of vertical alignment increases, the intensity of (001) SAED pattern becomes stronger (e.g., Figure 2. 1c vs e), indicating the increasing dominance of vertically aligned 2D layers aligned along the c-axis of their hexagonal crystals. This systematic TEM characterization strongly confirms that 2D PtSe₂ layers undergo the transition of horizontal-to-vertical orientation with increasing layer thickness. In order to clarify whether this structural transition is associated with or driven by any chemical compositional alteration, we carried out energy-dispersive X-ray

spectroscopy (EDS) characterization. Figure 2. 1f shows EDS profiles obtained from 2D PtSe₂ layers prepared with Pt of 0.75 nm (top) and 10 nm (bottom) thickness, respectively. The results confirm the stoichiometric atomic ratio of Pt/Se = 1:2 in both materials irrespective of the distinctions in their 2D layer orientation (horizontal vs vertical) and initial Pt thickness (0.75 nm vs 10 nm). The areal coverage ratio of vertically aligned 2D PtSe₂ layers was quantified by analyzing five representative top-view TEM images of each sample taken at identical magnification. Figure 2. 1g shows an apparent trend that 2D PtSe₂ layers preferably grow in vertical orientation with increasing Pt thickness. It is noteworthy that the thickness of Pt seeds significantly increases (~4–5 times) as they get converted to 2D PtSe₂ layers by the CVT selenization. Also, the surfaces of vertically aligned 2D PtSe₂ layers are more rough and irregular compared to horizontally aligned 2D PtSe₂ layers exposing their basal planes on the surface (Figure 2. 2).

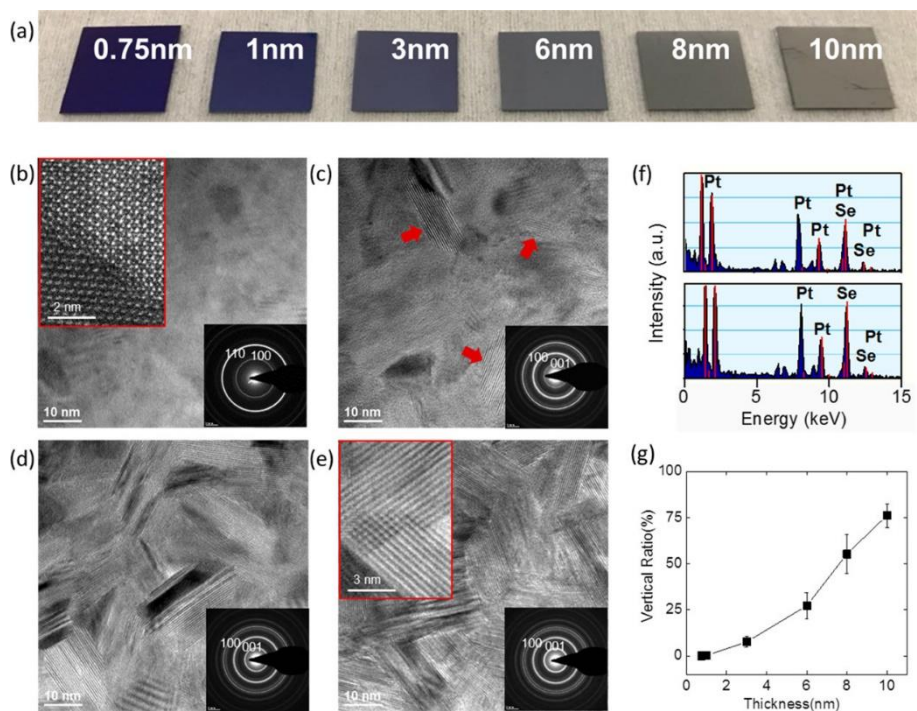


Figure 2.1. (a) Photograph of as-grown 2D PtSe₂ layers-on-SiO₂/Si substrates prepared with Pt of the noted thicknesses. (b–e) TEM characterization of 2D PtSe₂ layers grown with Pt of (b) 0.75 (c) 3 (d) 6, and (e) 10 nm. (f) EDS profiles obtained from 2D PtSe₂ layers prepared with 0.75 nm (top) and 10 nm (bottom) Pt seeds. (g) Coverage ratio of vertically aligned 2D PtSe₂ layers as a function of Pt thickness.

2.1.3.2. Atomic-scale Structural Analysis of Orientation Transition

Atomic-scale structural details of horizontal and vertical 2D PtSe₂ layers were further inspected by HR-STEM. Figure 2. 2a–c presents the plane-view and cross-sectional characterization of horizontally aligned 2D PtSe₂ layers. The low-magnification TEM image in Figure 2. 2a shows the uniform imaging contrast of horizontally aligned 2D PtSe₂ layers reflecting their high spatial homogeneity. The corresponding HR-STEM image We grew 2D PtSe₂ (Figure 2. 2b) reveals that the entire sample area is composed of horizontally aligned 2D layers without the presence of any crystalline grains of vertically aligned layers. The magnified image (red box) clearly shows a mixture of crystal lattice fringes obtained from (001) zone axis-oriented hexagonal 2D PtSe₂ as well as typical Moiré fringes, indicative of vertically stacked 2D horizontal layers of crystallographic misalignment. Figure 2. 2c reveals the cross-sectional view of the corresponding horizontally aligned 2D PtSe₂ of ~10 layers. It is evident that the horizontally aligned 2D PtSe₂ layers exhibit well-resolved interlayer spacing of ~5.2 Å which corresponds to the (001) planar distance of hexagonal PtSe₂ crystals.^{15,40} Figure 2. 2d–f presents the plane-view and cross-sectional characterization of vertically aligned 2D PtSe₂ layers. The low-magnification TEM image in Figure 2. 2d shows the imaging contrast variation across the large surface of vertically aligned 2D PtSe₂ layers. The corresponding HR-STEM image (Figure 2. 2e) reveals that the entire sample area consists of a large number of crystalline grains composed of vertically aligned 2D layers. The magnified image (red box) clearly shows that vertically aligned 2D layers predominantly expose their edge sites on the surface. The interlayer spacing in

between each vertical layer is determined to be $\sim 5.2 \text{ \AA}$ which matches the (001) planar distance of the 1T-phased bulk PtSe₂ crystal.[5, 30] Figure 2. 2f reveals the cross-sectional view of the corresponding vertically aligned 2D PtSe₂ layers directly grown on a SiO₂/Si surface.

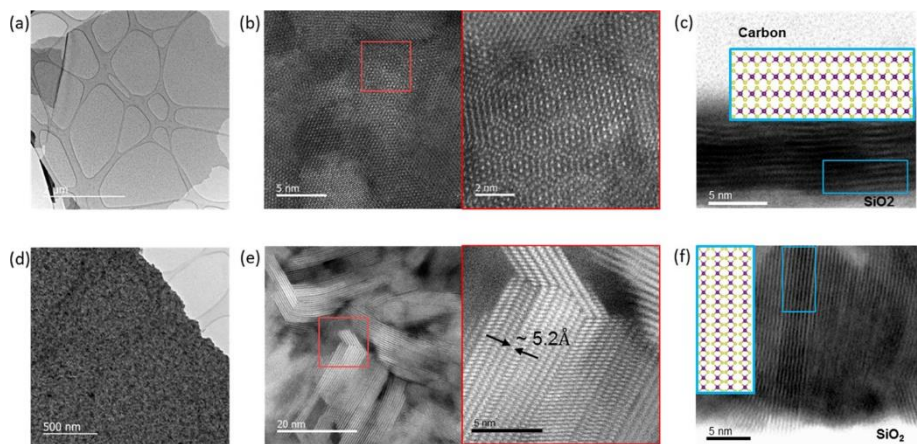


Figure 2. 2. (a–c) TEM/STEM characterization of horizontally aligned 2D PtSe₂ layers prepared with Pt of 0.75 nm; (a) low-magnification TEM. (b) HR-STEM. (c) Cross-sectional TEM. (d–f) TEM/STEM characterization of vertically aligned 2D PtSe₂ layers prepared with Pt of 8 nm; (d) low-magnification TEM. (e) HR-STEM. (f) Cross-sectional TEM.

2.1.3.3. Chemical and Electronic Structures of 2D PtSe₂ Layers

Chemical and electronic structures of 2D PtSe₂ layers were inspected by Raman spectroscopy and room-temperature carrier transport measurements. Figure 2. 3a–c presents the Raman characterization of 2D PtSe₂ layers of varying layer orientation prepared with Pt of various thicknesses. Figure 2. 4a shows the Raman spectra of 2D PtSe₂ layers obtained from the samples used for the TEM/STEM characterization. All the samples commonly exhibit two dominant Raman peaks, E_g mode at 175 cm⁻¹ (in-plane vibration of top and bottom Se atoms within an atomic layer) and A_{1g} mode at 205 cm⁻¹ (out-of-plane motions of Se atoms). The crystal structure of PtSe₂ belongs to the centrosymmetric CdI₂-type with the space group of *P3m1* (no. 164 and point group of D_{3d}).[31] The corresponding vibration modes at Γ can break into the irreducible representation of $\Gamma = A_{1g} + E_g + 2A_{2u} + 2E_u$, where the former two terms are Raman-active and the latter two terms are infrared-active.[31] The LO band dispersed from 218 to 240 cm⁻¹ is only observed with the samples prepared with Pt thickness <1 nm, which corresponds to the superposition of the A_{2u} and E_u modes contributed by the mutual motion of Pt and Se atoms vibrating along both the directions of out-of-plane and in-plane.[32] It is also noted that the Raman intensity of Si at 520 cm⁻¹ gradually decreases with increasing Pt thickness. Figure 2. 3b presents the shift of Raman energy, that is, wavenumber difference of A_{1g}–E_g, as a function of Pt thickness. The plot reveals a slight peak shift of ~1 cm⁻¹ as the orientation of 2D layers transits from horizontal to vertical, which is much smaller than those (e.g., ~10 cm⁻¹) previously observed with CVD-grown 2D PtSe₂ layers of increasing

thickness.[32] This small energy shift is a result of suppressed in-plane/out-of-plane strain in constituting 2D layers as manifested by the insignificant change in both A_{1g} and E_g phonon vibration modes. Moreover, the suppressed peak shift can be associated with the enhanced dielectric screening of Coulombic interactions in vertically aligned 2D PtSe₂ layers. For instance, the enriched 2D edge sites predominantly exposed on the surface of vertically aligned 2D TMDs are known to be highly metallic in comparison to 2D basal planes.[33] Indeed, the electrical conductivity of our vertically aligned 2D PtSe₂ layers will be confirmed by FET characterization in a later section. Figure 2. 3c presents the Raman peak intensity ratio of A_{1g}/E_g as a function of Pt thickness. The increasing peak intensity of A_{1g} over E_g in the plot clearly exhibits that the out-of-plane A_{1g} mode dominates over the in-plane E_g mode as 2D PtSe₂ layers transit from horizontal to vertical orientation. This trend is opposite to the A_{1g}/E_g characteristics observed with all horizontally aligned 2D TMDs of varying layer thickness,[34–37] but is fully consistent with the observation with vertically aligned 2D MoS₂ layers.[24, 38, 39] The crystallographic and molecular structure of 2D PtSe₂ layers verified by TEM/STEM and Raman characterization were correlated with their carrier transport properties. We fabricated FETs employing as-grown 2D PtSe₂ layers on SiO₂/Si wafers by defining chrome/gold (Cr/Au: 1 nm/70 nm) source–drain electrodes. Gate responses were assessed by utilizing the highly-doped Si handle wafer as a global back gate. Details for FET fabrication procedures are in the *Experimental Method*. Figure 2. 3d shows the plots of resistance (R) versus FET back gate voltage (V_{bg}) obtained from the 2D PtSe₂ layers corresponding

to those employed for the TEM/STEM and Raman characterization. The two-terminal resistance of 2D PtSe₂ layers gradually increases with increasing Pt thickness, similar to the previous observation with mechanically exfoliated horizontal 2D PtSe₂ of various layer numbers.[3, 9] Moreover, the gate dependence of R is clearly observed with the horizontally aligned 2D PtSe₂ layers grown with 0.75 nm Pt while all the other thicker samples exhibit no gate responses indicating the onset of transition in carrier transport characteristics. Semiconducting-to-metallic transition has been similarly observed with mechanically exfoliated horizontal 2D PtSe₂ layers of increasing layer numbers[12] as well as chemically synthesized 2D PtSe₂ films of undefined layer orientation.[3, 10, 27] This coupled structural/electrical transition of horizontal-to-vertical layer orientation accompanying tunable gate responses is further manifested in the plots shown in Figure 2. 4e. The ratio of the current obtained at $V_{bg} = \pm 60$ V and the conductance determined at $V_{bg} = 0$ V are plotted as a function of Pt thickness. The current ratio increases from unity to ~ 1.2 as the orientation of 2D PtSe₂ layers transits from vertical to horizontal while the conductance monotonously decreases. Having confirmed the electrical transition accompanying the morphological evolution in 2D PtSe₂ layers, we further investigated the gate-tunable transport characteristics only observed with thin horizontally aligned 2D PtSe₂ layers. Figure 2. 3f shows the output curve, $I_{ds}-V_{ds}$, of a FET based on horizontally aligned 2D PtSe₂ layers prepared with 0.75 nm Pt under varying back gate voltage (V_{bg}). The highly linear output characteristics indicate the good Ohmic contact of Cr/Au with the material. The source(s)-drain(d) current, I_{ds} , is observed to decrease with increasing V_{bg}

indicating *p*-type FET gate responses. This observed hole transport is consistent with recent studies on chemically synthesized 2D PtSe₂ layers[10] while *n*-type transports have also been reported varying with material preparation conditions.[3, 9, 40] Figure 2. 3g presents the gate response of the same FET device manifested by its *I*_{ds} variation as a function of *V*_{bg} along with its corresponding optical microscopy image in the inset. From the slope of the transfer curve, a FET mobility of 625 cm²/V s is determined by using the following equation at *V*_{ds} = 10 mV

$$\mu_{FE} = \frac{L}{WC_iV_{ds}} \left(\frac{dI_{ds}}{dV_{bg}} \right)$$

where *L* and *W* are channel length and width, respectively.[41] Capacitance per unit area (*C*_{*i*}) is $\epsilon_0\epsilon/t$ with relative permittivity (ϵ) and thickness of SiO₂ (*t*). This FET mobility value is order-of-magnitude higher than those of any previously reported CVD-grown 2D PtSe₂ layers,[9, 10, 27] while the FET channel is noted to be highly *p*-doped with high OFF current. The observed low ON/OFF current ratio indicates the onset of metallic-to-semiconducting transition, suggesting that 2D PtSe₂ layers have not fully transitioned to the purely semiconducting regime, possibly because of their large (~10) layer numbers (Figure 2. 2c) unlike the cases of mono-to-bilayers. Previously observed transitions of carrier transport characteristics in horizontally aligned 2D PtSe₂ layers[3, 42] have been attributed to the Se *p*-orbital coupling driven by the modulation of in-plane/out-of-plane strain with varying layer numbers. However, considering the suppressed strain effect confirmed by the Raman characterization, that is, insignificant peak shifts in Figure 2. 3b, the transition of carrier transport properties driven by 2D layer structural evolution observed

in our experiments are likely to be attributed to other mechanisms.

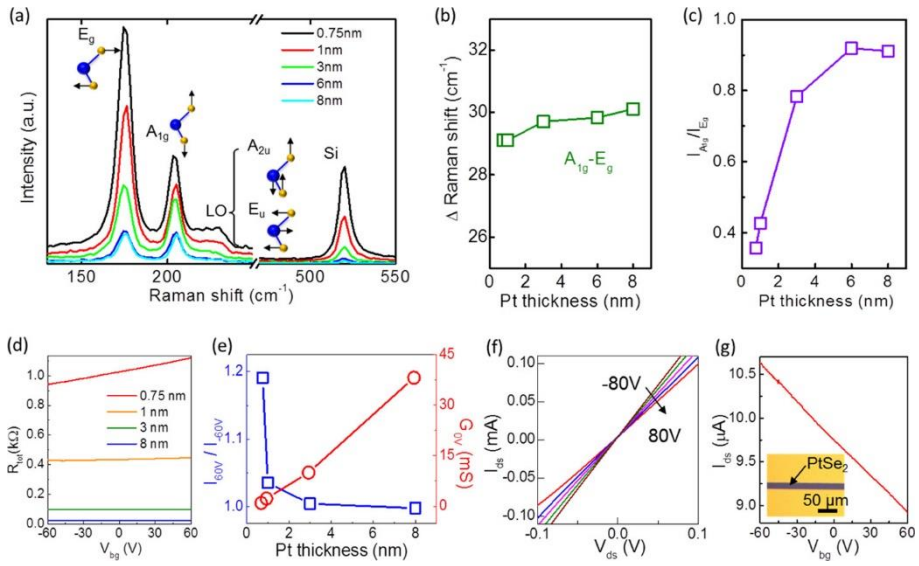


Figure 2. 3. (a) Raman profiles of 2D PtSe₂ layers prepared with Pt seeds of various thicknesses. (b) Raman peak position difference as a function of Pt thickness. (c) Raman peak intensity ratio as a function of Pt thickness. (d) Plots of R vs V_{bg} obtained from 2D PtSe₂ FETs with varying Pt thicknesses. (e) Plots of the current ratio obtained at V_{bg} = ±60 V and conductance determined at V_{bg} = 0 V as a function of Pt thickness. (f) I_{ds}-V_{ds} characteristics under varying V_{bg} (step of 40 V) obtained from horizontally aligned 2D PtSe₂ layers. (g) I_{ds}-V_{bg} characteristics obtained at V_{ds} = 10 mV from the sample corresponding to (f).

2.1.3.4. DFT calculation of various morphology and orientation 2D

PtSe₂

In order to clarify the origin for this coupled transition of electrical transport-layer orientation, we calculated the electronic structures of 2D PtSe₂ of various layer morphology and orientation. We performed *ab initio* calculation based on DFT using Vienna *ab initio* simulation package (VASP).[43] Details for simulation conditions are described in the Method section. Figure 2. 4a shows the band structures and the projected density of state (PDOS) of 2D PtSe₂ layers calculated along the K- Γ -M-K points in the hexagonal Brillouin zone. Two different cases of horizontally aligned 2D PtSe₂ monolayer and their bulk counterparts are presented. The monolayer exhibits a band gap energy of ~ 1.3 eV, while the bulk crystal shows zero band gap energy, consistent with previous theoretical studies.[4, 12, 13] We then calculated the band gap energies of vertically aligned 2D PtSe₂ layers along the Γ -X-S-Y- Γ - Z-U-R-T-Z points in the orthorhombic Brillouin zone (Figure 2. 4b-d). Vertically aligned 2D PtSe₂ layers were modeled with the fixed interlayer spacing of 5.12 Å and various vertical lengths of 7.9, 10, and 20 Å corresponding to Figure 2. 4b-d, respectively. Although the band structures become highly complicated with the increasing number of atoms within unit cells, all the vertically aligned 2D PtSe₂ layers exhibit zero band gap energies irrespective of their vertical lengths. It is noteworthy that band gap energies are already zero even with their vertical dimensions much smaller than those experimentally observed (e.g., vertical length >20 nm in Figure 2. 2f). We also studied how the morphology of vertically aligned 2D PtSe₂ layers affects their band structures by altering the

number of exposed Se atoms on their vertical edges. In addition to Figure 2. 4b–d where each 2D layer edge contains two exposed Se atoms, we calculated the band structure of vertical 2D PtSe₂ layers when one Se and one Pt atoms are exposed on their edges. Although the band structures slightly vary depending on their edge configurations, it is commonly observed that vertically aligned 2D PtSe₂ layers show metallic carrier transports with zero band gap energies. All these comprehensive experimental and theoretical results strongly confirm the transition of semiconducting-to-metallic carrier transports as the orientation of 2D PtSe₂ layers transit from horizontal to vertical. Moreover, they indicate that the band gap energies of 2D PtSe₂ layers are mainly determined by the number of stacked 2D layer basal planes.

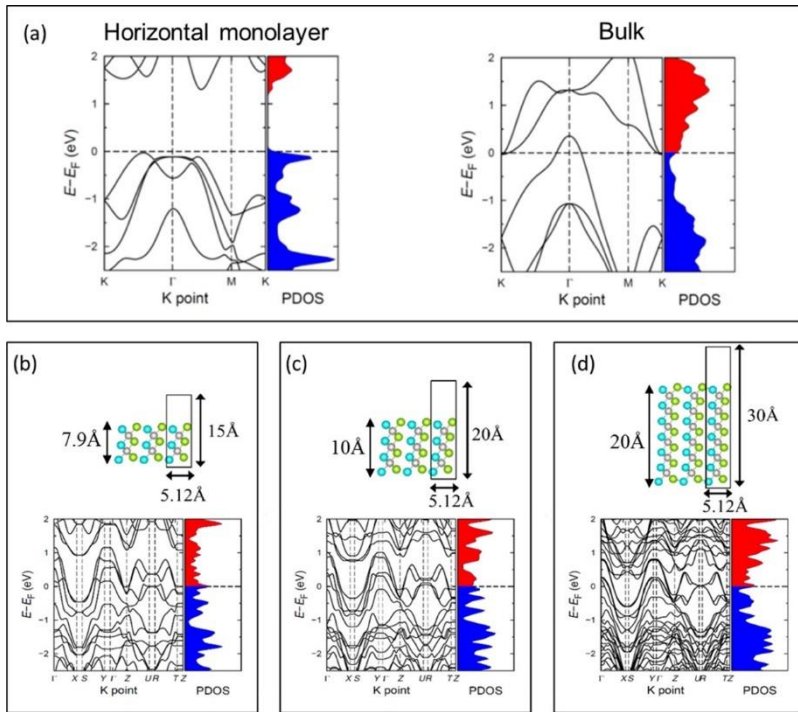


Figure 2. 4. Electronic band structures and PDOSs of PtSe₂ of various structures. (a) 2D monolayer vs bulk. (b–d) Vertically aligned 2D layers of various layer lengths of (b) 7.9 (c) 10 (d) 20 Å. Vacuum of ~ 10 Å was inserted above the vertically aligned 2D PtSe₂ layers.

2.1.3.5. The Growth Mechanism of Horizontal-to-vertical 2D Layer Transition in PtSe₂ Layer

Lastly, we discuss the growth mechanism which governs the horizontal-to-vertical 2D layer transition in PtSe₂. We have previously observed the similar layer orientation transition in 2D MoS₂ and 2D WS₂ layers[25] and investigated its fundamental principle by employing corroborating TEM characterization and molecular dynamic simulation.[46] We have identified that the seed metal (M) thickness-modulated transition of 2D layer orientation is a result of the thermodynamic interplay of M-to-2D MX₂ conversion at the initial 2D layer growth stage; MX₂ tends to rearrange its 2D layer orientation with increasing physical confinement (increasing M thickness) in a way to release the accumulating in-plane strain exerted by interconnecting 2D layers. In other words, 2D layers in vertical orientation can “freely” grow by exposing their growth fronts (i.e., 2D edges) on top of MX₂ without being interrupted by the internal strain.[46] Figure 2. 5 illustrates the two different growth scenarios for 2D PtSe₂ layers when they grow horizontally and vertically through the selenization of thin and thick Pt seeds, respectively. The growth of 2D PtSe₂ layers is carried out by the conversion of Pt into PtSe₂ which involves the volume expansion of initially deposited Pt seeds as single Pt atoms take in additional two Se atoms (Figure 2. 5a). When thin Pt seeds (typically, <1 nm in our case) are deposited on SiO₂/Si, they tend to form discontinuous nano-sized Pt islands with ample free volume in between them (Figure 2. 5b,c). Upon selenization reaction, PtSe₂ gets nucleated from Pt forming 2D layers which can efficiently fill in the free volume through their continued growth. As a result,

horizontally aligned 2D PtSe₂ layers are realized as illustrated in Figure 2. 5d. When thick Pt seeds are deposited on SiO₂/Si, they tend to form continuous films composed of networked Pt islands with diminished free volume. In this case, growing PtSe₂ will experience substantive unavailable free volume. As a result, it tends to redirect 2D layer orientation in a way to relieve the strain yielding vertically aligned 2D PtSe₂ layers as illustrated in Figure 2. 5e. Note that 2D layers can be easily bent and redirected during their growth while maintaining the interlayer vdW bond owing to high mechanical flexibility.[46] This analysis well agrees with the Raman characterization (Figure 2. 3b) which also indicates that strain is efficiently relieved as 2D PtSe₂ layers undergo horizontal-to-vertical transition, although their direct growth simulation is technically difficult at present owing to the unavailability of simulation parameters (e.g., reactive force field (ReaxFF) potential). The exact clarification of the fundamental growth mechanism and layer orientation transition in 2D PtSe₂ layers still needs further investigation.

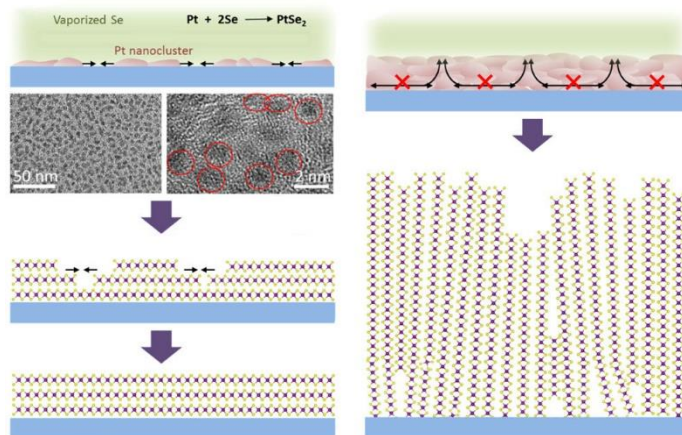


Figure 2. 5. Illustration of two different growth scenarios for 2D PtSe₂ layers; (a,b) horizontally aligned 2D PtSe₂ layers grown by the selenization of thin Pt seed layers. (a) Selenization of discontinuous Pt nanoclusters. (b) Plane-view TEM image of discontinuous Pt nanoclusters deposited on an amorphous carbon film. (c) Corresponding HRTEM image revealing crystalline Pt nanoclusters (red circles). (d) Growth of 2D PtSe₂ horizontally expanding layers filling in the free volumes in between Pt nanoclusters. (e) Vertical growth of 2D PtSe₂ layers by selenizing physically confined Pt nanoclusters of large thickness.

2.1.4. Conclusion

In conclusion, we have identified a coupled transition of structural morphology and electrical transports in 2D PtSe₂ layers by applying corroborating TEM and electrical characterization. With increasing 2D layer thickness, the layer orientation of 2D PtSe₂ transits from horizontal-to-vertical accompanying a gate-tunable transition of charge transport characteristics. FET gate responses achieved with thin horizontally aligned 2D PtSe₂ layers are manifested by the high hole mobility of ~ 625 cm²/V s determined at room temperature. The presence of this uniquely coupled structural–electrical transition verified by DFT calculation has also been demonstrated in 2D PtSe₂ layers directly grown on polymeric substrates. This study indicates that 2D PtSe₂ layers exhibit a rich set of intriguing structural and electrical properties as well as process advantages which have not been identified with other 2D TMDs.

2.1.5. Reference

- (1) Yan, M., et al. High Quality Atomically Thin PtSe₂ Films Grown by Molecular Beam Epitaxy. *2D Mater.* 2017, 4, 045015.
- (2) Guo, G. Y.; Liang, W. Y. The Electronic Structures of Platinum Dichalcogenides: PtS₂, PtSe₂ and PtTe₂. *J. Phys. C: Solid State Phys.* 1986, 19, 995–1008.
- (3) Ciarrocchi, A., et al. Thickness-Modulated Metal-to-Semiconductor Transformation in a Transition Metal Dichalcogenide. *Nat. Commun.* 2018, 9, 919.
- (4) Yao, W., et al. Direct Observation of Spin-Layer Locking by Local Rashba

Effect in Monolayer Semiconducting PtSe₂ Film. *Nat. Commun.* 2017, 8, 14216.

(5) Zeng, L.-H., et al. Fast, Self-Driven, Air-Stable, and Broadband Photodetector Based on Vertically Aligned PtSe₂/GaAs Heterojunction. *Adv. Funct. Mater.* 2018, 28, 1705970.

(6) Zeng, L., et al. Ultrafast and Sensitive Photodetector Based on a PtSe₂/Silicon Nanowire Array Heterojunction with a Multiband Spectral Response from 200 to 1550 Nm. *NPG Asia Mater.* 2018, 10, 352–362.

(7) Zhang, Z.-X., et al. Ultrafast, Self-Driven, and Air-Stable Photodetectors Based on Multilayer PtSe₂/Perovskite Heterojunctions. *J. Phys. Chem. Lett.* 2018, 9, 1185–1194.

(8) AlMutairi, A., et al. PtSe₂ Field-Effect Transistors: New Opportunities for Electronic Devices. *IEEE Electron Device Lett.* 2018, 39, 151–154.

(9) Zhao, Y., et al. High-Electron-Mobility and Air-Stable 2D Layered PtSe₂ FETs. *Adv. Mater.* 2017, 29, 1604230.

(10) Yim, C., et al. Electrical Devices from Top-Down Structured Platinum Diselenide Films. *npj 2D Mater. Appl.* 2018, 2, 5–12.

(11) Huang, H., et al. Type-I Dirac Fermions in the PtSe₂ Class of Transition Metal Dichalcogenides. *Phys. Rev. B: Condens. Matter Mater. Phys.* 2016, 94, 121117.

(12) Wang, Y., et al. Monolayer PtSe₂, a New Semiconducting Transition-Metal-Dichalcogenide, Epitaxially Grown by Direct Selenization of Pt. *Nano Lett.* 2015, 15, 4013–4018.

(13) Zhuang, H. L.; Hennig, R. G. Computational Search for Single-Layer Transition-Metal Dichalcogenide Photocatalysts. *J. Phys. Chem. C* 2013, 117, 20440–20445.

- (14) Zhang, W., et al. Two-Dimensional Semiconductors with Possible High Room Temperature Mobility. *Nano Res.* 2014, 7, 1731–1737.
- (15) Wang, Z., et al. Facile Synthesis of Single Crystal PtSe₂ Nanosheets for Nanoscale Electronics. *Adv. Mater.* 2016, 28, 10224–10229.
- (16) Radisavljevic, B., et al. Single-Layer MoS₂ Transistors. *Nat. Nanotechnol.* 2011, 6, 147–150.
- (17) Qiao, J., et al. High-Mobility Transport Anisotropy and Linear Dichroism in Few-Layer Black Phosphorus. *Nat. Commun.* 2014, 5, 4475.
- (18) Wood, J. D., et al. Effective Passivation of Exfoliated Black Phosphorus Transistors against Ambient Degradation. *Nano Lett.* 2014, 14, 6964–6970.
- (19) Atkins, P.; De Paula, J. *Physical Chemistry*; Oxford University Press: New York, 2014; pp 63–252.
- (20) Stolyarova, T. A.; Osadchii, E. G. Standard Enthalpies of Formation of Platinum Selenides PtSe₂ and PtSe_{0.8} (Pt₅Se₄) from Elements. *Geochem. Int.* 2010, 48, 91–93.
- (21) Lide, D. R. *Standard Thermodynamic Properties of Chemical Substances*. CRC Handbook of Chemistry and Physics; CRC Press, 1992.
- (22) Lee, Y.-H., et al. Synthesis of Large-Area MoS₂ Atomic Layers with Chemical Vapor Deposition. *Adv. Mater.* 2012, 24, 2320–2325.
- (23) Li, X. L.; Li, Y. D. Formation of MoS₂ Inorganic Fullerenes (IFs) by the Reaction of MoO₃ Nanobelts and S. *Chem.Eur. J.* 2003, 9, 2726–2731.
- (24) Islam, M. A., et al. Noble Metal-Coated MoS₂ Nanofilms with Vertically-Aligned 2D Layers for Visible Light-Driven Photocatalytic Degradation of Emerging Water Contaminants. *Sci. Rep.* 2017, 7, 14944.
- (25) Jung, Y., et al. Metal Seed Layer Thickness-Induced Transition from

Vertical to Horizontal Growth of MoS₂ and WS₂. *Nano Lett.* 2014, 14, 6842–6849.

(26) Yim, C., et al. High-Performance Hybrid Electronic Devices from Layered PtSe₂ Films Grown at Low Temperature. *ACS Nano* 2016, 10, 9550–9558.

(27) Su, T.-Y., et al. Phase-Engineered PtSe₂-Layered Films by a Plasma-Assisted Selenization Process toward All PtSe₂-Based Field Effect Transistor to Highly Sensitive, Flexible, and Wide-Spectrum Photoresponse Photodetectors. *Small* 2018, 14, 1800032.

(28) Xie, C., et al. High-Performance Broadband Heterojunction Photodetectors Based on Multilayered PtSe₂ Directly Grown on a Si Substrate. *Nanoscale* 2018, 10, 15285–15293.

(29) Wagner, S., et al. Highly Sensitive Electromechanical Piezoresistive Pressure Sensors Based on Large-Area Layered PtSe₂ Films. *Nano Lett.* 2018, 18, 3738–3745.

(30) Lin, S., et al. Tunable Active Edge Sites in PtSe₂ Films Towards Hydrogen Evolution Reaction. *Nano Energy* 2017, 42, 26–33.

(31) Sajjad, M.; Singh, N.; Schwingenschlögl, U. Strongly Bound Excitons in Monolayer PtS₂ and PtSe₂. *Appl. Phys. Lett.* 2018, 112, 043101.

(32) O'Brien, M., et al. Raman Characterization of Platinum Diselenide Thin Films. *2D Mater.* 2016, 3, 021004.

(33) Hu, S. Y., et al. Preparation and Characterization of Large Niobium-Doped MoSe₂ Single Crystals. *J. Cryst. Growth* 2005, 285, 408–414.

(34) Lee, C., et al. Anomalous Lattice Vibrations of Single- and Few-Layer MoS₂. *ACS Nano* 2010, 4, 2695–2700.

(35) Molina-Sánchez, A.; Wirtz, L. Phonons in Single-Layer and Few-Layer MoS₂ and WS₂. *Phys. Rev. B: Condens. Matter Mater. Phys.* 2011, 84, 155413.

- (36) Berkdemir, A., et al. Identification of Individual and Few Layers of WS₂ Using Raman Spectroscopy. *Sci. Rep.* 2013, 3, 1755.
- (37) Saito, R., et al. Raman Spectroscopy of Transition Metal Dichalcogenides. *J. Phys.: Condens. Matter* 2016, 28, 353002–353040.
- (38) Kong, D., et al. Synthesis of MoS₂ and MoSe₂ Films with Vertically Aligned Layers. *Nano Lett.* 2013, 13, 1341–1347.
- (39) Li, H., et al. Synthesis and Characterization of Vertically Standing MoS₂ Nanosheets. *Sci. Rep.* 2016, 6, 21171.
- (40) Yu, X., et al. Atomically thin Noble Metal Dichalcogenide: A Broadband Mid-Infrared Semiconductor. *Nat. Commun.* 2018, 9, 1545–1554.
- (41) Streetman, B. G. *Solid State Electronic Devices*, 4th ed.; Prentice Hall: Englewood Cliffs, 1995.
- (42) Zhao, Y., et al. Extraordinarily Strong Interlayer Interaction in 2D Layered PtS₂. *Adv. Mater.* 2016, 28, 2399–2407.
- (43) Kresse, G.; Furthmüller, J. Efficient Iterative Schemes for Ab Initio Total-Energy Calculations Using a Plane-Wave Basis Set. *Phys. Rev. B: Condens. Matter Mater. Phys.* 1996, 54, 11169–11186.
- (44) Azcatl, A., et al. HfO₂ on UV–O₃ Exposed Transition Metal Dichalcogenides: Interfacial Reactions Study. *2D Mater.* 2015, 2, 014004.
- (45) Zheng, W., et al. Kirigami-Inspired Highly Stretchable Nanoscale Devices Using Multidimensional Deformation of Monolayer MoS₂. *Chem. Mater.* 2018, 30, 6063–6070.
- (46) Choudhary, N., et al. Strain-Driven and Layer-Number-Dependent Crossover of Growth Mode in Van Der Waals Heterostructures: 2D/2D Layer-by-Layer Horizontal Epitaxy to 2D/3D Vertical Reorientation. *Adv. Mater. Interfaces* 2018, 5, 1800382–1800391.

(47) Kresse, G.; Joubert, D. From Ultrasoft Pseudopotentials to the Projector Augmented-Wave Method. *Phys. Rev. B: Condens. Matter Mater. Phys.* 1999, 59, 1758–1775.

(48) Perdew, J. P.; Burke, K.; Ernzerhof, M. Generalized Gradient Approximation Made Simple. *Phys. Rev. Lett.* 1996, 77, 3865–3868.

(49) Perdew, J. P.; Burke, K.; Ernzerhof, M. Generalized Gradient Approximation Made Simple. *Phys. Rev. Lett.* 1997, 78, 1396.

2.2. Growth Behavior and Properties of 2D PtTe₂ Layers

The contents of this section have been published in: Mengjing Wang, Tae-Jun Ko, Mashiyat Sumaiya Shawkat, Sang Sub Han, Emmanuel Okogbue, Hee-Suk Chung, Tae-Sung Bae, Shahid Sattar, Jaeyoung Gil, Chanwoo Noh, Kyu Hwan Oh, YounJoon Jung, J. Andreas Larsson and Yeonwoong Jung “Wafer-Scale Growth of 2D PtTe₂ with Layer Orientation Tunable High Electrical Conductivity and Superior Hydrophobicity” ACS Appl. Mater. Interfaces 12, 10839–10851 (2020).

2.2.1. Introduction

Among Pt-based 2D chalcogenides, Pt ditelluride (PtTe₂) is an emerging material, which has been identified to possess unusual band structures and topological properties.[1–16] Recent experiments report that 2D PtTe₂ is a type-II Dirac semimetal with a strongly tilted Dirac cone along Γ -A direction, projecting intriguing quantum phenomena such as anisotropic magnetism and topological transition.[7] Moreover, the theory predicts that it transits to a semiconductor with a small bandgap of 0.4 eV only when it is in a monolayer form.[8] Furthermore, an unusually high electrical conductivity of 106-107 S/m and large break-down current density have been observed in chemically synthesized PtTe₂ crystals.[9–11] In addition to this intrinsically semi-metallic nature, 2D PtTe₂ is projected to exhibit high chemical reactivity suitable for hydrogen evolution reaction,[12, 13] further justifying its rich novelty beyond conventional 2D TMDCs. Despite such projected advantages, scalable and controllable chemical synthesis of 2D PtTe₂ with well-defined layer orientation and material properties has not been established so far. Accordingly, a systematic understanding of its structure–property–process relationship has been lacking, impeding to unveil a full range of its intriguing attributes.

Existing methods for fabricating 2D PtTe₂ layers include (1) chemical vapor transport growth of bulk PtTe₂ crystals at 1000 °C through self-reflux and subsequent mechanical exfoliation,[13] (2) simultaneous evaporation of platinum tetrachloride (PtCl₄) or Pt and tellurium (Te) powders at a temperature range of ~800–1100 °C,[9, 10] and (3) eutectic liquid synthesis of Pt–Te solid solutions at 700 °C.[11] A major drawback common in these approaches is that they yield 2D PtTe₂ layers of limited size (i.e., typically ~5–20 μm) as well as uneven spatial distribution and surface coverage. Moreover, the adopted synthesis temperature is high and even comparable to those for conventional 2D TMDCs (e.g., 2D molybdenum disulfide) despite the much lower melting temperature of Pt over refractory metals (e.g., Mo).[14]

In this study, we report a low-temperature growth of 2D PtTe₂ layers on a large area greater than a few square centimeters by reacting Pt thin films of controlled thickness with vaporized Te at 400 °C. We systematically studied the thickness dependency of their growth orientation on resulting structural and electrical properties via comprehensive scanning transmission electron microscopy (STEM), X-ray diffraction (XRD), and electrical characterization. We unveil that 2D PtTe₂ layers accompany thickness-dependent distinct growth modes: (1) layer-by-layer horizontal growth, (2) transition of horizontal-to-vertical layer orientation, and (3) mixture of horizontal and vertical growth. The underlying growth mechanism is discussed in the context of competition between growth kinetics and strain energy release, analogous to the transition of Frank–van der Merwe (FM) to Stranski–Krastanov (SK) growths established in three-dimensional (3D) epitaxial thin-film models. We also characterized the

electrical conductivity of these orientation-controlled 2D PtTe₂ layers and identified its thickness dependency. 2D PtTe₂ multilayers of an optimum thickness exhibit the highest conductivity of $\sim 1.7 \times 10^6$ S/m, which is attributed to the excellent structural homogeneity of all horizontally aligned 2D layers as evidenced by cross-sectional STEM and XRD. The conductivity gradually decreases with increasing thickness while it still remains to be superior to those of any previously developed 2D TMDCs.[15–17] This thickness-dependent electrical property in conjunction with the variation of 2D layer orientation indicates a pronounced contribution of out-of-plane electron transports with increasing 2D vertical alignment. Finally, we performed water contact angle (WCA) measurements with 2D PtTe₂ layers of varying thickness and identified their surface wettability. An intrinsically high hydrophobicity was identified by a large WCA value up to $\sim 117^\circ$, significantly higher than the values observed with other 2D TMDCs of comparable lateral dimensions.[18–20] These comprehensive studies suggest the high structural and electrical quality of centimeter-scale 2D PtTe₂ layers and unveil an exclusive role of their layer orientation on governing such attributes.

2.2.2. Experimental Method

2.2.2.1. Synthesis of 2D PtTe₂ Layers

Pt seeds of controlled thickness were deposited on SiO₂/Si wafers (300 nm; SiO₂ thickness) by an electron beam evaporator (Thermionics VE-100) at a fixed evaporation rate of 0.15 Å/s. Pt-deposited SiO₂/Si substrates were placed in the center zone of a quartz tube inside a thermal furnace (Lindberg/Blue M Mini-Mite), and an alumina boat containing Te powder was placed at the

furnace upstream side (temperature ~ 200 °C). Following Ar purging down to a base pressure of ~ 1 mTorr, the furnace subsequently ramped up to the growth temperature of 400 °C at a rate of 7.6 °C/min was maintained for 50 min. During the growth reaction, the flow rate of Ar gas was kept being ~ 100 standard cubic centimeters per minute (SCCM) at a pressure of ~ 80 mTorr.

2.2.2.2. TEM Characterization and Analysis

The structural and chemical integrity of as-grown 2D PtTe₂ layers was characterized using FEI F30 TEM (operation voltage: 300 kV) and JEOL ARM 200F Cs-corrected TEM (operation voltage: 200 kV). For plane-view TEM sample preparation, the buffered oxide etchant was directly applied to as-prepared 2D PtTe₂-SiO₂/Si substrates and the separated 2D PtTe₂ layers were manually integrated onto copper TEM grids. Cross-sectional TEM samples were prepared using a focused ion beam (FIB: Quanta 2D FEG, FEI) employing Ga ion beam (30 keV)- based TEM lift-out techniques. The atomic simulation of the Moiré pattern was obtained by stacking two monolayers with a misorientation angle of 30° and was visualized in Vesta atomic visualization program. Geometrical phase analysis (GPA) of the HAADF-STEM image was performed using a built-in Digital Micrograph script.[30]

2.2.2.3. XRD Characterization

X-ray diffraction of 2D PtTe₂ films on SiO₂/Si wafers was carried out by a PANalytical Empyrean diffractometer equipped with a copper X-ray source ($K\alpha_1 = 1.5406$ Å, $K\alpha_2 = 1.54439$ Å) and a Pixel3D detector. Diffraction data were collected under an operation tension of 45 kV and a current of 40 mA using theta-two theta scan geometry.

2.2.2.4. Electrical Characterization

All electrical measurements were performed with a home-built probe station using a HP 4156 A semiconductor parameter analyzer. Gold was evaporated on top of as-grown 2D PtTe₂ layers on SiO₂/Si substrates through a metal shadow mask for electrode patterning.

2.2.2.5. AFM Characterization

A tapping mode AFM (Anasys Instruments, NanoIR2) scanning was carried out to reveal the topography of 2D PtTe₂ layers at a scan rate of 0.3 Hz. The AFM probe (model: PR-EX-T125-10) has a resonant frequency of 200–400 kHz and a spring constant of 13–77 N/m.

2.2.2.6. Computational Details

We use density functional theory with the projector augmented wave method[47, 48] as implemented in the Vienna *ab-initio* Simulation Package.[34] The generalized gradient approximation in the Perdew-Burke-Ernzerh of parametrization is employed for the exchange-correlation potential, and the plane wave cutoff energy is set to a sufficiently large value of 420 eV. The vdW interaction is taken into account using the nonlocal optB86b-vdW density functional.[61,62] A γ -centered Monkhorst-Pack $12 \times 12 \times 1$ ($9 \times 9 \times 2$) k-mesh is used for the structural relaxation, whereas for self-consistent calculations, the Brillouin zone integration is performed using a dense $20 \times 20 \times 1$ ($11 \times 11 \times 3$) k-mesh for horizontally (vertically) aligned 2D PtTe₂, respectively. We ensure an energy convergence of 10^{-6} eV and force convergence of 10^{-3} eV/Å for the iterative solution of the Kohn-Sham equations. Due to the constituent heavy elements involved in PtTe₂, the effects

of spin-orbit coupling are always taken into account in our calculations. We also use a 15 Å thick layer of vacuum on top of both horizontally and vertically aligned 2D PtTe₂ layers to exclude spurious interaction between periodic images in the out-of-plane direction as three-dimensional periodic boundary conditions are applied. The results are plotted using the Matplotlib software package.[51]

2.2.3. Results and Discussion

2.2.3.1. Growth and Structural Analysis of PtTe₂ Layers

2D dichalcogenides employing group X noble metals such as PtSe₂ and PtTe₂ preferably adopt the 1T configuration rather than the 2H.[8] Figure 2. 6a illustrates that 1T-PtTe₂ possesses a space group of P3m1 as presented in its perspective (left), side (mid), and top (right) views. Each Te–Pt–Te layer constitutes edges-connected octahedra, with one representative octahedron as outlined in the pink regions of the side and top views. Figure 2. 6b illustrates the schematic setup and the procedure for 2D PtTe₂ layer growth. SiO₂/Si wafers covered with Pt films of a controlled thickness (i.e., ~0.5–15 nm) are reacted at 400 °C with vaporized Te under a continued supply of Argon (Ar) flow gas. Details for growth conditions are presented in the *Experimental Section*. Figure 2. 6c shows an image of a SiO₂/Si substrate with as-grown 2D PtTe₂ layers (1 cm × 6 cm). Figure 2. 6d shows a representative high angle annular darkfield (HAADF) STEM image of a 2D PtTe₂ basal plane revealing its 1T configuration. Figure 1e shows the intensity profile along the red line in Figure 2. 6d, indicating the periodic spatial distribution of Pt and Te atoms. The

superimposed atomic configuration in Figure 2. 6d and the intensity fluctuation in Figure 2. 6e are fully consistent with the atomic model presented in Figure 2. 6a. Figure 1f shows a representative crosssection STEM image of 2D PtTe₂ layers revealing a stacking sequence of 1T Te–Pt–Te atomic chains with an interlayer spacing of 0.52 nm corresponding to the lattice constant c. Figure 2. 6g shows a large-area STEM image of 2D PtTe₂ multilayers with horizontally aligned layers of high homogeneity, highlighting their excellent crystallinity and layer orientation control. Energy dispersive X-ray spectroscopy (EDS) in Figure 2. 6h further validates that the synthesized 2D PtTe₂ layers possess a stoichiometry of Pt/Te = 1:2. Additional EDS spectra, elemental mapping images, and EDS line scan profiles were obtained from 2D PtTe₂ layers prepared with various Pt film thicknesses, i.e., from 0.5 to 15 nm. The data confirm that the Pt/Te = 1:2 stoichiometry is well retained irrespective of the variation in initial Pt thickness, indicating the complete conversion of Pt to 2D PtTe₂.

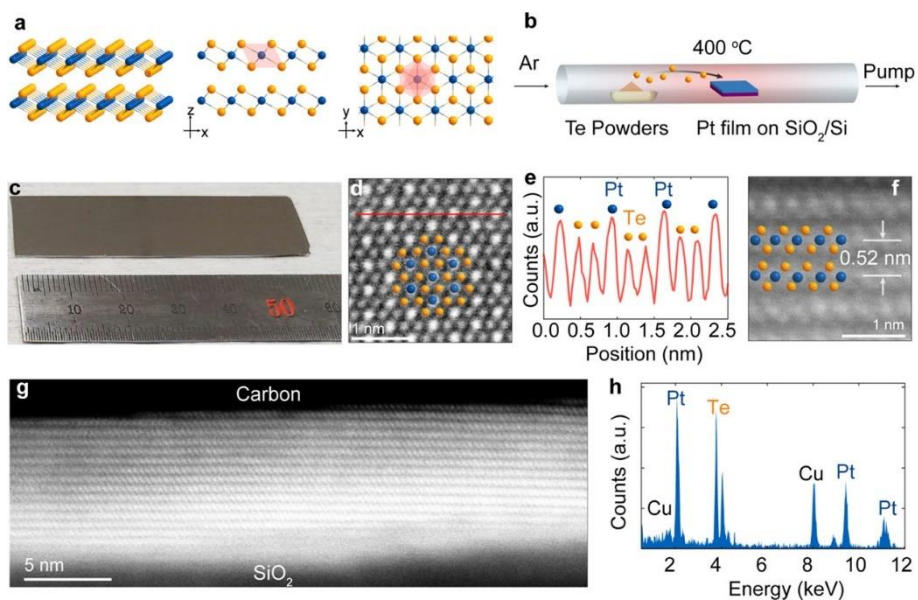


Figure 2. 6. (a) Perspective (left), side (mid), and top (right) views of 1T-PtTe₂. Orange and blue balls represent Te and Pt atoms, respectively. The pink-shaded areas in the side and top views illustrate an octahedron atomic configuration. (b) Schematic illustration of the 2D PtTe₂ layer growth apparatus and procedure. (c) Camera image of a PtTe₂ sample on a SiO₂/Si wafer with a size of 1 cm × 6 cm. (d) Plane-view HAADF-STEM image of a 2D PtTe₂ basal plane. (e) Intensity profile corresponding to the red line in (d). (f) Cross-sectional HAADF-STEM image of 2D PtTe₂ layers with an interlayer spacing of 0.52 nm. (g) Representative cross-sectional STEM image of large-area, horizontally aligned 2D PtTe₂ multilayers. (h) EDS spectrum revealing a stoichiometry of Pt/Te = 1:2.

2.2.3.2. Orientation Controlled Growth and the Mechanism of Orientation Transition of PtTe₂ Layers

We systematically grew 2D PtTe₂ layers by tellurizing Pt films of varying thickness and characterized their morphological transition. Figure 2. 7a–c illustrates the morphology of 2D PtTe₂ layers obtained with Pt thin films in three different thickness regimes, i.e., small (e.g., ~0.5 nm) for Figure 2. 14a, intermediate (e.g., ~1–3 nm) for Figure 2. 7b, and large (e.g., >6 nm) for Figure 2. 7c. These values denote the “nominal” thickness of deposited Pt films set by their e-beam evaporation conditions, and its correlation with the experimentally verified actual thickness of 2D PtTe₂ layers is to be presented in the following section. In conjunction with the thickness variation of Pt films, three different growth modes have been observed. Growth mode (i) in Figure 2. 7a: Holey PtTe₂ films composed of horizontally aligned 2D layers are obtained by tellurizing Pt films of ~0.5 nm thickness. This is a consequence that depositing Pt films of such a small thickness form scattered Pt nanoclusters of low areal density (top). As a result, 2D PtTe₂ layers grow without entirely covering the substrate surface (mid and bottom). Growth mode (ii) in Figure 2. 7b: Continuous PtTe₂ films composed of all horizontally aligned 2D layers are obtained by tellurizing Pt films of ~1–3 nm thickness. Tellurizing Pt nanoclusters of a much higher area density (top) convert them to continuous 2D PtTe₂ layers, which laterally expand covering the free spaces on the substrate We grew 2D PtSe₂ layers by selenizing Pt-deposited SiO₂/Si substrates (mid and bottom). Growth mode (iii) in Figure 2c: Continuous PtTe₂ films constituting a mixture of horizontally and vertically aligned 2D layers are

obtained by tellurizing continuous Pt films of >6 nm thickness (top). Conversion of the continuous Pt films to 2D PtTe₂ layers involves a significant volume expansion since Pt atoms take in additional Te atoms as well as forming vdW physical gaps. Accordingly, growing 2D PtTe₂ layers will experience a substantial amount of accumulating strain, and some of their crystalline domains will prefer to reorient 2D layers in a vertical manner to release the strain (mid and bottom). This growth event is similar to the recently observed and verified strain-driven vertical growth of 2D MoS₂ layers.[21] Figure 2. 7d–i presents STEM characterization to verify the thickness-dependent 2D PtTe₂ layer morphological transition. Figure 2. 7d–f shows low-magnification STEM images of 2D PtTe₂ layers obtained from various Pt thicknesses of ~ 0.5 , ~ 3 , and ~ 15 nm. Figure 2. 7d reveals that 2D PtTe₂ layers indeed exhibit rich porosity (red arrow), while the others show their continuous film morphology. 2D PtTe₂ layers in Figure 2. 7d present an average domain size of ~ 50 nm with a spatial coverage ratio of $\sim 74\%$, supporting their conversion from scattered Pt nanoclusters of low density illustrated in Figure 2. 7a. It is also noted that 2D PtTe₂ layers grown from the larger Pt thickness (Figure 2. 7e) exhibit higher STEM imaging contrast over the other (Figure 2.7 f), indicating significant inhomogeneity of 2D layer orientation. Figure 2. 7g–l presents HAADF-STEM characterization of 2D PtTe₂ layers obtained with various Pt thickness. Figure 2. 7g shows a high-resolution HAADF-STEM image obtained from holey 2D PtTe₂ layers, revealing highly crystalline domains along with a grain boundary. The measured lattice spacing of 0.20 nm corresponds to (110) lattice fringes exposed on PtTe₂ basal planes, indicative of horizontally aligned 2D layers.

Figure 2. 7h shows a representative high-resolution HAADF-STEM image of continuous 2D PtTe₂ layers obtained from Pt thin films of intermediate thickness. The image reveals three crystalline domains of distinct crystallographic orientation, while (110) lattice fringes are uniformly observed in each grain. This observation indicates that horizontally aligned individual 2D layers of distinct orientation laterally “stitch” in an in-plane manner, evidencing their layer-by-layer growth nature. Figure 2. 7i shows a representative high-resolution HAADF-STEM image of 2D PtTe₂ layers obtained from Pt thin films of a much larger thickness (15 nm, in this case). Unlike the other cases, which confirm the layer-by-layer stitching of horizontally aligned 2D layers, we note distinct lattice fringes corresponding to (001) planes confirmed by the measured spacing of 0.52 nm. This observation indicates that crystalline domains are formed in the way that 2D PtTe₂ layers grow upright in a vertical orientation, as illustrated in Figure 2. 14c. In Figure 2. 7i, the crystalline domain on the upper right corner is on-axis with respect to 2D layer orientation, while the others are slightly off-axis, which results in location-dependent imaging contrast difference. Figure 2. 7j–l presents representative cross-sectional STEM images highlighting the distinct growth mode and orientation transition in 2D PtTe₂ layers. Figure 2. 7j reveals a high-resolution STEM image of horizontally aligned 2D layers where the arrows denote laterally terminated 2D layers on their top surface, directly evidencing the layer-by-layer stitching growth mode. Figure 2. 7k displays a local area on 2D PtTe₂ multilayers of ~10 nm thickness, evidencing the transition of horizontal-to-vertical layer orientation (blue and red insets). Figure 2. 7l shows a representative cross-sectional STEM image of

2D PtTe₂ multilayers of larger thickness. The inset reveals crystalline domains composed of vertically slanted 2D layers that expose their edge sites on the surface, corresponding to the in-plane STEM image in Figure 2. 7i. Despite the growth mode variation, the average size of individual 2D PtTe₂ layer particles is nearly similar, i.e., ~40–60 nm, irrespective of the variation in initial Pt thickness, which is attributed to the similar size distribution of individual Pt nanoparticle obtained with identical e-beam deposition conditions.

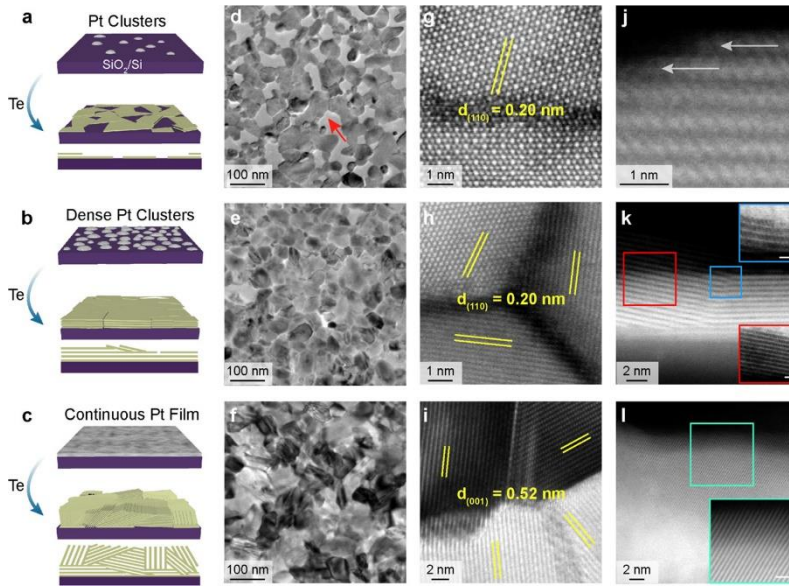


Figure 2. 7. (a–c): Schematics for growth characteristics of 2D PtTe₂ layers obtained by tellurizing (a) scattered Pt nanoclusters, (b) dense Pt nanoclusters, and (c) continuous Pt films. The mid and bottom rows of (a, b, and c) represent projected and side-views of resulting 2D PtTe₂ layers, respectively. (d–f): HAADF-STEM images of (d) holey layers with the pores indicated by the red arrow, (e) continuous layers, and (f) continuous layers with pronounced imaging contrast. (g–i): High-resolution HAADF-STEM images of (g) (110) lattice fringes in crystalline grains with a grain boundary, (h) (110) lattice fringes from crystalline 2D basal planes of three distinct orientations, and (i) (001) lattice fringes denoting 2D layer vertical orientation. (j–l): Cross-sectional STEM images of (j) edge-terminated horizontally aligned 2D layers, (k) reorientation of 2D layers along with the top and bottom insets corresponding to the blue and red boxed regions, and (l) vertically aligned 2D layers along with the inset corresponding to the green boxed region. The scale bars of the insets are 1 nm.

The underlying mechanism, which dictates the thickness-dependent orientation transition of 2D PtTe₂ layers, is discussed in the context of competition between thermodynamic and kinetic driving forces. In general, the growth of 2D PtTe₂ layers should be driven to lower its associated thermodynamic energy, while it is simultaneously limited by the diffusion kinetics of Te atoms and the tellurization reaction rate. The growth mode (i) employs the tellurization of scattered and well-exposed Pt nanoclusters, which must be highly reactive, imposing low diffusion barriers for Te atoms. Thus, the kinetic effect should be insignificant, and the thermodynamic driving force favors to expose 2D basal planes of low surface energy, resulting in horizontally aligned 2D PtTe₂ layers. While the surface coverage and dimension of Pt clusters are further increased (growth mode (ii)), the horizontal growth mode is still retained owing to a sufficient amount of free volumes in between them. Accordingly, 2D PtTe₂ multilayers of high structural homogeneity and full coverage are generated upon tellurizing Pt films of a certain critical thickness, as demonstrated in Figure 2. 6g. Beyond this critical point where thicker Pt films become tellurized, a substantial amount of internal strain will start to accumulate particularly along the grain boundaries of 2D PtTe₂ layers where 2D layers of distinct orientation converge. To release this additional strain energy during the course of continued growth, 2D PtTe₂ layers start to adjust their layer orientation off the horizontal direction by entering the growth mode (iii). Given the high density and volume of Pt films in this case, diffusion of Te atoms into them becomes challenging and rate limiting compared to growth mode (ii) at such a low growth temperature of 400 °C. Accordingly, the growth

mode (iii) is believed to be driven by kinetic factors, as verified by the significantly faster diffusion of chalcogen atoms along the surface-exposed vdW gaps of vertically aligned 2D layers over 2D basal planes.[18, 23, 24]

We note that this thickness-dependent transition of PtTe₂ layer orientation from “2D-like horizontal” to “3D-like vertical” is analogous to the growth characteristics established in 3D epitaxial thin films, i.e., the transition from Frank–van der Merwe (FM) growth to Stranski–Krastanov (SK) growth.[25, 26] Despite the seemingly similar characteristics, it is necessary to point out that the growth principles for the conventional thin-film epitaxy vs. 2D PtTe₂ layer growth are fundamentally different at molecular levels. The epitaxial growth adopted in conventional thin-film technologies such as molecular beam epitaxy generally relies on the deposition and crystallization of gaseous molecular precursors. Meanwhile, the growth of 2D PtTe₂ layers proceeds through the transformation of solid-phase Pt films through their reaction with gaseous tellurium. 2D PtTe₂ layers grown from the tellurization of thin Pt films preferably expose 2D basal planes of high atomic packing density, lowering the total thermodynamic energy. This event is akin to the FM mode, which predicts 2D layer-by-layer growth accompanying the exposure of atomically smooth and fully covered surfaces, as previously verified in thin-film epitaxial growth studies.[27] Following the initial growth of 2D multilayers driven by the FM mode, a nontrivial amount of strain energy subsequently accumulates particularly across sites of high structural inhomogeneity.[25, 26, 28] Above a certain layer thickness, this strain leads to a transition of FM-to-SK growth mode forming Volmer–Weber islands (vertically aligned 2D layers, in this

case), which are energetically more favorable.[29] This 3D thin-film epitaxy model well matches the growth characteristics observed with our 2D PtTe₂ layers of varying thickness, explaining the existence of a certain critical Pt thickness regime (~1–3 nm) above which vertically aligned 2D layers start to emerge.

The above growth mechanism analysis indicates the presence of a substantial amount of internal strain exerted by 2D layers of distinct crystallographic orientation. We hypothesize that such strain should significantly accumulate along the grain boundaries where 2D PtTe₂ layers with distinct orientations impeach each other during lateral volume expansion.[14] To experimentally verify this prediction, we analysis (GPA)[30, 31] to the STEM images of horizontally aligned PtTe₂ layers obtained with Pt of 1 nm thickness, right below the regime where vertically aligned 2D layers dominantly emerge. Figure 2. 8a shows a representative DFSTEM image (left) from a location rich with grain boundaries formed by three distinct grains (denoted A, B, and C) as well as its corresponding FFT image (right). Three sets of hexagonally packed diffraction spots distinguished by the color shading in the FFT correspond to each individual grain in the STEM image. Figure 2. 8b–d demonstrates the spatial strain distribution along the three sets of grain boundaries formed by grains of A–B (Figure 2. 8b), C–A (Figure 2. 8c), and B–C (Figure 2. 8d) as well as their corresponding FFTs. We identify that dislocations with displacements of atoms are localized along the grain boundaries of high strain concentration, consistent with other GPA studies of dislocations.[32,33] In the strain mapping images of Figure 2. 8b–d, the white squares denote the areas

where dislocations under high strains are localized, manifested by the dark blue and bright yellow color. It is noteworthy that a larger misorientation angle between grains yields a higher linear density of dislocation cores at the grain boundaries. For instance, the areal density of dislocation cores associated with the misorientation angle of 24.8° (Figure 2. 8d) is noticeably higher than that with 10.5° (Figure 2. 8c). The observation is consistent with recent studies on the strain distribution along the grain boundaries within horizontally stacked 2D MoS₂ layers, evidenced by the identical GPA method.[32] This analysis directly evidences a significant amount of strain accumulation globally occurring within these intrinsically polycrystalline 2D PtTe₂ layers. A histogram of misorientation angles between individual grains was obtained from the sample prepared with the Pt film of 0.5 nm, which indicates an absence of specifically preferred angle values. Furthermore, it is worth pointing out that the strain effect should become more pronounced with growths from Pt films of larger thickness accompanying larger grain sizes.

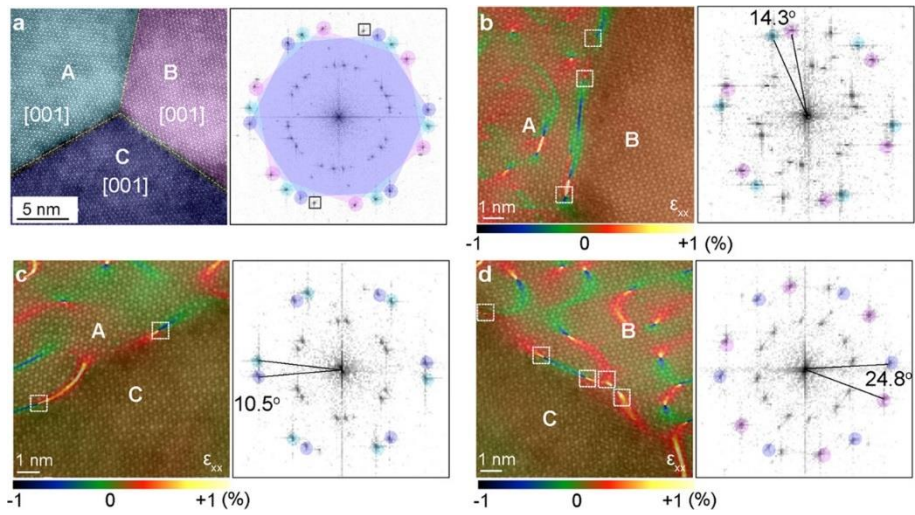


Figure 2. 8. (a) DF-STEM image (left) and corresponding FFT pattern (right) of horizontally aligned 2D PtTe₂ multilayers constituting three crystalline grains composed of basal planes with distinct orientations. The blue, cyan, and pink-shaded spots in the FFT correspond to the grains denoted by the identical color in the DF-STEM image. The black squared diffraction spots in the FFT originate from the layer underneath the grains of A, B, and C. (b–d) GPA mapping and corresponding FFTs of grain boundaries formed by grains of (b) A + B, (c) C + A, and (d) B + C. The white dashed squares in (b–d) denote the dislocation cores exhibiting high strain.

To further elucidate the thickness-dependent crystallographic transition of 2D PtTe₂ layers, we employed diffraction characterization techniques, including X-ray diffraction (XRD) and TEM electron diffraction. Figure 2. 9a, b shows XRD characterization of 2D PtTe₂ layers obtained from Pt films of varying thickness. With small enough thickness (<6 nm), 2D PtTe₂ layers preferably adopt horizontally aligned layers. This is evidenced by the strong (001) crystalline peaks in Figure 2. 9a, indicating the dominant coverage of 2D basal planes on the growth substrate while weak (003) peaks also appear. With Pt films of larger thickness, 2D PtTe₂ layers gradually start to adopt vertically aligned and slanted layers. Crystalline planes other than (001) and (003), such as (101), (102), (110), and (111), start to emerge, which becomes more pronounced with larger thickness. Interestingly, the 2D PtTe₂ layers obtained from 15 nm Pt exhibit a strong (101) peak intensity with a significantly suppressed (001) peak, a sharp contrast to the characteristics observed in those with Pt thickness <6 nm. This observation indicates that vertically aligned 2D layers significantly dominate over horizontal orientation, consistent with the TEM observations in Figure 2. 9i–l. Further quantification was carried out by measuring the XRD intensity ratio of (101) over (001) peaks as a function of Pt film thickness, as presented in Figure 2. 9b. It is evident that there is a sharp increase in the peak intensity ratio entering the 6 nm regime and beyond, indicating an onset of horizontal-to-vertical transition in 2D layer orientation as denoted by the blue and red shading, respectively. In addition to observed peak intensity attenuation, the (001) peak becomes more sharpened with increasing initial Pt film thickness, which is majorly contributed to the increase of

crystallite size along (001) direction. Moreover, XRD characterization was performed to a thick Pt film of 15 nm before and after its tellurization. In the XRD data, Pt crystal peaks completely vanish and only PtTe₂ peaks appear after the tellurization, which further validates the complete conversion of Pt to 2D PtTe₂ layers even with this large Pt thickness. TEM selected area electron diffraction (SAED) analysis was carried out to correlate the macroscopic observation by XRD with the microstructure of 2D PtTe₂ layers. Figure 2. 9c shows a representative STEM image of 2D PtTe₂ layers obtained from 1 nm Pt thickness, belonging to the horizontal orientation regime. Figure 2. 9d presents its corresponding SAED characterization revealing a strong (110) ring pattern along the [001] zone axis, which indicates the dominant exposure of 2D basal planes on the surface consistent with Figure 2.7h. Figure 2. 9e shows a representative STEM image of 2D PtTe₂ layers obtained from 6 nm Pt thickness, belonging to the horizontal-to-vertical transition regime. Figure 2. 9f presents its corresponding SAED characterization where the indexed diffraction patterns indicate a presence of both [001] and [010] zone axes, corroborating with the XRD result in Figure 2. 9a.

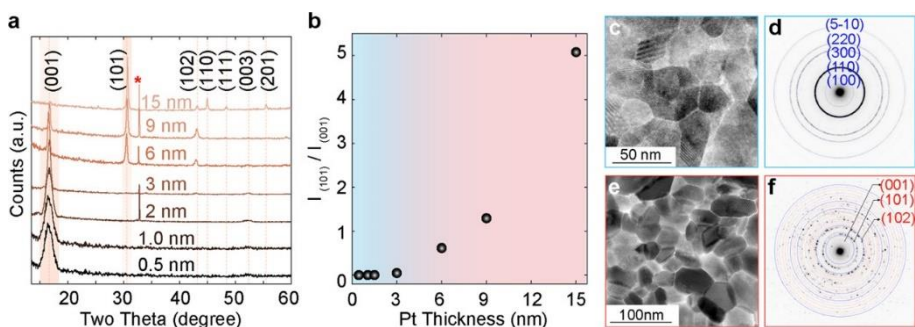


Figure 2. 9. (a) XRD characterization of 2D PtTe₂ layers grown from Pt films of varying thickness. The red star mark denotes peaks from the growth substrate. (b) XRD peak intensity ratio of I(101)/I(001) as a function of Pt film thickness. (c) Representative STEM image of crystalline grains constituting horizontally aligned 2D PtTe₂ layers. (d) Corresponding SAED pattern indicating that the indexed diffraction rings are normal to the [001] zone axis. (e) Representative STEM image of crystalline grains constituting a mixture of horizontally and vertically aligned 2D PtTe₂ layers. (f) Corresponding SAED pattern indicating a presence of both [001] and [101] zone axes. The blue highlighted diffraction rings correspond to those presented in (d), highlighting the crystallographic distinction of horizontally vs. vertically aligned 2D PtTe₂ layers.

2.2.3.3. DFT calculation for various morphology and orientation of 2D

PtTe₂ Layers

From the above comprehensive structural characterization, we identified a thickness-dependent transition of 2D PtTe₂ layer morphology and orientation, which indicates a possibility of thickness dependency in material properties such as electron transports. Herein, we systematically investigated electrical performances of 2D PtTe₂ layers with varying thickness and identified a potential influence of 2D layer orientation on them, particularly of vertical orientation. We first identified their electronic band structures by performing first-principles calculations. To be consistent with the experimentally realized 2D PtTe₂ layer structures, we focused our calculations on horizontally aligned 2D PtTe₂ multiple layers and vertically aligned 2D PtTe₂ layers of varying lengths using the Vienna *ab initio* Simulation Package[34] (see Computational Details in *the Experimental Section*). Horizontally aligned 2D PtTe₂ layers of varying layer numbers from tri-layer (3L) to hexa-layer (6L) are modeled, and Figure 2. 10a shows a schematic view of representative penta-layer (5L) PtTe₂. The optimized lattice constant a for 3L–6L PtTe₂ turns out to be in the range of 4.045–4.051 Å with a Pt–Pt interlayer distance ($d_{\text{Pt-Pt}}$) of 5.25 Å, which is in close agreement to the experimentally observed value of 0.52 nm. Corresponding electronic band structures plotted along the high-symmetry line ($M - \Gamma - K - M$) are given in Figure 2. 10b, which clearly depicts the metallic nature of horizontally aligned 2D PtTe₂ multilayers irrespective of their layer number. Furthermore, we show the atomic projected density of state (PDOS) plots and found mixed contributions from both Pt and Te atomic states around

the Fermi level. We next address the case of vertically aligned 2D PtTe₂ layers, as shown in Figure 2. 10c, d. Fixing the Pt–Pt interlayer distance to 5.25 Å identical to the case of horizontally aligned layers, we consider an orthorhombic unit cell of various edge configurations, i.e., Te-terminated edges in Figure 2. 10c and Pt-terminated edges in Figure 2. 10d. The electronic band structures plotted along the high-symmetry line (Γ -Z-S-B- Γ -A-E-Z-D) in Figure 2. 10c, d demonstrate the metallic behavior of vertically aligned 2D PtTe₂ layers regardless of edge configurations. This finding of the metallic nature of vertically aligned 2D PtTe₂ layers remains unchanged even with further increasing their vertical layer length. We systematically grew for the sake of complete-ness, we also calculated the band structures of PtTe₂ in monolayer and bulk forms. Consistent with previous density functional theory (DFT) studies,[8] 2D PtTe₂ layers exhibit a bandgap of ~ 0.8 eV when they are in a monolayer form while they are metallic in a bulk form. Indeed, it is known that 2D PtTe₂ layers are semiconducting only when they possess monolayers unlike other Pt-based 2D chalcogenides such as 2D PtSe₂, which can be still semiconducting with few-to-several layers.[25]

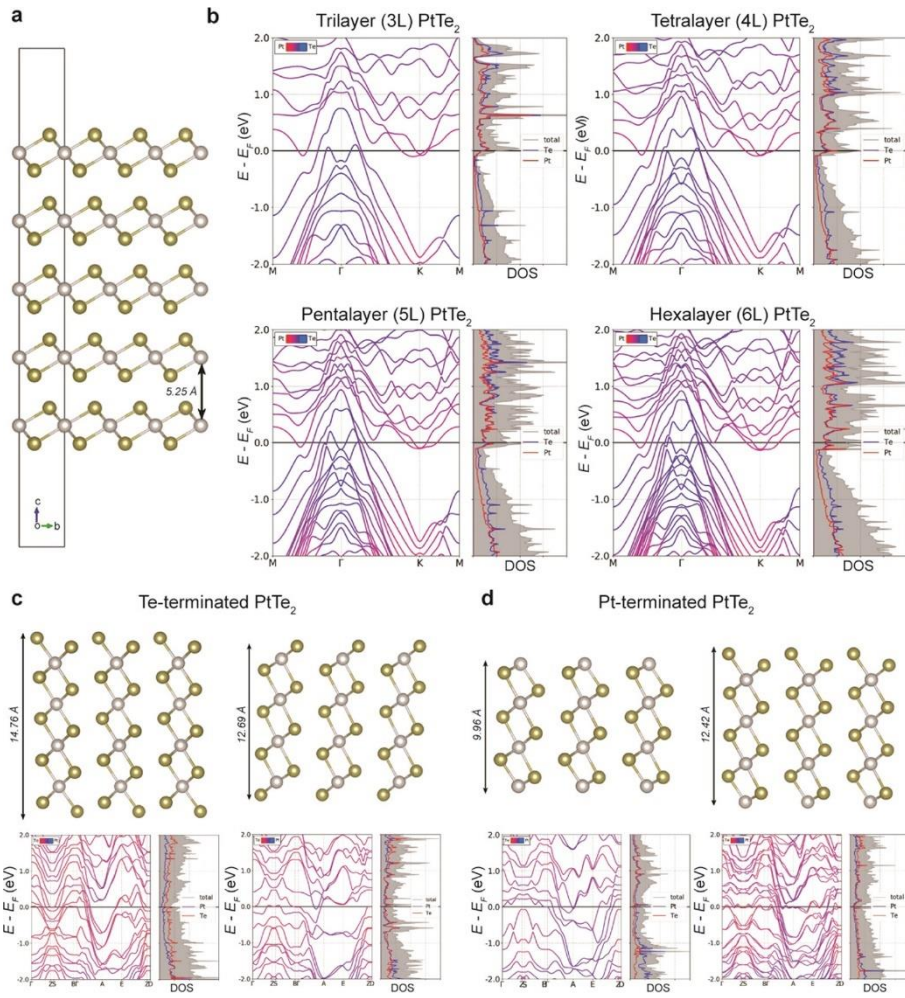


Figure 2. 10. (a) Side view of penta-layer (5L) PtTe_2 as a representative system for horizontally aligned multilayers. (b) Electronic band structure and DOS plots for 3L–6L. (c) Side view (top) and electronic band structures (bottom) of vertically aligned 2D PtTe_2 with Te-terminated edge configurations. (d) Side view (top) and electronic band structures (bottom) of vertically aligned 2D PtTe_2 with Pt-terminated edge configurations.

2.2.3.4. Electronic Structures of 2D PtTe₂ Layers

We then experimentally studied the thickness-dependent electrical performances of 2D PtTe₂ layers. We first identified the relationship of Pt film thickness and resulting 2D PtTe₂ layer thickness by performing atomic force microscopy (AFM) height profile measurements, as presented in Figure 2. 11a. We note that the actual thickness of 2D PtTe₂ layers is ~5 times larger than the nominal thickness of Pt films, which is set by the deposition conditions inherent to our e-beam evaporator. We then investigated the carrier type of as-grown 2D PtTe₂ layers on SiO₂/Si wafers by characterizing their field-effect transistor (FET) gate responses. From various theory studies[8] and our DFT calculation results, it is well established that 2D PtTe₂ layers do not possess bandgap energies even in a few-layer form. We thus focused our measurements on 2D PtTe₂ layers obtained from Pt films of a very small thickness (e.g., ~0.5 nm corresponding to a 2D layer thickness of ~2.5 nm), as presented in Figure 2. 11b, c. Figure 2. 11b shows transfer characteristics of drain-source voltage (V_{ds}) vs. drain-source current (I_{ds}) with varying back-gate voltage (V_g), and Figure 2. 11c shows I_{ds} - V_g at varying V_{ds} . As anticipated, 2D PtTe₂ layers reveal strong metallic characteristics, as manifested by the complete overlap of $I_{ds} - V_{ds}$ irrespective of V_g (Figure 2. 11b) and the V_g -independent I_{ds} (Figure 2. 11c). The inset in Figure 2. 11b illustrates a schematic of 2D PtTe₂ layer-based FET in a back-gate configuration. Having confirmed the intrinsically metallic nature of 2D PtTe₂ layers, we investigated their thickness-dependent electron transports. For rigorous quantification, we precisely defined the geometrical dimension of 2D PtTe₂ layers by AFM characterization of their actual thickness

(Figure 2. 11a) and by patterning gold (Au) electrodes with an identical channel length (width: 200 μm , spacing: 100 μm). Figure 2. 11d shows I–V characteristics obtained from 2D PtTe₂ layers of varying Pt thickness, and Figure 2. 11e presents the corresponding electrical conductance obtained from their tangential slopes. Electrical conductivity was determined by combining the geometrical dimension with the measured conductance, and its thickness-dependency is presented in Figure 2. 11f. With increasing Pt thickness, the conductivity steadily increases yielding the highest value of $\sim 1.7 \times 10^6$ S/m at ~ 3 nm thickness. This thickness is the critical point where 2D PtTe₂ multilayers exhibit horizontally aligned layer orientation with full surface coverage and high structural homogeneity. The lower conductivity value from a smaller Pt thickness is attributed to their intrinsically holey morphology (Figure 2. 7a, d). Beyond this critical point, vertically aligned 2D layers start to emerge as confirmed by the XRD (Figure 2. 9a) and STEM/SAED (Figure 2. 9c, d) characterization. With further increasing thickness, the conductivity gradually decreases reaching $\sim 1.4 \times 10^6$ S/m at Pt thickness of 15 nm. This thickness-dependent conductivity decrease well agrees with the thickness-dependent transition of 2D layer orientation, i.e., emergence of vertically aligned 2D layers beyond a certain critical thickness continuously becomes more pronounced with further increasing thickness (Figure 2. 11a, b). This suppressed conductivity from the vertically aligned 2D layers is attributed to the increasing contribution of “out-of-plane” transports of electrons across vdW physical gaps, as illustrated in Figure 2. 11g. This observation is well supported by previous experimental and theoretical studies that report much higher energy

barriers for the electrons undergoing out-of-plane transports across vdW gaps over those traveling in an “in-plane” manner.[36, 37] It is also worth mentioning that the overall conductivity values are on the order of 10^6 S/m, highly comparable to those of previously reported 2D PtTe₂ layers of much smaller dimensions, which fall in the range of $3.3\text{--}6.4 \times 10^6$ S/m (Table 2. 1).[9–11] Moreover, these conductivity values are significantly higher than those of any other 2D TMDC layers, e.g., the highest reported being vanadium diselenide (VSe₂) with a conductivity of $\sim 1 \times 10^6$ S/m[38] (Table 2. 1). Such an unusual combination of extremely high electrical conductivity, wafer-scale dimension, and tunable geometry offers numerous opportunities beyond applications of electronics, e.g., electrochemical or catalytic applications requiring high electrical conductivity coupled with large structural porosity and surface area.

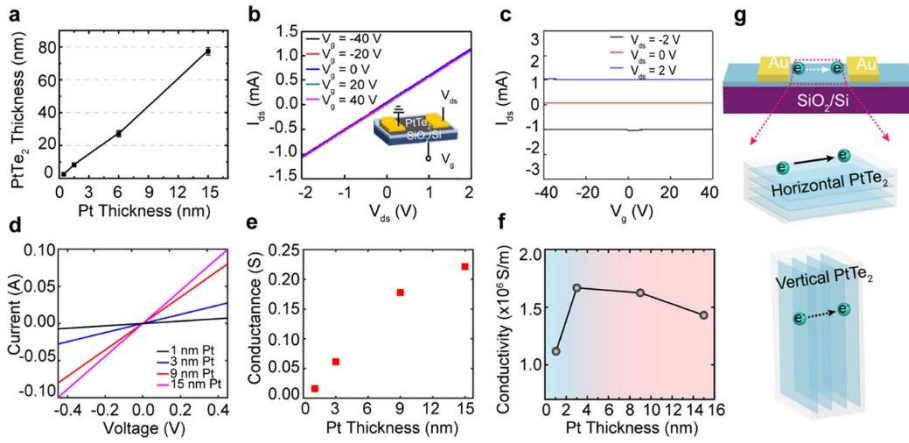


Figure 2. 11. (a) Thickness of 2D PtTe₂ layers as a function of Pt thickness. (b, c) Back-gate FET measurements of 2D PtTe₂ layers obtained from ~ 0.5 nm Pt thickness, showing (b) $I_{ds}-V_{ds}$ and (c) $I_{ds}-V_g$ transfer characteristics. (d) $I-V$ curves of 2D PtTe₂ prepared from various Pt thicknesses. (e) Conductance as a function of Pt thickness. (f) Conductivity as a function of Pt thickness showing a presence of its thickness-dependent maximum point. The junction of the blue and red shading represents a transition of horizontal-to-vertical layer orientation. (g) Schematics of electron transports in horizontally vs. vertically aligned 2D PtTe₂ layers.

2D Material	Synthetic Method	Conductivity (S/m)	Reference
PtTe ₂	Chemical vapor deposition (PtCl ₄ + H ₂ + Te ₂)	6.4×10^6	1
	Chemical vapor deposition (Pt + Te powders)	2.5×10^6	2
	Eutectic synthesis	3.3×10^6	3
	Tellurization of Pt film	1.7×10^6	Our work
VS ₂	CVD	3×10^5	4
VSe ₂	CVD	$\sim 1 \times 10^6$	5
1T-MoS ₂	Chemical exfoliation	$\sim 10^3 - 10^4$	6
NiTe ₂	CVD	7.8×10^5	7

Table 2. 1. Room-temperature conductivity values for horizontally-aligned 2D PtTe₂ layers synthesized via various approaches and other representative conductive 2D TMDCs.

2.2.4. Conclusion

To conclude, we report a scalable growth of 2D PtTe₂ layers at a low temperature of 400 °C by tellurizing Pt films of controlled thickness. We observed their thickness-dependent transition of layer morphology and orientation, confirmed by extensive TEM, STEM, XRD, and electron diffraction characterization. The transition is identified to result from a competing interplay of thermodynamic and kinetic factors where an internal strain accumulating during the course of 2D layer growth plays a critical role. This thickness-dependent morphological transition in 2D PtTe₂ layers is correlated with their electrical conductivity, which exhibits a maximum at a certain critical thickness regime after which it steadily decreases. The electrical conductivity values of 2D PtTe₂ layers, as well as their WCA values, are much higher than those of any other previously explored 2D TMDCs, confirming high material quality. Accordingly, this study is believed to pave the way for investigations of novel quantum phenomena in this relatively less-explored Dirac semimetal of a large area.

2.2.5. Reference

- (1) Politano, A., et al. 3D Dirac Plasmons in the Type-II Dirac Semimetal PtTe₂. *Phys. Rev. Lett.* 2018, 121, No. 086804.
- (2) Deng, K., et al. Crossover from 2D Metal to 3D Dirac Semimetal in Metallic PtTe₂ Films with Local Rashba Effect. *Sci. Bull.* 2019, 64, 1044–1048.
- (3) Fu, D., et al. Quantum Oscillations in Type-II Dirac Semimetal PtTe₂. *Phys. Rev. B* 2018, 97, No. 245109.

- (4) Zhang, K., et al. Experimental Evidence for Type-II Dirac Semimetal in PtSe₂. *Phys. Rev. B* 2017, 96, No. 125102.
- (5) Huang, H., et al. Type-II Dirac Fermions in the PtSe₂ Class of Transition Metal Dichalcogenides. *Phys. Rev. B* 2016, 94, No. 121117(R).
- (6) Bahramy, M. S., et al. Ubiquitous Formation of Bulk Dirac Cones and Topological Surface States from a Single Orbital Manifold in Transition-Metal Dichalcogenides. *Nat. Mater.* 2018, 17, 21–27.
- (7) Yan, M., et al. Lorentz-Violating Type-II Dirac Fermions in Transition Metal Dichalcogenide PtTe₂. *Nat. Commun.* 2017, 8, No. 257.
- (8) Villaos, R. A. B., et al. Thickness Dependent Electronic Properties of Pt Dichalcogenides. *npj 2D Mater. Appl.* 2019, 3, No. 2.
- (9) Fu, L., et al. Highly Organized Epitaxy of Dirac Semimetallic PtTe₂ Crystals with Extrahigh Conductivity and Visible Surface Plasmons at Edges. *ACS Nano* 2018, 12, 9405–9411.
- (10) Ma, H., et al. Thickness-Tunable Synthesis of Ultrathin Type-II Dirac Semimetal PtTe₂ Single Crystals and Their Thickness-Dependent Electronic Properties. *Nano Lett.* 2018, 18, 3523–3529.
- (11) Hao, S., et al. Low-Temperature Eutectic Synthesis of PtTe₂ with Weak Antilocalization and Controlled Layer Thinning. *Adv. Funct. Mater.* 2018, 28, No. 1803746.
- (12) Chia, X., et al. Layered Noble Metal Dichalcogenides: Tailoring Electrochemical and Catalytic Properties. *ACS Appl. Mater. Interfaces* 2017, 9, 25587–25599.
- (13) Chia, X., et al. Layered Platinum Dichalcogenides (PtS₂, PtSe₂, and PtTe₂) Electrocatalysis: Monotonic Dependence on the Chalcogen Size. *Adv. Funct. Mater.* 2016, 26, 4306–4318.

- (14) Jung, Y., et al. Metal Seed Layer Thickness-Induced Transition from Vertical to Horizontal Growth of MoS₂ and WS₂. *Nano Lett.* 2014, 14, 6842–6849.
- (15) Ji, Q., et al. Metallic Vanadium Disulfide Nanosheets as a Platform Material for Multifunctional Electrode Applications. *Nano Lett.* 2017, 17, 4908–4916.
- (16) Acerce, M., et al. Metallic 1T Phase MoS₂ Nanosheets as Supercapacitor Electrode Materials. *Nat. Nanotechnol.* 2015, 10, 313–318.
- (17) Park, S.; Ruoff, R. S. Chemical Methods for the Production of Graphenes. *Nat. Nanotechnol.* 2009, 4, 217–224.
- (18) Gaur, A. P. S., et al. Surface Energy Engineering for Tunable Wettability through Controlled Synthesis of MoS₂. *Nano Lett.* 2014, 14, 4314–4321.
- (19) Chow, P. K., et al. Wetting of Mono and Few-Layered WS₂ and MoS₂ Films Supported on Si/SiO₂ Substrates. *ACS Nano* 2015, 9, 3023–3031.
- (20) Son, S. B., et al. Ultraviolet Wavelength-Dependent Optoelectronic Properties in Two-Dimensional NbSe₂–WSe₂ Van Der Waals Heterojunction-Based Field-Effect Transistors. *ACS Appl. Mater. Interfaces* 2017, 9, 41537–41545.
- (21) Choudhary, N., et al. Strain-Driven and Layer-Number-Dependent Crossover of Growth Mode in van Der Waals Heterostructures: 2D/2D Layer-By-Layer Horizontal Epitaxy to 2D/3D Vertical Reorientation. *Adv. Mater. Interfaces* 2018, 5, No. 1800382.
- (22) Wang, L., et al. New Generation of Moiré Superlattices in Doubly Aligned HBN/Graphene/HBN Heterostructures. *Nano Lett.* 2019, 19, 2371–2376.
- (23) Deokar, G., et al. Large Area Growth of Vertically Aligned Luminescent MoS₂ Nanosheets. *Nanoscale* 2017, 9, 277–287.

- (24) Stern, C., et al. Growth Mechanisms and Electronic Properties of Vertically Aligned MoS₂. *Sci. Rep.* 2018, 8, No. 16480.
- (25) Bauer, E.; Poppa, H. Recent Advances in Epitaxy. *Thin Solid Films* 1972, 12, 167–185.
- (26) Grabow, M. H.; Gilmer, G. H. Thin Film Growth Modes, Wetting and Cluster Nucleation. *Surf. Sci.* 1988, 194, 333–346.
- (27) Lang, O., et al. Single Crystalline GaSe/WSe₂ heterointerfaces Grown by van Der Waals Epitaxy. I. Growth Conditions. *J. Appl. Phys.* 1994, 75, 7805–7813.
- (28) Schell-Sorokin, A. J.; Tromp, R. M. Mechanical Stresses in (Sub)Monolayer Epitaxial Films. *Phys. Rev. Lett.* 1990, 64, 1039–1042.
- (29) Thompson, C. V., et al. Epitaxial Grain Growth in Thin Metal Films. *J. Appl. Phys.* 1990, 67, 4099–4104.
- (30) Kim, K.-H. Digital Micrograph Script Source Listing for a Geometric Phase Analysis. *Appl. Microsc.* 2015, 45, 101–105.
- (31) Hÿtch, M. J.; Snoeck, E.; Kilaas, R. Quantitative Measurement of Displacement and Strain Fields from HREM Micrographs. *Ultramicroscopy* 1998, 74, 131–146.
- (32) Elibol, K., et al. Grain Boundary-Mediated Nanopores in Molybdenum Disulfide Grown by Chemical Vapor Deposition. *Nanoscale* 2017, 9, 1591–1598.
- (33) Sun, C., et al. Atomic and Electronic Structure of Lomer Dislocations at CdTe Bicrystal Interface. *Sci. Rep.* 2016, 6, No. 27009.
- (34) Kresse, G.; Joubert, D. From Ultrasoft Pseudopotentials to the Projector Augmented-Wave Method. *Phys. Rev. B: Condens. Matter Mater. Phys.* 1999, 59, 1758–1775.

- (35) Ciarrocchi, A., et al. Thickness-Modulated Metal-to-Semiconductor Transformation in a Transition Metal Dichalcogenide. *Nat. Commun.* 2018, 9, No. 919.
- (36) Yu, Y., et al. Layer-Dependent Electrocatalysis of MoS₂ for Hydrogen Evolution. *Nano Lett.* 2014, 14, 553–558.
- (37) Cappelluti, E., et al. Tight-Binding Model and Direct-Gap/Indirect-Gap Transition in Single-Layer and Multilayer MoS₂. *Phys. Rev. B: Condens. Matter Mater. Phys.* 2013, 88, No. 075409.
- (38) Zhang, Z., et al. Van Der Waals Epitaxial Growth of 2D Metallic Vanadium Diselenide Single Crystals and Their Extra-High Electrical Conductivity. *Adv. Mater.* 2017, 29, No. 1702359.
- (39) Choi, B. K., et al. Tunable Wetting Property in Growth Mode-Controlled WS₂ Thin Films. *Nanoscale Res. Lett.* 2017, 12, No. 262.
- (40) Kozbial, A., et al. Study on the Surface Energy of Graphene by Contact Angle Measurements. *Langmuir* 2014, 30, 8598–8606.
- (41) Kumar, P.; Viswanath, B. Horizontally and Vertically Aligned Growth of Strained MoS₂ Layers with Dissimilar Wetting and Catalytic Behaviors. *CrystEngComm* 2017, 19, 5068–5078.
- (42) Agrawal, A. V., et al. Controlled Growth of MoS₂ Flakes from In-Plane to Edge-Enriched 3D Network and Their Surface-Energy Studies. *ACS Appl. Nano Mater.* 2018, 1, 2356–2367.
- (43) Quéré, D. Wetting and Roughness. *Annu. Rev. Mater. Res.* 2008, 38, 71–99.
- (44) Owens, D. K.; Wendt, R. C. Estimation of the Surface Free Energy of Polymers. *J. Appl. Polym. Sci.* 1969, 13, 1741–1747.

- (45) Guo, G. Y.; Liang, W. Y. The Electronic Structures of Platinum Dichalcogenides: PtS₂, PtSe₂ and PtTe₂. *J. Phys. C: Solid State Phys.* 1986, 19, 995–1008.
- (46) Li, Y. X., et al. Two-Dimensional MTe₂ (M = Co, Fe, Mn, Sc, Ti) Transition Metal Tellurides as Sodium Ion Battery Anode Materials: Density Functional Theory Calculations. *Phys. Lett. A* 2018, 382, 2781–2786.
- (47) Blöchl, P. E. Projector Augmented-Wave Method. *Phys. Rev. B* 1994, 50, 17953–17979.
- (48) Kresse, G.; Furthmüller, J. Efficient Iterative Schemes for Ab Initio Total-Energy Calculations Using a Plane-Wave Basis Set. *Phys. Rev. B: Condens. Matter Mater. Phys.* 1996, 54, 11169–11186.
- (49) Klimeš, J., et al. Chemical Accuracy for the van Der Waals Density Functional. *J. Phys.: Condens. Matter* 2010, 22, No. 022201.
- (50) Klimeš, J., et al. Van Der Waals Density Functionals Applied to Solids. *Phys. Rev. B: Condens. Matter Mater. Phys.* 2011, 83, No. 195131.
- (51) Hunter, J. D. Matplotlib: A 2D Graphics Environment. *Comput. Sci. Eng.* 2007, 9, 90–95.

Chapter 3. Transfer and Integration of 2D TMDs

Layers

3.1. Water-assisted Transfer method for 2D TMDs Layers

The contents of this section have been published in: Jung Han Kim, Tae-Jun Ko, Emmanuel Okogbue, Sang Sub Han, Mashiyat Sumaiya Shawkat, Md Golam Kaium, Kyu Hwan Oh, Hee-Suk Chung & Yeonwoong Jung “Centimeter-scale Green Integration of Layer-by-Layer 2D TMD vdW Heterostructures on Arbitrary Substrates by Water-Assisted Layer Transfer” Scientific Reports volume 9, Article number: 1641 (2019)

3.1.1. Introduction

As 2D TMD layers exert weak van der Waals (vdW) attraction to underlying growth substrates, it is possible to individually assemble them in a layer-by-layer manner achieving targeted electronic structures, implying new venues for 2D heterojunction devices with tailored band offsets.[1–5] Such atom thick semiconductor heterostructures have been technically challenging to integrate with conventional thin film growth strategies owing to their intrinsic lattice match constraint which imposes the crystallographic limitation for the choice of materials to be integrated. A few critical prerequisites exist in order to realize the aforementioned advantages inherent to 2D TMDs toward their exploration for novel technologies; (1) It is demanded to develop viable strategies to transfer 2D TMD layers from original growth substrates and integrate them on secondary substrates of targeted functionalities, e.g., mechanically flexible substrates. (2) The intrinsic mechanical and electrical properties of the transferred 2D layers should not be compromised throughout their integration process and should be uniformly preserved on a wafer scale. (3) The layer

integration process should be generalized to 2D TMDs and substrates of diverse materials without being limited to specific kinds for technological versatility. Presently, the most commonly employed approach for the transfer and integration of 2D TMD layers relies on the chemical etching of underlying growth substrates involving protection polymers (e.g., polymethylmethacrylate (PMMA)) and subsequent chemical lift-off.[6–8] However, such strategies tend to result in the fragmentation of individual 2D layers as they employ solution-based chemicals to etch away both the protection layer and growth substrates (e.g., silicon dioxide (SiO₂) or sapphire wafer).[7] Accordingly, they impose scalability limitation in terms of heterogeneously stacking up 2D layers of multiple components in a controlled manner as well as being difficult to be applied to a variety of unconventional substrates. Moreover, the intrinsic material properties of 2D layers are often compromised and damaged by the employed chemicals though their transfer and integration stages.

In this study, we report a generic and reliable strategy to achieve the layer-by-layer integration of 2D TMDs of controlled morphology and component onto arbitrary substrates over a large area. The newly developed 2D layer integration method is intrinsically “green” as it employs water only without involving any other chemicals, thus is free of any chemicals-associated material degradation. We demonstrate the layer-by-layer integration of centimeter-scale (>2 cm²) uniform 2D TMDs and their heterostructures onto virtually arbitrary substrates including, papers, woods, and plastics, which is difficult to achieve with any conventional approaches. The integrated 2D TMD layers and their

heterostructures well preserve their original structural and compositional integrity benefiting from the intrinsic cleanness of the water-assisted process, confirmed by extensive spectroscopy and microscopy characterization. The technological versatility of this 2D layer integration method has been demonstrated by developing large-area 2D TMDs-based flexible photodetectors and pressure sensors on plastics and papers, respectively.

3.1.2. Experimental Method

3.1.2.1. Synthesis of 2D TMDs Films

Various 2D TMD layers were grown via the sulfurization or selenization of transition metals deposited on SiO₂/Si substrates using a home-built CVD chamber (Lindberg/Blue M Mini-Mite). High-quality transition metals (e.g., Mo, W, Pt) were deposited on cleaned SiO₂/Si wafers (typical dimension: ~1 × 3 cm²) using an e-beam evaporation system (Thermionics VE-100). The metal deposited SiO₂/Si substrates were placed at the center zone of the CVD furnace while alumina boats containing S or Se powders were located at the upstream side. After the furnace was evacuated to the base pressure of ~1 mTorr, high purity Ar gas was flushed for ~10 min to remove any residuals in the chamber. The CVD furnace was gradually ramped up to reach the targeted growth temperatures, i.e., 800 °C for MoS₂ and WSe₂, and 400 °C for PtSe₂, while the S and Se powders were vaporized at ~200 °C. The reaction was maintained for ~45 min under a constant supply of Ar gas at a flow rate of 100 sccm (standard cubic centimeter per minute) followed by natural cooling.

3.1.2.2. Structural Characterization

TEM characterization was performed using a JEOL ARM200F Cs-corrected

TEM at an accelerating voltage of 200 kV. TEM samples were prepared by transferring 2D TMD films from SiO₂/Si substrates to TEM grids by using water without compromising their intrinsic material quality of as-grown states. Cross-sectional TEM samples (2D MoS₂ in Figure 3. 2 and 2D MoS₂/WSe₂ vertical-stack in Figure 3. 5) were prepared by focused ion beam (FIB)-based milling and lift-out techniques. Raman characterization was performed using a Renishaw system with a solid-state laser (spot size: 1 μm) at the excitation wavelength of 532 nm. Optical microscopy images were recorded in an Olympus BX60M optical microscope.

3.1.3. Results and Discussion

3.1.3.1. Procedure of Water-assisted 2D TMDs Layer Integration

Figure 3. 1 schematically depicts the integration of large-area 2D TMDs onto a variety of substrates via the water-assisted 2D layer transfer. The process is carried out in following steps: (1) Deposition of transition metals on the surface of growth substrates (i.e., SiO₂/Si) followed by their conversion to 2D TMD layers via chemical vapor deposition (CVD). (2) Immersion of the 2D TMDs grown SiO₂/Si substrates inside water followed by spontaneous 2D layer separation. (3) Transfer and integration of the delaminated 2D TMD layers onto secondary substrates inside water. (4) Recycling of the original growth substrates for additional 2D TMDs growth (optional). Details for the CVD growth of 2D TMDs are described in Methods section. The water-assisted 2D layer separation can be carried out in following two slightly different manners. The first method is to slowly immerse the entire 2D TMDs-grown substrate inside water while the second method is to deposit water droplet only on the

sample surface to leverage its buoyancy. We emphasize that the whole process utilizes water only without involving any kinds of additional chemicals for the separation, transfer, and integration of 2D TMD layers. Previous approaches generally employed the combined use of polymeric protective materials (e.g., PMMA or Polyvinyl alcohol (PVA)) and chemical etchants for the removal of SiO_2 . [7, 8] In addition to the operational complexity inherent to these conventional approaches, 2D TMDs are susceptible to chemical degradation owing to the corrosive nature of hydrogen fluoride (HF) or strong bases (sodium or potassium hydroxide (NaOH or KOH)) involved in the processes. [6, 8] Moreover, their structural integrity can be significantly altered by the solution-based chemicals (e.g. acetone) employed to rinse away the protective polymers as well as being affected by the polymer residuals. On the other hand, our water-assisted approach yields the completely clean and homogenous integration of a variety of 2D TMDs on a large centimeter scale (to be demonstrated below). As this approach is intrinsically free of introducing chemicals-associated structural damage, the original SiO_2/Si substrates after 2D layer separation can be reused for the subsequent growth of additional 2D TMD materials (step (4) in Figure 3. 1).

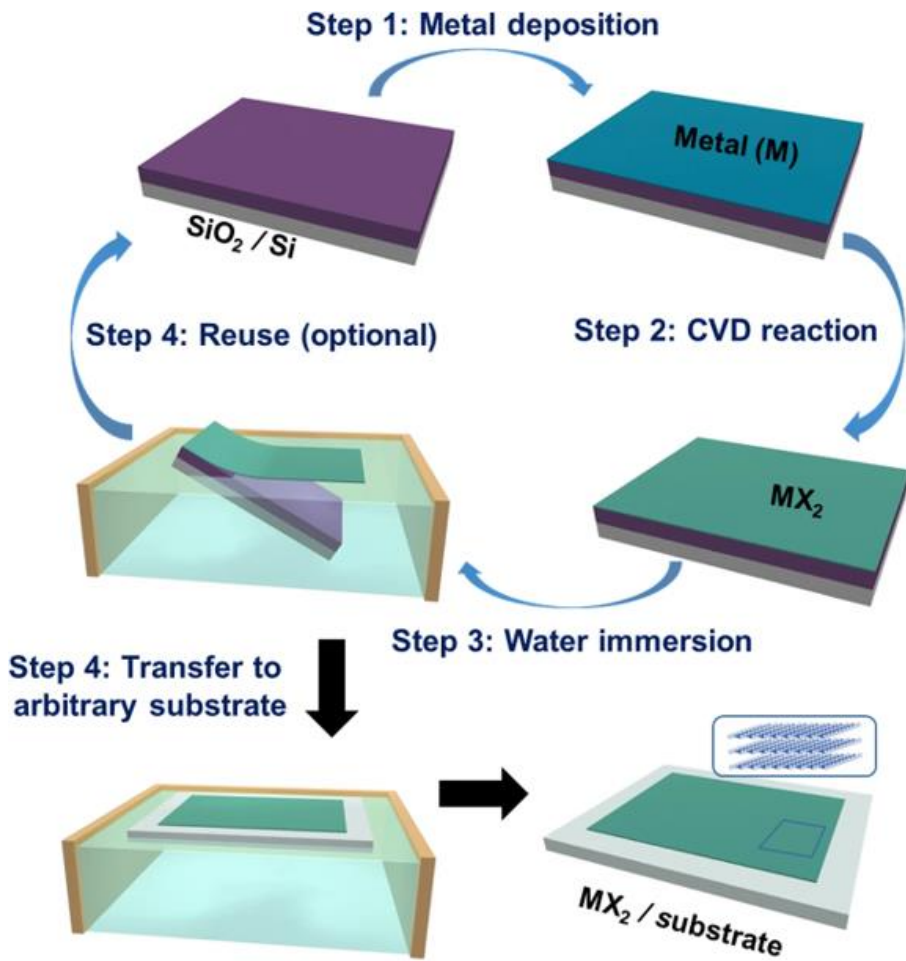


Figure 3. 1. Schematic to illustrate the water-assisted green integration of CVD-grown 2D TMD layers on arbitrary substrates.

3.1.3.2. Demonstration of Water-assisted 2D TMDs Layer Transfer and Integration

Figure 3. 2 is the experimental demonstration of the water-assisted 2D TMD layer transfer and integration utilizing 2D molybdenum disulfide (2D MoS₂) as a representative case. Figure 3.2a shows the representative images of as-grown 2D MoS₂ layers on SiO₂/Si on a dimension of $\sim 2 \times 3 \text{ cm}^2$ (top image). In optimizing 2D MoS₂ layers growth conditions, we have considered the previous studies which report the transition of horizontal-to-vertical 2D layer orientation in the CVD thermal sulfurization of Mo.[9–11] In order to ensure the growth of horizontally-oriented layers only, we have typically deposited Mo of small and uniform thickness (<3 nm) and carried out the CVD sulfurization using the previously developed recipe.[12–14] The cross-sectional transmission electron microscope (TEM) characterization (bottom image) of the same sample represents well resolved, all horizontally-oriented 2D MoS₂ layers. Figure 3. 2b shows the Raman spectroscopy characterization of the same sample, revealing two distinguishable peaks corresponding to their in-plane and out-of-plane E_{12g}¹ and A_{1g} oscillation modes.[15, 16] Figure 3. 2c shows the time-lapsed representative images to demonstrate the sequential delamination of 2D MoS₂ layers inside water recorded for ~ 4 sec. As shown in the images, 2D MoS₂ layers become spontaneously separated from the underlying SiO₂/Si substrate and subsequently float on the water surface maintaining their original size and shape. The success of this facile water-assisted delamination of 2D layers is attributed to the surface energy imbalance between 2D MoS₂ basal planes and SiO₂ surfaces, as depicted in Figure 3. 2d. Upon exposure to water droplet, our

CVD-grown 2D MoS₂ layers exhibit significantly larger hydrophobicity compared to the underlying SiO₂, as demonstrated by the water contact angle measurement results. The observation is consistent with the previous studies on the surface wettability of 2D MoS₂ layers exposing their basal planes for water adsorption.[17–19] Accordingly, upon the onset of water penetration into any opened interfaces of 2D MoS₂/SiO₂, mechanical tension is to occur and propagate underneath the weakly vdW-bound 2D basal planes. In other words, the distinct surface wettability of 2D MoS₂ vs. SiO₂ indicates a strong tendency for water repulsion from 2D MoS₂ vs. water attraction to SiO₂, respectively.[6, 20, 21] Moreover, it has been well known that the surface energy of 2D MoS₂ layers is also sensitive to air exposure and its duration period. 2D MoS₂ layers exhibit more pronounced hydrophobicity after elongated air exposure, confirmed by the water contact angle measurements in various studies.[19, 22, 23] In fact, we note that our CVD-grown 2D MoS₂ layers also tend to become more easily separable inside water once they were exposed in air for a few days after growth. Such enhanced hydrophobicity in slightly aged 2D MoS₂ layers has been attributed to a few factors, e.g., accumulation of hydrocarbons on their surface obtained from ambient air.[22, 24] More detailed discussion regarding the influence of the surface properties of 2D MoS₂ layers on the efficacy of water-assisted spontaneous layer separation is presented in the next section.

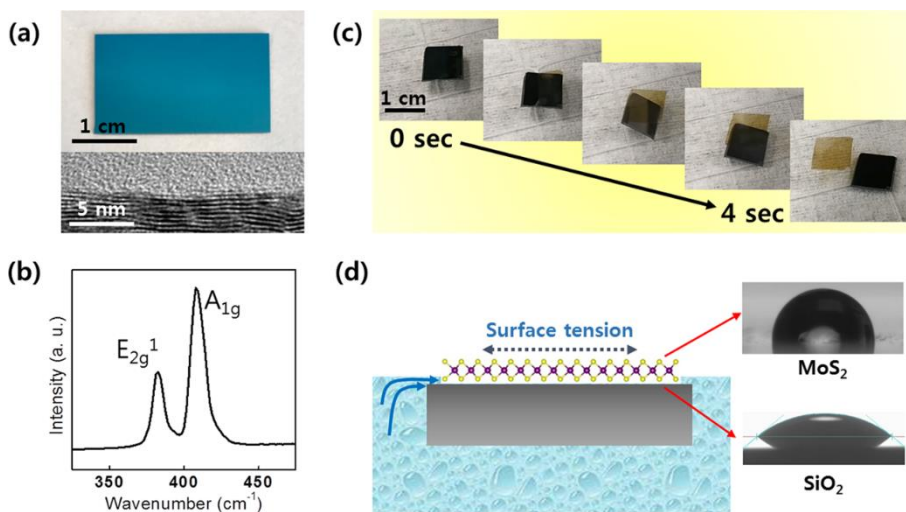


Figure 3. 2. (a) Image of 2D MoS₂ layers as-grown on SiO₂/Si and the corresponding cross-sectional HRTEM image. (b) Raman spectrum obtained from the 2D MoS₂ layers denoting their characteristic peaks. (c) Time-lapsed snapshot images to demonstrate the water-assisted spontaneous separation of 2D MoS₂ layers inside water. (d) Illustration of the water penetration process at the 2D MoS₂/SiO₂ interface along with the representative images of water contact angle measurements for 2D MoS₂ layers and SiO₂.

3.1.3.3. Principle of Water-assisted 2D TMDs Layer Separation

Lastly, we discuss about the fundamental principle behind the facile delamination of 2D layers inside water. We identify followings as two major factors; i.e., crystallographic layer orientation and surface wetting property of 2D MoS₂ layers.

Influence of 2D layer orientation: We have observed that the spontaneous delamination of 2D layers inside water happens with 2D TMDs obtained from the sulfurization of thin metal seeds (typically <3 nm). 2D TMDs obtained in this manner exhibit horizontally-aligned basal planes of well-resolved layers; for example, horizontally-aligned 2D MoS₂ layers of ~7–8 nm thickness obtained from the sulfurization of ~2.5 nm thick Mo have been confirmed by atomic force microscopy (AFM) and cross-sectional TEM characterization. Maintaining the small thickness of metal seeds is critically important to ensure that 2D TMD layers grow in horizontal orientation as identified in our previous studies.[11, 13]. In this case, weak molecular vdW attraction will be responsible for holding the 2D basal planes of diminished defect density to the SiO₂ substrate surface, enabling facile water penetration in between them. Meanwhile, we have identified that the CVD sulfurization of thick (typically ~6–7 nm) metal seeds tends to grow 2D TMD layers in vertical alignment. Figure 3. 3a, b presents the plane-view and cross-sectional HRTEM images of vertically-aligned 2D MoS₂ layers prepared with the CVD sulfurization of ~7 nm thick Mo. It is noted that their 2D edge sites are predominantly exposed on the top surface (Figure 3. 3a) while 2D layers are vertically “rooted” in the SiO₂ growth substrate (Figure 3. 3b). This morphology is in sharp contrast to that of

horizontally-aligned layers (Figure 3. 3c) and is believed to result from the actual chemical bonding of 2D MoS₂ edges and SiO₂ instead of weak vdW attraction. Accordingly, it has been identified that the water-assisted spontaneous separation of vertically-aligned 2D layers is much more difficult in terms of retaining their original shape and dimension on a large area. We have previously identified that 2D TMDs tend to rearrange their layer orientation with increasing physical confinement (increasing metal thickness) in a way to release the accumulating in-plane strain exerted by interconnecting 2D layers.[11] Moreover, we considered the theoretical condition to satisfy the water-assisted spontaneous separation of 2D layers by considering its associated surface energy contributions. The work of adhesion, W , required for the spontaneous 2D layer separation is expressed as $W = \gamma_{sw} + \gamma_{wl} - \gamma_{sl}$, where γ_{sw} , γ_{wl} , and γ_{sl} are interfacial tension between substrate and water, water and 2D layer, substrate and 2D layer, respectively. In comparing the 2D MoS₂ layers of horizontal vs. vertical orientation, we note that vertically-aligned 2D MoS₂ layers exhibit significantly higher adhesion energy with respect to the SiO₂ surface owing to the exposure of energetically reactive 2D edge sites; i.e., order-of-magnitude higher binding energy of 2D edges with dangling bonds over 2D basal planes with saturated bonds.[25, 26] Accordingly, the value of γ_{sl} for vertically-aligned 2D MoS₂ layers should be much smaller than that for horizontally-aligned ones, which further justifies the observed difficulty with their spontaneous separation inside water. Meanwhile, water can easily penetrate into the vdW gaps exposed in between horizontally aligned 2D MoS₂ layers assisted by their large γ_{sl} values. Specific values for these interfacial

energy terms are currently unavailable in literature, which makes more precise quantification and elucidation difficult at present.

Influence of surface wetting property: As above mentioned, we have observed that 2D MoS₂ layers aged for a few days after their growth typically exhibit better performance in terms of spontaneous layer separation inside water. In fact, it has been known that the water-wettability of 2D MoS₂ layers increases with elongated air exposure owing to the lowered surface energy,[22, 45] similar to the observation with graphene.[27, 28]. Accordingly, the surface of 2D MoS₂ layers becomes more hydrophobic reflected by increasing water contact angle values, which becomes another determining factor for the water-assisted 2D layer separation. The separation efficacy of hydrophobic thin layers inside water has been recently studied,[29] which confirms a presence of strong capillary-induced “peeling” force exerted at their edges interfaced with water. A smaller amount of the capillary force is required to separate the thin layers of higher hydrophobicity while hydrophilic layers tend to get submerged inside water rather than being peeled off.[29] We believe that the identical principle should apply to the water-assisted spontaneous separation of 2D layers presented in this study. Indeed, we have observed that our as-grown 2D MoS₂ layers of diminished hydrophobicity immersed into water immediately following their growth tend to get submerged without yielding the desired layer separation. This behavior is in sharp contrast to the facile and spontaneous layer separation typically observed with slightly-aged 2D MoS₂ layers (Figure 3. 4).

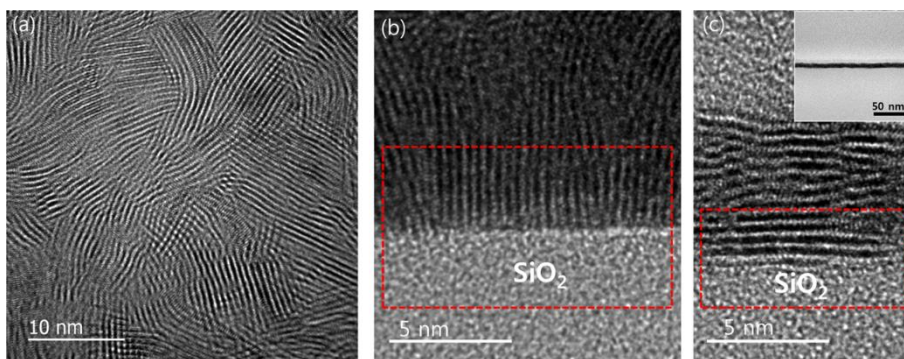


Figure 3.3. (a) Plane-view and (b) cross-sectional HRTEM images of vertically-aligned 2D MoS₂ layers grown on SiO₂. 2D MoS₂ layers are rooted in the SiO₂ surface (red highlight in (b)). (c) Cross-sectional HRTEM image of horizontally-aligned 2D MoS₂ layers grown on SiO₂. 2D basal planes are in contact with the SiO₂ surface. The inset shows a low magnification TEM image of the corresponding sample.

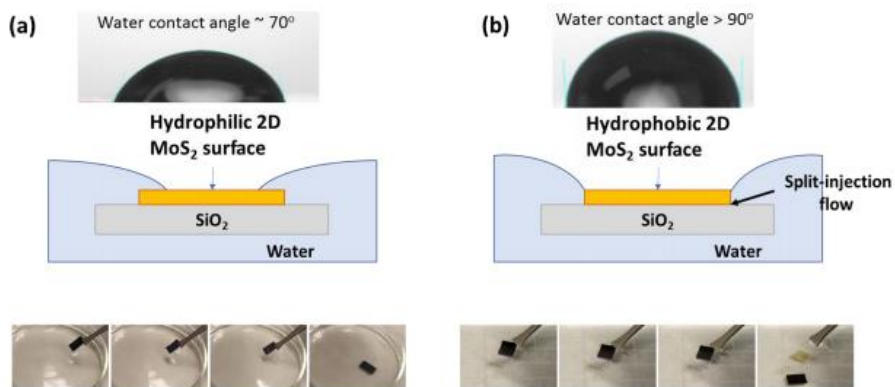


Figure 3. 4. Distinguishable characteristics of 2D MoS₂ layers on SiO₂ substrates upon water immersion when they are in two different surface states. (a) Pristine samples typically get submerged in water. (b) Aged samples yield the facile and spontaneous separation of 2D layers.

3.1.4. Conclusion

In summary, we report a novel approach to reliably transfer a variety of 2D TMD layers and heterogeneously integrate them onto virtually arbitrary yet unconventional substrates. The presented method benefits from the water-assisted spontaneous separation of 2D layers, exhibiting distinguishable advantages over conventional approaches in terms of property preservation and size scalability. The intrinsic generality and versatility of this integration method has been verified with 2D TMDs of various kinds as well as their multi-component heterostructures. Moreover, its potential for device applications has been confirmed by demonstrating centimeter-scale 2D MoS₂-based flexible photodetectors and pressure sensors integrated on exotic substrates, which are difficult to fabricate with any other conventional approaches.

3.1.5. Reference

- (1) Pant, A., et al. Fundamentals of lateral and vertical heterojunctions of atomically thin materials. *Nanoscale* 8, 3870 (2016).
- (2) Li, M.-Y., Chen, C.-H., Shi, Y. & Li, L.-J. Heterostructures based on two-dimensional layered materials and their potential applications. *Mater. Today* 19, 322–335 (2016).
- (3) Das, S., et al. Beyond graphene: progress in novel two-dimensional materials and van der Waals solids. *Annu. Rev. Mater. Res.* 45, 1–27 (2015).
- (4) Geim, A. K. & Grigorieva, I. V. Van der Waals heterostructures. *Nature* 499, 419 (2013).
- (5) Kang, J., et al. Band offsets and heterostructures of two-dimensional semiconductors. *Appl. Phys. Lett.* 102, 012111 (2013).

- (6) Gurarslan, A., et al. Surface energy-assisted perfect transfer of centimeter-scale monolayer and few-layer MoS₂ films onto arbitrary substrates. *ACS Nano* 8, 11522–11528 (2014).
- (7) Lin, Y.-C., et al. Wafer-scale MoS₂ thin layers prepared by MoO₃ sulfurization. *Nanoscale* 4, 6637–6641 (2012).
- (8) Liu, K.-K., et al. Growth of large-area and highly crystalline MoS₂ thin layers on insulating substrates. *Nano Lett.* 12, 1538–1544 (2012).
- (9) Jung, Y. et al. Metal seed layer thickness-induced transition from vertical to horizontal growth of MoS₂ and WS₂. *Nano Lett.* 14, 6842–6849 (2014).
- (10) Kong, D. et al. Synthesis of MoS₂ and MoSe₂ films with vertically aligned layers. *Nano Lett.* 13, 1341–1347 (2013).
- (11) Choudhary, N. et al. Strain-driven and layer number-dependent crossover of growth mode in van der Waals heterostructures: 2D/2D layer-by-layer horizontal epitaxy to 2D/3D vertical reorientation. *Adv. Mater. Interfaces* 5, 1800382 (2018).
- (12) Choudhary, N. et al. Centimeter scale patterned growth of vertically stacked few layer only 2D MoS₂/WS₂ van der Waals heterostructure. *Sci. Rep.* 6, 25456 (2016).
- (13) Islam, M. A. et al. Noble metal-coated MoS₂ nanofilms with vertically-aligned 2D layers for visible light-driven photocatalytic degradation of emerging water contaminants. *Sci. Rep.* 7, 14944 (2017).
- (14) Jung, Y., et al. Chemically synthesized heterostructures of two-dimensional molybdenum/tungsten-based dichalcogenides with vertically aligned layers. *ACS Nano* 8, 9550–9557 (2014).
- (15) Li, H., et al. From bulk to monolayer MoS₂: evolution of Raman scattering. *Adv. Funct. Mater.* 22, 1385–1390 (2012).

- (16) Verble, J. L., Wietling, T. J. & Reed, P. R. Rigid-layer lattice vibrations and van der Waals bonding in hexagonal MoS₂. *Solid State Commun.* 11, 941–944 (1972).
- (17) Gaur, A. P. S. et al. Surface energy engineering for tunable wettability through controlled synthesis of MoS₂. *Nano Lett.* 14, 4314–4321 (2014).
- (18) Choi, J. et al. Hierarchical, dual-scale structures of atomically thin MoS₂ for tunable wetting. *Nano Lett.* 17, 1756–1761 (2017).
- (19) Chow, P. K. et al. Wetting of mono and few-layered WS₂ and MoS₂ films supported on Si/SiO₂ substrates. *ACS Nano* 9, 3023–3031 (2015).
- (20) Lai, S., et al. Water-penetration-assisted mechanical transfer of large-scale molybdenum disulfide onto arbitrary substrates. *RSC Adv.* 6, 57497–57501 (2016).
- (21) Islam, M. A., et al. Centimeter-scale 2D van der Waals vertical heterostructures integrated on deformable substrates enabled by gold sacrificial layer-assisted growth. *Nano Lett.* 17, 6157–6165 (2017).
- (22) Kozbial, A., Gong, X., Liu, H. & Li, L. Understanding the intrinsic water wettability of molybdenum disulfide (MoS₂). *Langmuir* 31, 8429–8435 (2015).
- (23) Annamalai, M. et al. Surface energy and wettability of van der Waals structures. *Nanoscale* 8, 5764–5770 (2016).
- (24) Gao., et al. Aging of transition metal dichalcogenide monolayers. *ACS Nano* 10, 2628–2635 (2016).
- (25) Cho, S.-Y., et al. Highly Enhanced Gas Adsorption Properties in Vertically Aligned MoS₂ Layers. *ACS Nano*, 2015 9, 9314–9321 (2015).
- (26) Islam, M. A., et al. Three dimensionally-ordered 2D MoS₂ vertical layers integrated on flexible substrates with stretch-tunable functionality and improved sensing capability. *Nanoscale* 10, 17525–17533 (2018).

(27) Kozbial, A. et al. Study on the Surface Energy of Graphene by Contact Angle Measurements. *Langmuir* 30, 8598–8606 (2014).

(28) Li, Z. et al. Effect of airborne contaminants on the wettability of supported graphene and graphite. *Nature Materials* 12, 925–931 (2013).

(29) Khodaparast, S., Boulogne, F., Poulard, C. & Stone, H. A. Water-Based Peeling of Thin Hydrophobic Films. *Phys. Rev. Lett.* 119,154502 (2017).

3.2. Water Dissoluble Salt Substrates for 2D TMDs Layer

The contents of this section have been published in: Sang Sub Han, Tae-Jun Ko, Changhyeon Yoo, Mashiyat Sumaiya Shawkat, Hao Li, Bo Kyung Kim, Woong-Ki Hong, Tae-Sung Bae, Hee-Suk Chung, Kyu Hwan Oh, and Yeonwoong Jung “Automated Assembly of Wafer-Scale 2D TMD Heterostructures of Arbitrary Layer Orientation and Stacking Sequence Using Water Dissoluble Salt Substrates” Nano Lett. 20, 3925–3934 (2020).

3.2.1. Introduction

2D TMDs layers offer distinct advantages due to their extremely large mechanical tolerance and small thickness as well as vdW attraction-enabled relaxed assembly requirement.[1–3] Such unparalleled opportunities have triggered proliferating extensive research endeavors as well as piloting industry-oriented initiatives toward emergent technologies.[4–15] While major efforts in fundamental sciences have focused on unveiling their intrinsic properties,[16–19] rapidly growing intellectual property landscapes have already started to leverage them toward practical device applications in a wide range of domains.[4, 5, 20, 21] To this end, it is important to manufacture 2D TMD layers of controlled chemistry and morphology in a way to be compatible with the currently available wafer process schemes. Ultimately, there is demand to develop an “automation” process that will enable the deterministic integration of wafer-scale 2D TMD layers onto target substrates in a controlled and sustainable manner. This approach not only relieves the laborious and delicate handling of individual 2D layers, but this approach also should preserve their intrinsic material properties, minimizing the involvement of quality-impairing chemicals during the integration stages.[5, 22–24] Such perspective is particularly essential for realizing 2D TMD heterolayers which

require the individual 2D layers of chemically distinct components to be integrated in a layer-by-layer manner.[4, 15, 20, 25–29] Moreover, the integration process should be generic to integrating 2D TMDs irrespective of their crystallographic layer orientation, that is, horizontally or vertically aligned onto substrates of virtually unrestricted forms.

In this study, we developed a versatile and sustainable approach to manufacture wafer-scale 2D TMD layers of arbitrary chemical composition and crystallographic orientation on exotic substrates. This manufacturing scheme adopts the scalable chemical vapor deposition (CVD) growth of 2D TMD layers on “water-dissoluble” salt wafers and their spontaneous delamination. We demonstrated the controlled integration of “vertically-aligned” 2D heterolayers of whichever desired layer-stacking orders in a fully automated manner and projected their opportunities for unconventional device applications.

3.2.2. Experimental Section

3.2.2.1. Growth of 2D TMD Layers

CVD was performed for the sulfurization, selenization, and tellurization of pre-deposited metals using a horizontal quartz tube furnace (Lindberg/Blue M Mini-Mite). Metal films of various thicknesses were deposited on single-crystalline salt substrates (TedPella, 99% single crystal) by an electron beam evaporator (Temescal) at a deposition rate of 0.1 \AA/s , that is, 0.7 nm Pt for HA-2D PtSe₂ layers, 1.5 nm Pt for HA-2D PtTe₂ layers, and 6 nm Pt and Mo for VA-2D PtSe₂, VA-2D PtTe₂, and VA-2D MoS₂. The metal-deposited salt

crystals were placed in the center zone of the CVD furnace. Alumina boats containing chalcogenide powders specific to targeted 2D TMD layers were placed in the upstream side of the furnace, that is, Se and Te for PtSe₂ and PtTe₂, respectively, and S for MoS₂. All the chalcogen powders were high purity (~99.9%) and were purchased from Millipore-Sigma. The quartz tube was pumped down to a base pressure of ~20 mTorr and purged with Ar gas for ~10 min to remove organic residuals in it. Subsequently, it was heated to the reaction temperature specific to target materials, that is, 400 °C for 2D PtSe₂ and 2D PtTe₂ layers and 550 °C for MoS₂. The total ramping time was 50 min, and the reaction was maintained at the target temperature for another 50 min. Throughout the reaction, Ar gas was supplied at a constant rate of 100 standard cubic centimeters per minute, and the furnace was naturally cooled down to room temperature once the reaction was over. Prior to the metal deposition, as-purchased salt crystals can be optionally polished with polishing papers (purchased from Micro-Surface) without applying liquid if their surface smoothness needs to be improved; initial rough polishing was with 4000 grit and final fine polishing was with 12000 grit.

3.2.2.2. Delamination and Integration of 2D TMD Layers

For the manual transfer of 2D TMD layers, as-prepared samples are immersed in DI water until their complete delamination. The delaminated 2D layers floating on the water surface are maintained at 70 °C, followed by a subsequent transfer to fresh DI water to remove any residual salt elements. The 2D TMDs layers integrated on secondary substrates are dried on a hot plate at 70 °C for ~12 h to remove residual water. For the demonstration of the water-

assisted automated integration of 2D TMD layers, we fabricated the setup and the loading rod presented in Figure 3. 20b using a 3D printer (PRUSA i3MK3). The loading rod was manually connected to a home-built tensile stretcher, which moves it between the sample stage and the integration stage in an automated manner.

3.2.2.3. Structural and Chemical Characterization

TEM characterization was performed using JEOL ARM 200F Cs-corrected TEM and FEI F30 TEM at an accelerating voltage of 200 and 300 kV, respectively. Raman characterization was using Renishaw RM 1000B system with a laser source of 514 nm wavelength. XPS characterization was performed using ESCALAB 250 with an Al K α -ray source (1486.3 eV) in ultrahigh vacuum condition (10^{-9} mBar).

3.2.3. Results and Discussion

3.2.3.1. The Manufacturing Process of the Water-assisted

Delamination from Water Soluble Salt Substrates

The manufacturing process relies on the water-assisted delamination of CVD-grown wafer-scale 2D TMD layers. Figure 3. 5a, b describes the working principle for 2D TMD layers of distinct layer orientation, that is, horizontally aligned (HA) versus vertically aligned (VA), respectively. It is known that HA-2D TMD layers can be spontaneously delaminated from their growth wafers (e.g., silicon dioxide/silicon (SiO_2/Si)) inside water[30–36] and attributed to the exposure of vdW gaps in between them and the wafers. Figure 3. 5a illustrates this scenario along with a representative cross-sectional high-

resolution transmission electron microscopy (HRTEM) image of HA-2D molybdenum disulfide (MoS_2) layers. However, delaminating VA-2D TMD layers has been technically challenging with this approach, as described in Figure 3. 5b. In this case, individual 2D layers are vertically “rooted” in the wafer surface without exposing vdW gaps, impeding their delamination in water as previously verified.[30] This challenge has been the major limiting factor in terms of fully exploring technological opportunities of VA 2D-TMD layers beyond their growth substrate-bound forms. In general, VA 2D-TMD layers exhibit unparalleled chemical reactivity and physisorption properties owing to their surface-exposed rich dangling bonds, suggesting great implications for high-performance electrochemical and/or molecular sensing applications.[37, 38] Such unprecedented opportunities can be realized even in flexible and/or stretchable forms as far as they are deterministically and stably integrated on mechanically reconfigurable yet functional substrates retaining their original structural integrity. Figure 3. 5c illustrates schematics of our manufacturing strategy, which overcomes this limitation and can be generalized to 2D TMD layers of any layer orientation. Metal thin films are deposited on single-crystalline salt substrates, and the prepared samples undergo CVD processes adopting the previously developed recipes.[30, 32, 39–42] The 2D layer orientation can be controlled by adjusting the thickness of the metal films,[42, 43] and we focus on growing and delaminating VA-2D layers. As-prepared samples are immersed in water, which causes the spontaneous delamination of only VA-2D layers only within a few seconds after the immersion. The original salt substrates remain nearly intact and can be reused

for subsequent CVD growth. The delaminated VA-2D TMD layers floating on the water surface are manually integrated on secondary substrates of desired functionalities, and this entire process can be repeated until targeted 2D TMD heterolayers are achieved. In order to verify the generality and versatility of this approach, we grew a variety of 2D TMD layers including platinum diselenide (PtSe_2) and platinum ditelluride (PtTe_2) beyond MoS_2 on a variety of salt crystals including sodium chloride (NaCl), potassium chloride (KCl), and potassium bromide (KBr). These substrates have been judiciously selected due to their combined advantage of high melting temperature (up to ~ 800 °C) and high water solubility.[44] Details for CVD growth conditions are described in the *Experimental Section*. Figure 3. 5d shows photographs corresponding to the step-by-step procedures illustrated in Figure 3. 5c. Accordingly, they can be recycled for subsequent CVD growths, typically up to 20 times, offering high sustainability. Also, we emphasize that the entire process is conducted in water without involving any other chemical etchants or polymeric adhesives, thus it is intrinsically free of any chemical-driven properties degradation.

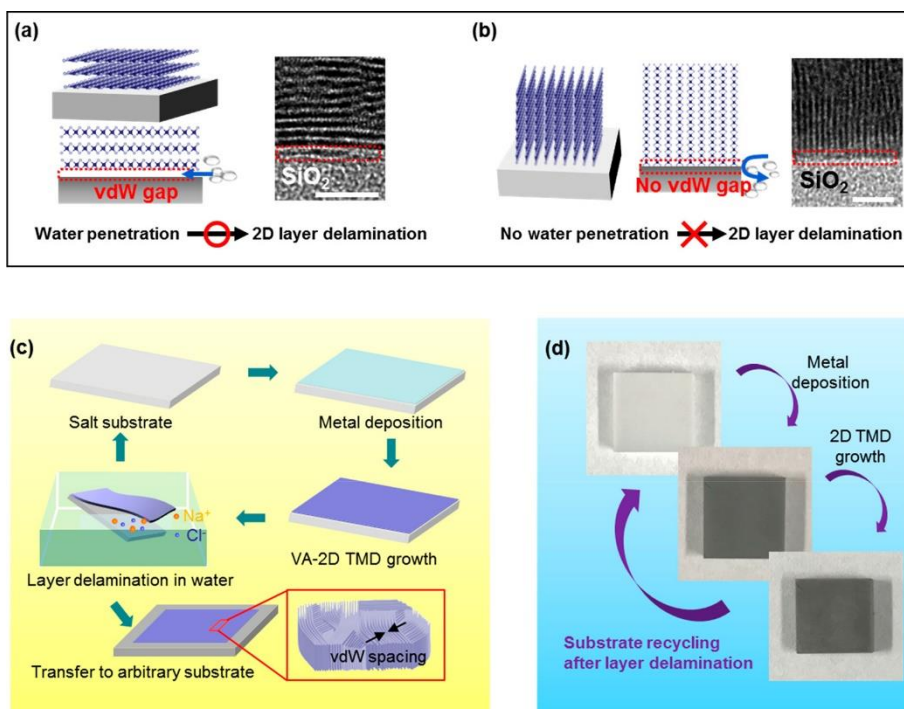


Figure 3. 5. (a,b) Schematic illustrations highlighting the feasibility of water-assisted delamination for (a) HA- and (b) VA-2D TMD layers, and their representative cross-sectional HRTEM images of 2D MoS₂ layers. The scale bars are 5 and 2.5 nm for (a,b), respectively. (c) Schematic illustration of stepwise processes for the water-assisted delamination and transfer of VA-2D TMD layers using salt crystals. (d) Representative images to highlight the sustainability of salt crystals throughout sequential steps of metal deposition, 2D TMD layers growth, and their delamination.

3.2.3.2. Structural and Chemical Analysis of 2D TMDs Layer grown on Salt Substrates

Figure 3. 6 demonstrates the successful CVD growth and delamination of VA-2D MoS₂ layers using NaCl substrates, which were obtained by the growth recipe developed for SiO₂/Si substrates in our lab.[25, 39, 43] Figure 3. 6a presents photographs of a sample taken at each preparation stage and Figure 3. 6b depicts time-lapsed snapshot images of the corresponding 2D layers undergoing water-assisted delamination. The delamination is completed instantly after water immersion (typically within a few seconds). After this step, the delaminated 2D layers can be transferred to freshwater to ensure the complete removal of any salt ion residuals (details are described in the *Experimental Method*). Figure 3. 6c shows a low-magnification TEM image of the sample prepared in Figure 3. 6a, b, evidencing its highly continuous film morphology without any disconnection or cracks. Figure 3. 6d presents the corresponding selected area electron diffraction (SAED) characterization which exhibits the indexed (002) and (004) ring patterns of hexagonal MoS₂ crystals, consistent with previous observations with VA- 2D MoS₂ layers.[43, 45] The HRTEM image in Figure 3. 6e evidences that the sample is entirely composed of VA-2D MoS₂ layers, predominantly exposing their edge sites on the surface. The measured interlayer spacing is ~0.65 nm which precisely matches the (001) planar distance (that is, c-axis) of hexagonal MoS₂ crystals.[43, 45–47] The inset in Figure 3. 6e shows the digital micrograph intensity profile corresponding to the line-scan orientation (white arrow) in the image, confirming the uniform dimension of vdW gaps. The chemical

composition of the VA-2D MoS₂ layers was characterized by energy dispersive X-ray spectroscopy (EDS). Figure 3. 6f shows EDS profiles obtained from the same sample confirming the stoichiometric ratio of Mo/S = 1:2, which is highly consistent with previous studies.[30, 48] It is remarkable to note that the EDS intensity of salt residuals is negligible, as presented in the zoomed-in image in the right panel. The chemical integrity of the sample was further characterized by X-ray photoelectron spectroscopy (XPS). Figure 3. 6g displays XPS core-level spectra of Mo 3d, S 2p, Na 1s, and Cl 2p binding energies obtained from the same sample. The XPS spectra of Mo 3d and S 2p reveal deconvolution peaks at the specific binding energies consistent with previous studies on 2D MoS₂ layers,[39, 49, 50] consistent with the SAED and EDS characterization. Meanwhile, the XPS spectra of Na 1s and Cl 2p exhibit negligible peaks, further confirming the chemically clean nature of this layer delamination approach. We note that as-delaminated 2D MoS₂ layers can exhibit a very small amount of Na⁺ residuals, which can be completely removed by the additional water rinsing step described in the *Experimental Method* section. Figure 3. 6h presents Raman spectroscopy characterization which reveals two distinguishable peaks of in-plane E_{2g}¹ and out-of-plane A_{1g} oscillation modes of 2D MoS₂ layers. It is noted that the intensity of the A_{1g} peak is significantly higher than that of the E_{2g}¹ peak, which is a distinct feature of VA-2D MoS₂ layers and is fully consistent with previous studies.[39, 43, 51, 52]

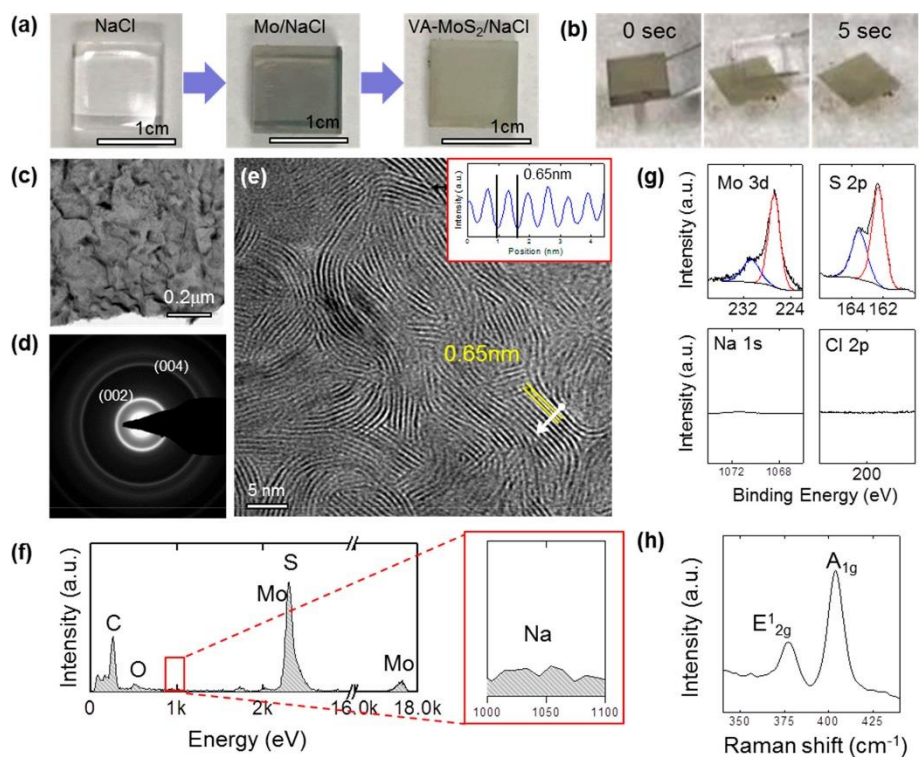


Figure 3. 6. (a) HRTEM image of VA-2D PtSe₂ layers delaminated from a NaCl substrate. The inset is the corresponding SAED pattern with indexed PtSe₂ crystalline planes. (b) Raman spectrum, (c) XPS spectra, and (d) EDS profile obtained from the same sample of delaminated VA-2D PtSe₂ layers. (e) HRTEM image of HA-2D PtSe₂ layers delaminated from a NaCl substrate. The inset is the corresponding low-magnification TEM image. (f) SAED pattern corresponding to the sample in (e). (g) EELS elemental map images obtained from the same sample.

3.2.3.3. The Diversity of Salt Substrates for 2D TMDs Growth and Delamination

In order to verify the generality of this growth/delamination approach, we grew a variety of 2D TMD layers on diverse salt crystal substrates and delaminated them. Figure 3. 7a–d demonstrates the CVD growth of VA-2D PtSe₂ layers on NaCl crystals and their water-assisted delamination. Figure 3. 7a shows a representative HRTEM image of VA-2D PtSe₂ layers and their corresponding indexed SAED pattern (inset). Figure 3. 7b presents a Raman spectroscopy profile of the same sample after delamination, revealing the E_{12g}¹ and A_{1g} peaks of PtSe₂. Figure 3. 7c exhibits XPS spectral profiles of Pt 4f, Se 3d, Na 1s, and Cl 2p core levels, which confirm the stoichiometric atomic ratio of PtSe₂. [40, 53] Meanwhile, the spectral profiles of Na 1s and Cl 2p core levels do not exhibit any noticeable peaks, similar to the observation with 2D MoS₂ layers obtained from NaCl substrates. Figure 3. 7d shows the corresponding EDS profile, which further confirms the stoichiometric ratio of Pt/Se = 1:2 with a negligible presence of Na atoms. We further extended this water-assisted growth and delamination approach to other materials, including VA-2D PtTe₂ layers and single-crystalline KCl substrates. The delaminated 2D layers preserve the original stoichiometry of their as-grown state. Additionally, the growth and delamination of VA-2D PtSe₂ layers using KCl and KBr substrates were confirmed. The intrinsic vdW gap spacings of the VA-2D TMD layers are much smaller than the dimensions of the salts ions in their hydrated states [54] which possibly explains the negligible presence of the ions in the delaminated 2D layers. In addition to VA-2D TMD layers, HA-2D TMD layers were also

grown and delaminated using salt crystals. Figure 3. 7e–g presents a representative example of HA-2D PtSe₂ layers obtained from NaCl substrates. Figure 3. 7e shows an HRTEM image of HA-2D PtSe₂ layers revealing the lattice fringes from their basal planes along with the corresponding low-magnification TEM image (inset). Figure 3. 7f presents the corresponding SAED characterization obtained from a large area (>10 μm²) of the sample exhibiting the dominant appearance of (110) diffraction ring pattern, clearly distinct from the characteristic observed with VA-2D PtSe₂ layers (Figure 3. 7a inset). This observation indicates that a large number of (110) crystalline planes are orthogonally aligned with respect to the TEM beam direction, confirming that the basal planes of 2D PtSe₂ layers are horizontally aligned consistent with previous studies.[40, 42] Figure 3. 7g shows TEM electron energy loss spectroscopy (EELS) maps of the corresponding sample, revealing a highly uniform spatial distribution of constituent elements. Additional characterization results further verify the crystalline structure and stoichiometric composition of the delaminated HA-2D PtSe₂ layers.

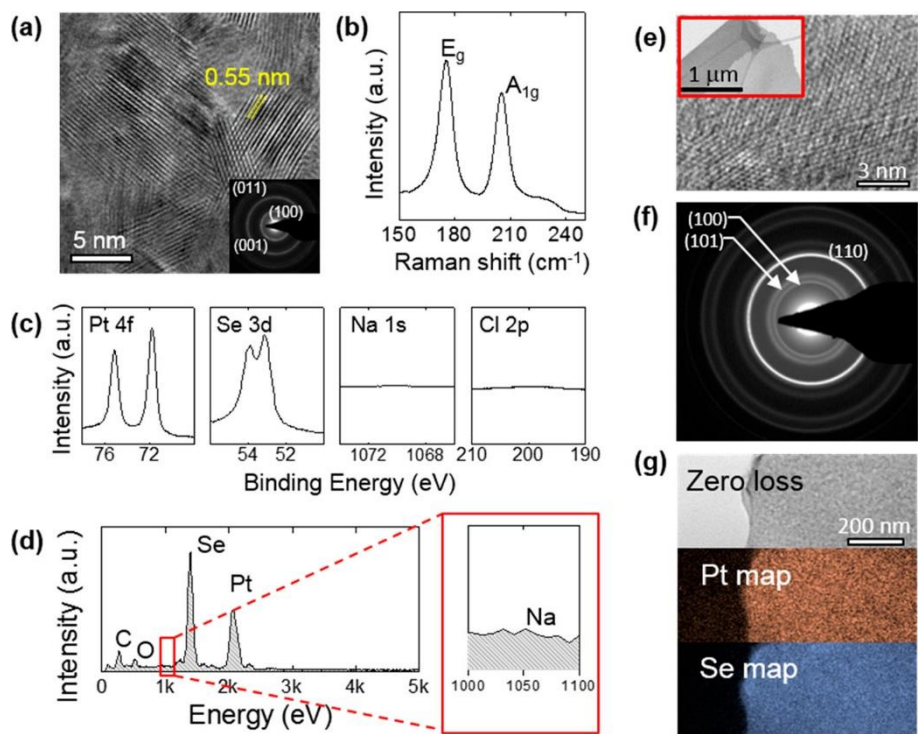


Figure 3. 7. (a) HRTEM image of VA-2D PtSe₂ layers delaminated from a NaCl substrate. The inset is the corresponding SAED pattern with indexed PtSe₂ crystalline planes. (b) Raman spectrum, (c) XPS spectra, and (d) EDS profile obtained from the same sample of delaminated VA-2D PtSe₂ layers. (e) HRTEM image of HA-2D PtSe₂ layers delaminated from a NaCl substrate. The inset is the corresponding low-magnification TEM image. (f) SAED pattern corresponding to the sample in (e). (g) EELS elemental map images obtained from the same sample.

3.2.3.4. The Heterogeneous Integration of Multiple 2D TMDs Layers

We then demonstrated the heterogeneous integration of multiple VA-2D TMD layers on unconventional substrates, achieving 2D/2D heterolayers. To this end, we developed a home-built stage which enables the layer-by-layer delamination and integration of various 2D TMD layers in an “automated” manner. Figure 3. 8a shows a schematic illustration of the apparatus describing its working principle. It is composed of three major components; (1) loading stage where as-grown 2D TMD/salt substrate samples are loaded, (2) water chamber which supplies a controlled amount of water to the loading stage, and (3) integration stage where delaminated 2D TMD layers are individually stacked up. Figure 3. 8b shows a top-to-bottom view of the home-built apparatus specifying the loading stage (blue box) containing a sample of VA-2D PtTe₂/NaCl substrate and the integration stage (green box). The blue arrow presents the flow of water into the sample stage and the yellow arrow denotes the movement of the loading rod, both of which are executed in a fully automated manner. Figure 3. 8c specifies the 2D layer integration event occurring in the red dotted box in Figure 3. 8b in a time-lapsed manner. Once the VA-2D PtTe₂ layers are delaminated within the blue-boxed sample stage (left panel), they are subsequently transferred to the integration stage by the loading rod (middle panel). Eventually, they become integrated onto the preloaded target substrate within the green boxed stage and the loading rod returns to the starting point for the next processes (right panel). Mild heating can be optionally applied to the integration stage to promote the evaporation of the supplied water to ensure the robust integration of each sample. We

demonstrated the integration of wafer-scale 2D TMD heterolayers employing various components of controlled orientation. Figure 3. 8d shows representative images demonstrating the sequential integration of three different VA-2D TMD layers, that is, MoS₂, PtSe₂, and PtTe₂, on top of a polyethylene terephthalate (PET) substrate (purchased from Eg-eMigoo). The lateral dimension of each material is greater than a few square centimeters, and the PtSe₂ and PtTe₂ layers were intentionally grown to be in rectangular shapes for better visualization. Figure 3. 8e presents another example of large-area PtTe₂/PtSe₂/MoS₂ heterolayers integrated on a mechanically bendable substrate maintaining their vertical alignment. We also demonstrated other heterolayers stacked in a different order, that is, PtSe₂/MoS₂/PtTe₂, confirming the high controllability of layer stacking order. The chemical integrity of these large-area 2D heterolayers was characterized by Raman spectroscopy, as shown in Figure 3. 8f. The image on the top panel shows a Raman spectrum obtained from a stacked region of PtTe₂/MoS₂. The PtTe₂ and MoS₂ Raman spectra presented on the bottom panel correspond to the enlarged views of the blue and red boxed regions on the top panel, respectively. The PtSe₂ Raman spectrum on the bottom panel was separately obtained from a region containing only 2D PtSe₂ layers.

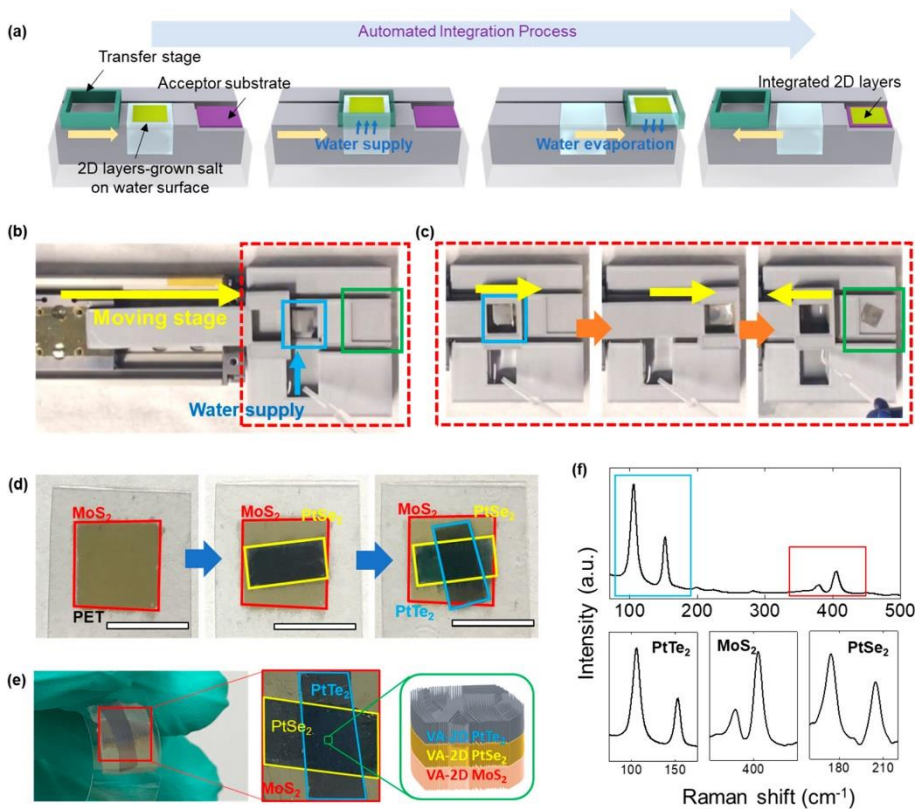


Figure 3. 8. (a) Schematic illustration and working principle for the water-assisted automated integration of 2D TMD layers. (b) Top-to-bottom view of a home-built 2D layer integration stage describing its major components. (c) Time-lapsed snapshot images sequentially depicting the water-assisted automated integration of VA-2D PtTe₂ layers. (d) Heterogeneous integration of three-different VA-2D TMD layers on a PET substrate. The scale bar is 1 cm. (e) Mechanical flexibility of VA-2D TMD heterolayers. The sample is different from that in (d). (f) Raman spectral profiles obtained from a sample of 2D heterolayers composed of PtTe₂, MoS₂, and PtSe₂.

3.2.4. Conclusion

We report a new method to heterogeneously integrate wafer-scale 2D TMD layers onto secondary substrates in a highly scalable and controllable manner. We employed salt crystals as growth substrates, which enable water-assisted delamination of as-grown 2D TMD layers irrespective of their compositions and orientations. We demonstrated a fully automated assembly of wafer-scale 2D TMD layers on unconventional substrates difficult with other approaches. These wafer-scale 2D TMD heterolayers retaining their intrinsic material properties enable a variety of near atom-thickness device building blocks of diverse form factors.

3.2.5. Reference

- (1) Tan, C., et. al. Recent Advances in Ultrathin Two-Dimensional Nanomaterials. *Chem. Rev.* 2017, 117 (9), 6225–6331.
- (2) Zhang, H. Ultrathin Two-Dimensional Nanomaterials. *ACS Nano* 2015, 9 (10), 9451–9469.
- (3) Gao, L. Flexible Device Applications of 2D Semiconductors. *Small* 2017, 13 (35), 1603994–1604018.
- (4) Choi, W.; Choudhary., et. al. Recent Development of Two-Dimensional Transition Metal Dichalcogenides and Their Applications. *Mater. Today* 2017, 20(3), 116–130.
- (5) Ferrari, A. C., et. al. Science and Technology Roadmap for Graphene, Related Two-Dimensional Crystals, and Hybrid Systems. *Nanoscale* 2015, 7 (11), 4598–4810.

- (6) Li, Y., et. al. Anti-Ambipolar Field-Effect Transistors Based On Few-Layer 2D Transition Metal Dichalcogenides. *ACS Appl. Mater. Interfaces* 2016, 8 (24), 15574–81.
- (7) Duan, X., et. al. Two-Dimensional Transition Metal Dichalcogenides as Atomically Thin Semiconductors: Opportunities and Challenges. *Chem. Soc. Rev.* 2015, 44 (24), 8859–8876.
- (8) Novoselov, K. S., et. al. 2D Materials and Van der Waals Heterostructures. *Science* 2016, 353 (6298), aac9439.
- (9) Bao, X., et. al. Band Structure Engineering in 2D Materials for Optoelectronic Applications. *Advanced Materials Technologies* 2018, 3 (11), 1800072–1800085.
- (10) Duan, X., et. al. Synthesis of WS_2xSe_{2-2x} Alloy Nanosheets with Composition-Tunable Electronic Properties. *Nano Lett.* 2016, 16 (1), 264–269.
- (11) Cheng, R., et. al. Electroluminescence and Photocurrent Generation from Atomically Sharp WSe_2/MoS_2 Heterojunction p-n Diodes. *Nano Lett.* 2014, 14 (10), 5590–5597.
- (12) Mann, J., et. al. 2-Dimensional Transition Metal Dichalcogenides with Tunable Direct Band Gaps: $MoS_2(1-x)Se_{2x}$ Monolayers. *Adv. Mater.* 2014, 26 (9), 1399–1404.
- (13) Li, H.; Duan., et. al. Growth of Alloy $MoS_2xSe_{2(1-x)}$ Nanosheets with Fully Tunable Chemical Compositions and Optical Properties. *J. Am. Chem. Soc.* 2014, 136 (10), 3756–3759.
- (14) Furchi, M. M., et. al. Photovoltaic Effect in an Electrically Tunable van der Waals Heterojunction. *Nano Lett.* 2014, 14 (8), 4785–4791.
- (15) Gong, Y., et. al. Vertical and In-Plane Heterostructures from WS_2/MoS_2 Monolayers. *Nat. Mater.* 2014, 13, 1135–1155.
- (16) Wang, Q. H., et. al. Electronics and Optoelectronics of Two-Dimensional Transition Metal Dichalcogenides. *Nat. Nanotechnol.* 2012, 7 (11), 699–712.

- (17) Butler, S. Z., et. al. Progress, Challenges, and Opportunities in Two-Dimensional Materials beyond Graphene. *ACS Nano* 2013, 7 (4), 2898–2926.
- (18) Radisavljevic, B., et. al. Single-Layer MoS₂ Transistors. *Nat. Nanotechnol.* 2011, 6 (3), 147–150.
- (19) Akinwande, D., et. al. A Review on Mechanics and Mechanical Properties of 2D Materials Graphene and Beyond. *Extreme Mechanics Letters* 2017, 13, 42–77.
- (20) Mak, K. F.; Shan, J. Photonics and Optoelectronics of 2D Semiconductor Transition Metal Dichalcogenides. *Nat. Photonics* 2016, 10 (4), 216–226.
- (21) Cho, B., et. al. Chemical sensing of 2D graphene/MoS₂ heterostructure device. *ACS Appl. Mater. Interfaces* 2015, 7 (30), 16775–16780.
- (22) Xu, M., et. al. Graphene-like Two-Dimensional Materials. *Chem. Rev.* 2013, 113 (5), 3766–3798.
- (23) Moving Towards The Market. *Nat. Mater.*, 2019, 18(6) 519–519.
- (24) Masubuchi, S., et. al. Autonomous Robotic Searching and Assembly of Two-Dimensional Crystals to Build Van der Waals Superlattices. *Nat. Commun.* 2018, 9 (1), 1413–1424.
- (25) Choudhary, N., et. al. Centimeter Scale Patterned Growth of Vertically Stacked Few Layer Only 2D MoS₂/WS₂ Van der Waals Heterostructure. *Sci. Rep.* 2016, 6, 25456–25462.
- (26) Geim, A. K., et. al. Atomically Thin p-n Junctions with Van der Waals Heterointerfaces. *Nat. Nano technol.* 2014, 9, 676–681.
- (27) Bonaccorso, F., et. al. Production and Processing of graphene and 2D Crystals. *Mater. Today* 2012, 15 (12), 564–589.
- (28) Kang, K., et. al. Layer-By-Layer Assembly of Two-Dimensional Materials into Wafer-Scale Heterostructures. *Nature* 2017, 550 (7675), 229–233.

- (29) Kim, J. H., et. al. Centimeter-scale Green Integration of Layer-by-Layer 2D TMD vdW Heterostructures on Arbitrary Substrates by Water-Assisted Layer Transfer. *Sci. Rep.* 2019, 9 (1), 1641–1650.
- (30) Zhang, F., et. al. Etchant-Free Transfer of 2D Nanostructures. *Nanotechnology* 2018, 29 (2), 025602–025607.
- (31) Islam, M. A., et. al. Centimeter-Scale 2D van der Waals Vertical Heterostructures Integrated on Deformable Substrates Enabled by Gold Sacrificial Layer-Assisted Growth. *Nano Lett.* 2017, 17 (10), 6157–6165.
- (32) Gurarslan, A., et. al. Surface-Energy-Assisted Perfect Transfer of Centimeter-Scale Monolayer and Few-Layer MoS₂ Films onto Arbitrary Substrates. *ACS Nano* 2014, 8 (11), 11522–11528.
- (33) Zhang, L., et. al. Damage-Free and Rapid Transfer of CVD-Grown Two-Dimensional Transition Metal Dichalcogenides by Dissolving Sacrificial Water-Soluble Layers. *Nanoscale* 2017, 9 (48), 19124–19130.
- (34) Lee, C. H., et. al. Transferred Large Area Single Crystal MoS₂ Field Effect Transistors. *Appl. Phys. Lett.* 2015, 107 (19), 193503–193507.
- (35) Jin, G., et. al. Atomically Thin Three-Dimensional Membranes of Van der Waals Semiconductors by Wafer-Scale Growth. *Science Advances* 2019, 5 (7), No. eaaw3180.
- (36) Hwang, J.-H., et. al. Improving Electrochemical Pb²⁺ Detection Using a Vertically Aligned 2D MoS₂ Nanofilm. *Anal. Chem.* 2019, 91 (18), 11770–11777.
- (37) Islam, M. A., et. al. Three dimensionally-ordered 2D MoS₂ vertical layers integrated on flexible substrates with stretch-tunable functionality and improved sensing capability. *Nanoscale* 2018, 10 (37), 17525–17533.
- (38) Islam, M. A., et. al. Noble Metal-Coated MoS₂ Nanofilms with Vertically-Aligned 2D Layers for Visible Light-Driven Photocatalytic Degradation of Emerging Water Contaminants. *Sci. Rep.* 2017, 7 (1), 14944–14953.

- (39) Okogbue, E., et. al. Multifunctional Two-Dimensional PtSe₂-Layer Kirigami Conductors with 2000% Stretchability and Metallic-to-Semiconducting Tunability. *Nano Lett.* 2019, 19, 7598–7607.
- (40) Okogbue, E., et. al. Centimeter-Scale Periodically Corrugated Few-Layer 2D MoS₂ with Tensile Stretch- Driven Tunable Multifunctionalities. *ACS Appl. Mater. Interfaces* 2018, 10 (36), 30623–30630.
- (41) Han, S. S., et. al. Horizontal-to-Vertical Transition of 2D Layer Orientation in Low-Temperature Chemical Vapor Deposition- Grown PtSe₂ and Its Influences on Electrical Properties and Device Applications. *ACS Appl. Mater. Interfaces* 2019, 11 (14), 13598–13607.
- (42) Jung, Y., et. al. Metal seed layer thickness-induced transition from vertical to horizontal growth of MoS₂ and WS₂. *Nano Lett.* 2014, 14 (12), 6842–6849.
- (43) Van Artsdalen, E. R.; Yaffe, I. S. Electrical Conductance and Density of Molten Salt Systems: KCl-LiCl, KCl-NaCl and KCl-KI. *J. Phys. Chem.* 1955, 59 (2), 118–127.
- (44) Fei, L., et. al. Direct TEM Observations of Growth Mechanisms of Two-Dimensional MoS₂ Flakes. *Nat. Commun.* 2016, 7, 12206–12212.
- (45) Kong, D., et. al. Synthesis of MoS₂ and MoSe₂ Films with Vertically Aligned Layers. *Nano Lett.* 2013, 13 (3), 1341–1347.
- (46) Choudhary, N., et. al. Strain-Driven and Layer-Number-Dependent Crossover of Growth Mode in van der Waals Heterostructures: 2D/2D Layer-By-Layer Horizontal Epitaxy to 2D/3D Vertical Reorientation. *Adv. Mater. Interfaces* 2018, 5 (14), 1800382–1800391.
- (47) Guo, J., et. al. Oxygen-Incorporated MoS₂ Ultrathin Nanosheets Grown on Graphene for Efficient Electrochemical Hydrogen Evolution. *J. Power Sources* 2015, 291, 195–200.
- (48) Chiappe, D., et. al. A. Controlled Sulfurization Process for the Synthesis of Large Area MoS₂ Films and MoS₂/WS₂ Heterostructures. *Adv. Mater. Interfaces* 2016, 3 (4), 1500635–1500644.

- (49) Ganta, D.; Sinha, S.; Haasch, R. T. 2-D Material Molybdenum Disulfide Analyzed by XPS. *Surf. Sci. Spectra* 2014, 21 (1), 19–27.
- (50) Kumar, P.; Viswanath, B. Horizontally and Vertically Aligned Growth of Strained MoS₂ Layers with Dissimilar Wetting and Catalytic Behaviors. *CrystEngComm* 2017, 19 (34), 5068–5078.
- (51) Kalita, H., et. al. Artificial Neuron Using Vertical MoS₂/Graphene Threshold Switching Memristors. *Sci. Rep.* 2019, 9 (1), 53–60.
- (52) Zeng, L.-H., et. al. Fast, Self-Driven, Air-Stable, and Broadband Photodetector Based on Vertically Aligned PtSe₂/GaAs Heterojunction. *Adv. Funct. Mater.* 2018, 28 (16), 1705970–1705980.
- (54) Li, H., et. al. Experimental Realization of Few Layer Two-Dimensional MoS₂ Membranes of Near Atomic Thickness for High Efficiency Water Desalination. *Nano Lett.* 2019, 19 (8), 5194–5204.

Chapter 4. Application to Stretchable Future

Electronics

4.1. High Stretchable Electronic Device

The contents of this section have been published in: Emmanuel Okogbue, Sang Sub Han, Tae-Jun Ko, Hee-Suk Chung, Jinwoo Ma, Mashiyat Sumaiya Shawkat, Jung Han Kim, Jong Hun Kim, Eunji Ji, Kyu Hwan Oh, Lei Zhai, Gwan-Hyoung Lee and Yeonwoong Jung “Multifunctional Two-Dimensional PtSe₂-Layer Kirigami Conductors with 2000% Stretchability and Metallic-to-Semiconducting Tunability” Nano Lett. 19, 7598–7607 (2019).

4.1.1. Introduction

A variety of approaches have been explored to convert intrinsically brittle electronic materials to stress-resilient forms by rationally engineering their physical configurations and dimensions.[1–2] Among them, forming the materials into “kirigami” patterns inspired by the ancient paper-cutting art[4, 5] offers distinguishable advantages for efficiently relieving external stress.[9–11] This kirigami patterning employs rows of designed cuts to a planar material, which improves its mechanical stretchability by converting applied tensile stress to torsional stress at specific points between the cuts.[11–17] In addition to structural “engineering” approaches, substantive efforts have been used to identify a new form of electronic materials which intrinsically possess suitable crystallinity to enable superior mechanical tolerance. In this endeavor, recently explored two-dimensional (2D) transition metal dichalcogenides (TMDs) present highly unique and promising aspects.[18, 19] For instance, they exhibit significantly larger in-plane strain limits over covalently bonded three-

dimensional crystals owing to their van der Waals molecular bonding, offering opportunities for futuristic stretchable electronics.[18, 20] Despite the projected advantages, combining these two different compelling approaches (i.e., converting 2D TMDs into kirigami forms) has been rarely attempted, leaving their anticipated mechanoelectrical superiority largely unexplored. While some proof-of-concept demonstrations have been predicted by theory,[21, 22] the experimental realization of “stand-alone” 2D TMD-based kirigami patterning has been unavailable. This limitation is attributed to the technical difficulty associated with reliably handling extremely thin 2D layers in a free-standing form. As a result, limited success has been demonstrated with the graphene kirigami of a very small dimension ($\leq 100 \mu\text{m}^2$) realized by highly sophisticated lithographic fabrication processes.[23] Directly integrating 2D TMDs into kirigami-patterned secondary substrates of high mechanical flexibility and electrical insulation (e.g., plastics) can be a viable alternative. Although it is desirable to grow 2D TMDs directly on flexible substrates for subsequent kirigami patterning, the intrinsically high growth temperatures inherent to most 2D TMDs have made this approach technically challenging. For instance, the chemical vapor deposition (CVD) growth of conventional 2D TMDs such as molybdenum (Mo) disulfides (MoS_2) generally requires a high temperature of $>500 \text{ }^\circ\text{C}$ which pristine plastics cannot withstand.[24–29] Alternately, the mechanical integration of separately grown 2D MoS_2 layers onto kirigami-patterned plastics has been pursued.[30] This technique achieved poor electrical retention under stretching (i.e., tensile strain $<100\%$), significantly falling short of theoretically predicted advantages.

Herein, we employed the kirigami strain engineering concept in 2D TMDs by directly growing them on plastic substrates and investigated the resulting mechano-electrical responses. Among a variety of 2D TMDs, we employed 2D platinum diselenide (2D PtSe₂) layers with an intrinsically much lower growth temperature than for conventional 2D TMDs as well as layer-thickness-dependent semiconducting-to-metallic transition characteristics.[31, 32] We directly grew 2D PtSe₂ layers of controlled morphology and transport characteristics on polyimide (PI) substrates at 400 °C via CVD reaction and subsequently created centimeter-scale kirigami patterns. We then explored their strain-tunable and/or invariant electrical and optical properties via various characterization. The metallic 2D PtSe₂/PI kirigami of optimized pattern geometries presented excellent electrical retention up to ~2000% tensile strain. Moreover, they exhibited strain-tunable photocurrent generation and modulation upon incorporating semiconducting carbon nanotubes (CNTs) by the formation of CNT/2D PtSe₂ Schottky junctions in kirigami forms. We also explored highly stretchable kirigami field-effect transistors (FETs) by employing semiconducting 2D PtSe₂ layers and identified their *p*-type responses to electrolyte gating. The exclusive role of the kirigami pattern geometry in the resulting mechano-electrical properties was also verified by finite element method (FEM) simulation.

4.1.2. Experimental Method

4.1.2.1. Preparation of a Kirigami-Patterned PI Substrate

Kirigami patterning of the PI substrate with systematic linear cuts was carried out using a CO₂ laser cutter (Universal ILS12.150D, 150 W capacity)

with a 10.6 μm infrared laser. The substrate was placed on the equipment bed, and the laser cutting process was performed in the presence of constant air cooling and gas suction to prevent the release of any toxic fumes and the burning of the material. The optimal cutting conditions for minimizing the heat zone and burning effect from the laser have been identified as follows: laser power of 60%, laser speed of 100%, and pulse per inch of 600.

4.1.2.2. Two-Dimensional PtSe₂ Layer Growth

Two-dimensional PtSe₂ layers were grown on the kirigami-patterned PI substrate in a home-built CVD system based on a horizontal quartz tube furnace (Lindberg/Blue M Mini-Mite). An electron beam evaporator (Temescal) was used to deposit Pt seeds of controlled thickness at a constant evaporation rate of 0.15 $\text{\AA}/\text{s}$. The Pt-deposited patterned PI substrate was placed in the middle zone of the CVD furnace with an alumina boat containing selenium (Se) preloaded at the furnace's upstream side. The quartz tube was pumped down to a pressure of ~ 1 mTorr and was subsequently purged with argon (Ar) to remove residual gases. The furnace was heated to a growth temperature of 400 $^{\circ}\text{C}$ while Se was evaporated at ~ 200 $^{\circ}\text{C}$ for a dwell time of 50 min under a continuous flow of Ar gas (~ 100 standard cubic centimeters per minute (SCCM)). Upon completion of the CVD reaction, the furnace was allowed to cool to room temperature naturally.

4.1.2.3. Electrical and Optoelectrical Characterization

For electrical characterization, two-terminal devices were fabricated by depositing gold contacts on the ends of the kirigami 2D PtSe₂/PI pattern. I–V transfer characteristics were recorded by using a home-built probe station

connected to a semiconductor parameter analyzer (HP 4156 A). For optoelectrical characterization, the electrical response of the device was recorded under illumination from a white LED of controlled intensity. Strain-dependent electrical and optoelectrical properties were obtained by operating the devices mounted on a home-built tensile stretcher.

4.1.2.4. XPS and TEM/STEM Characterization

XPS characterization was performed using a Thermo VG Scientific K- α system equipped with an Al K α -ray source (1486.3 eV) under ultrahigh vacuum. The energy resolution of the instrument is better than 0.5 eV, and a 100 W X-ray spot of 400 μm^2 was used for surface scans with a pass energy of 50 eV. All XPS peaks are calibrated using the binding energy of C 1s, 284.5 eV, and a Shirley-type background and a Voigt function were used for peak fitting. TEM/STEM characterization was performed using JEOL ARM200F FEG-TEM/STEM with a Cs (spherical aberration) corrector. Plane-view TEM samples were prepared by delaminating the 2D PtSe₂ layers from PI substrates inside the water and by transferring them to carbon TEM grids. Cross-sectional TEM samples were prepared by focused ion beam (FIB) milling and lift-out techniques using a Quanta 2D FEG, FEI. As-grown 2D PtSe₂ layers/PI substrates were coated with a carbon film of ~100 nm thickness and were subsequently cross-sectioned using a FIB-Ga ion beam of 30 keV. All TEM/STEM operations were performed at an accelerating voltage of 200 kV.

4.1.3. Results and Discussion

4.1.3.1. The Manufacturing Process of High Stretchable 2D PtSe₂/PI

Kirigami Device

Figure 4. 1 is the schematic depiction of the process used to fabricate a 2D PtSe₂/PI kirigami. The process begins with obtaining a kirigami-patterned electrically insulating PI substrate, which consists of symmetrical linear cuts achieved by laser beam cutting. The cutting parameters are optimized to ensure minimal heat zones on the PI substrate and no damage to its pristine mechanical properties through the laser process.[33] The substrate is subsequently cleaned in water by sonication to remove residual impurities resulting from the pattern fabrication. A Pt thin film of ~6–8 nm thickness is deposited onto the kirigami-patterned PI substrate via e-beam evaporation for subsequent thermal selenization.[28] With this thickness, 2D PtSe₂ layers grow in a “vertical” orientation with individual 2D layers standing upright, exposing their edges on the surface as confirmed in the next section. The Pt-deposited kirigami substrate is then put into a CVD furnace to convert Pt to 2D PtSe₂ layers at 400 °C. This temperature is high enough to ensure the complete thermal selenization of Pt[32, 34, 35] and is low enough not to deform the underlying PI substrate. Finally, gold (Au) contacts are deposited on the two ends of the 2D PtSe₂/PI kirigami for electrical characterization under tensile stretching. During the stretching process, the kirigami pattern leads to a reduction in its in-plane stiffness, causing the out-of-plane buckling of constituting struts allowing for high elasticity as depicted in the scheme (verified in a later section).[36]

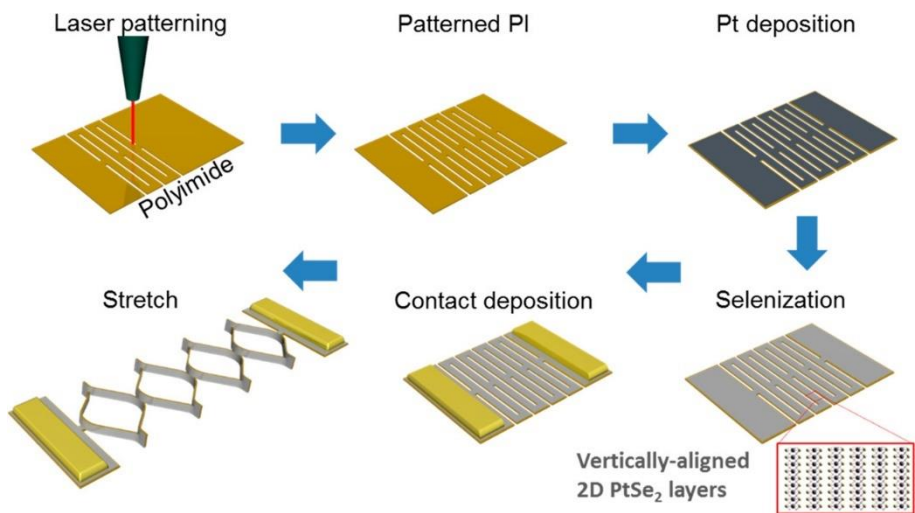


Figure 4. 1. Schematic of the fabrication processes for kirigami-patterned, vertically aligned 2D PtSe₂ layers on a flexible PI substrate.

4.1.3.2. Structural and Chemical Analysis of 2D PtSe₂ Layers

Before evaluating the mechanoelectrical performance of 2D PtSe₂/PI kirigami patterns, we first confirmed the successful growth of 2D PtSe₂ layers on PI substrates by characterizing their as-grown morphology. We employed a variety of characterization techniques including X-ray photoelectron spectroscopy (XPS), transmission electron microscopy (TEM), and energy-dispersive X-ray spectroscopy (EDS). Figure 4. 2a shows an image of a bare PI substrate (left) and a Pt deposited PI substrate after CVD selenization (right), revealing distinguishable color contrast. We identified the chemical composition of the Pt-deposited PI substrate which underwent CVD selenization. Figure 4. 2b, c shows the XPS core-level spectra of Pt 4f and Se 3d obtained from the Pt-deposited PI substrates after CVD selenization and their corresponding spin-orbit splitting values of 3.3 and 1.1 eV, respectively. As shown in Figure 4. 2b, the Pt 4f spectrum was featured to present a high symmetry of the spectral profiles with a narrow fullwidth at half-maximum of ~1 eV. Moreover, Pt 4f exhibits no observable signal produced by elemental Pt (the expected position of Pt 4f_{7/2} is ~71 eV), indicating that the entire spectrum can be assigned to Pt⁴⁺ corresponding to PtSe₂. Se 3d spectra can be deconvoluted into two chemical states, as presented in Figure 4. 2c. The predominant spectrum represents PtSe₂, whose spin-up state ($j = 2 + 1/2$) is located at 54.1 eV. On the other hand, the humplike small peak centered at ~58.6 eV is associated with the oxidation of Se to SeO₂ or SeO₃.^[37] The element ratio of Pt/Se calculated from the XPS spectrum is 0.55, which indicates the formation of stoichiometric 2D PtSe₂ layers. TEM

characterization was employed to investigate the microstructure of the 2D PtSe₂ layers directly grown on PI substrates. Figure 4. 2d shows a low-magnification TEM of isolated 2D PtSe₂ layers revealing spatially homogeneous imaging contrast. The corresponding selected area electron diffraction (SAED) pattern in Figure 4. 2e presents multiple diffraction rings which are indexed to the crystalline planes of (100), (001), (101), and (110) in hexagonal 2D PtSe₂. [38, 39] The EDS spectrum in Figure 4. 2f obtained from the same sample indicates that the stoichiometric atomic ratio of Pt/Se is 1:2, which is in agreement with the XPS results. The corresponding EDS mapping images in Figure 4. 2g confirm the highly homogeneous spatial distribution of Pt and Se, indicating the complete conversion of Pt and Se to PtSe₂. Figure 4. 2h shows a high-resolution TEM (HRTEM) image of the sample corresponding to Figure 4. 2d–g. The image reveals that the material consists of multiple domains of vertically aligned 2D PtSe₂ layers in various crystallographic orientation exposing their 2D edge sites on the surface. Figure 4. 2i is the corresponding scanning TEM (STEM) image revealing vertically aligned 2D PtSe₂ layer edges with an interlayer spacing of ~0.54 nm. This value corresponds to the (001) crystalline plane of 2D PtSe₂ layers, as illustrated in the schematic of their atomic structures. [40, 41]

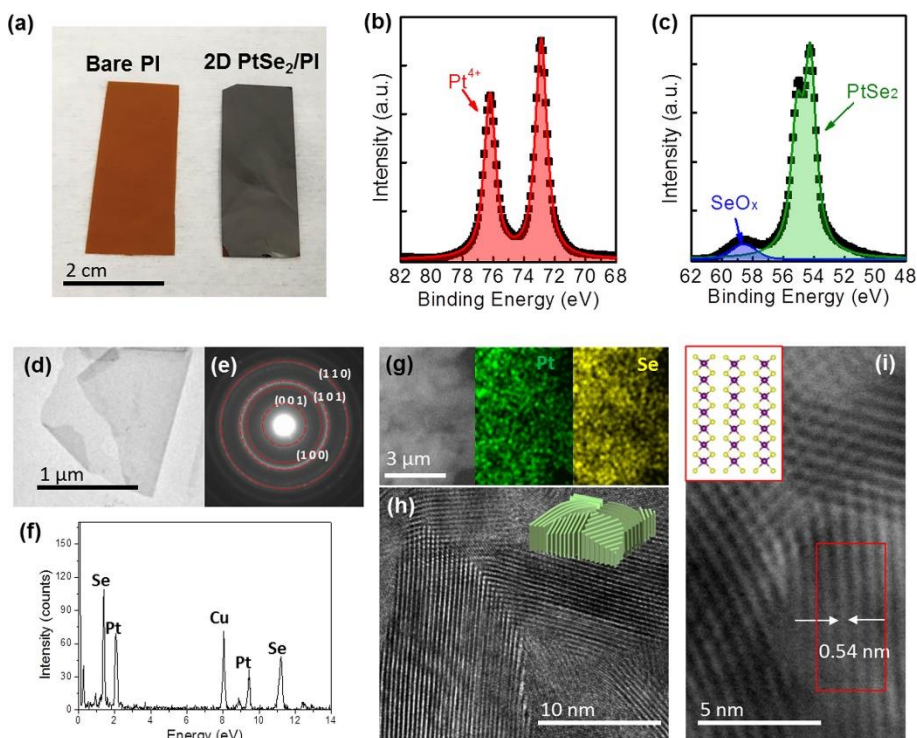


Figure 4. 2. (a) Camera images showing a bare PI (left) and an as-grown 2D PtSe₂ layers-on-PI substrate prepared by the CVD selenization of 8 nm Pt (right). (b and c) XPS characterization of (b) Pt 4f and (c) Se 3d core levels obtained from 2D PtSe₂ layers on PI substrates. (d) Low-magnification plane-view TEM image of 2D PtSe₂ layers isolated from their PI growth substrates. (e) SAED indexing, (f) EDS spectrum profile, and (g) EDS mapping images obtained from the corresponding 2D PtSe₂ layers. (h) HRTEM image of the corresponding sample showing vertically aligned 2D PtSe₂ layers along with their schematic illustration (inset). (i) STEM image showing the edges of vertically aligned 2D PtSe₂ layers with an interlayer spacing of ~0.54 nm, corresponding to the schematic illustration in the inset.

4.1.3.3. The Mechanical Properties of 2D PtSe₂/PI Device

Having confirmed the successful fabrication of 2D PtSe₂/PI kirigami patterns enabled by the low-temperature direct growth of 2D PtSe₂ layers, we investigated their mechano-electrical performances. Prior to that, we first studied the transport properties of as-grown 2D PtSe₂ layers on a SiO₂/Si substrate in a field-effect-transistor (FET) configuration to identify their intrinsic carrier types. Our vertically aligned 2D PtSe₂ layers exhibit metallic carrier transport with no detectable FET gate responses, consistent with the previously reported 2D PtSe₂ layers of comparable thickness.[34, 42, 43] Details of FET characterization are presented in the next section. In designing the kirigami pattern, we considered the geometrical and dimensional influences of the pattern on the resulting electrical properties under mechanical deformation. We attempted to maximize the retention of electrical conductance under tensile stretch by applying optimized parameters to the kirigami pattern design. The schematic in Figure 4. 3a presents the kirigami pattern of symmetrical linear cuts where key characteristic parameters are defined as follows: a is the cut length, b is the spacing between two cuts perpendicular to the direction of tensile force, and c is the vertical spacing between the linear cuts parallel to the direction of tensile force. On the basis of the beam theory which models the mechanical deflection of a strut,[44, 45] the relationship between the critical tensile force (F) and the characteristic parameters is given as

$$F \propto \frac{Ect^3}{(a-b)^3} \quad - \quad \text{eq. 4. 1}$$

where E is Young's modulus and t is the thickness of the strut as deflection

occurs along its length. The equation indicates that an increase in the cut length leads to a reduction in the critical buckling length, thereby allowing for continued elongation along the direction of applied force. Similarly, decreasing the vertical and horizontal spacing improves the maximum attainability of strain. Note that the strain is defined as $\varepsilon = \Delta l/l_0$, where l_0 is the initial length of the kirigami before stretching and Δl is the increase in the length upon stretching. The maximum strain attainable by the kirigami is proportional to the cut length a and is inversely proportional to the lateral and vertical spacing of b and c , while the number of columns and rows within the pattern has a negligible impact.[36, 44] Considering the above relationship between the maximum strain and characteristic parameters, we applied the following parameters to achieve maximum lateral stretchability in the 2D PtSe₂/PI kirigami and investigated its resulting electrical properties upon stretching: $a = 17.2$ mm, $b = 0.4$ mm, and $c = 0.375$ mm. Figure 4. 3a shows the current response of a 2D PtSe₂/PI kirigami pattern with these parameters under varying strain levels applied by manual stretching. The kirigami pattern exhibits a negligible current drop of $\lesssim 5\%$ even up to 2000% strain, confirming its excellent electrical retention. Figure 4. 3b shows the two-terminal current–voltage (I–V) characteristics of the corresponding sample revealing the ohmic nature of metallic 2D PtSe₂ layers as manifested by the high linearity of I–V. We note that this 2000% retention achieved with 2D PtSe₂ layer-based kirigami is orders of magnitude higher than the stretchability of other experimentally demonstrated 2D MoS₂ layer-based kirigami patterns[30] and outperforms most of the state-of-the-art kirigami-patterned electrical

conductors.[10, 13, 36, 44, 45] We then investigated the failure characteristics of kirigami patterns, for which we employed the in situ monitoring of current-strain variation until their electrical breakdown. We first manually stretched another sample to 1000% strain and loaded it into an automated tensile stretcher before applying controlled strain. Figure 4. 3c shows that the sample exhibits an electrical failure at ~2350% strain accompanying a drastic current drop within ~5% before the failure point. The inset of the Figure corresponds to the red boxed regime detailing the failure characteristics. For further assessment of the strain-invariant electrical stability of kirigami patterns, we performed cyclic tests by repeatedly stretching and releasing them up to a fixed strain. Figure 4. 3d presents the current variation of another kirigami sample undergoing a large number of cyclic stretching up to 1000 times at 1000% strain. The result confirms the excellent mechanical stability of the kirigami in terms of retaining its original electrical conductance throughout severe mechanical deformation. It is worth mentioning that previously developed nanomaterialsbased kirigami patterns are mostly based on the solution integration of active materials,[8] while our approach employs the direct growth of 2D materials in kirigami form. This integration advantage leads to the excellent structural integrity of 2D PtSe₂ layers on PI substrates, which is believed to be responsible for the observed superiority of electrical retention. In addition to the mechanical and physical stability confirmed by the cyclic test and TEM characterization, respectively, we have investigated the environmental stability of 2D PtSe₂/PI kirigami materials. Specifically, we have characterized the chemical states of 2D PtSe₂/PI samples in the as-grown

state and after ~10 months of air exposure at ambient temperature and compared their characteristics. XPS characterization identifies that the envelopes of both Pt 4f spectra are nearly identical, which indicates that the 4+ valence state of Pt is well retained even after prolonged air exposure. The shapes of Se 3d spectra pertaining to PtSe₂ are also very similar to a slight reduction in SeO_x.

Having proven the superior structural and electrical integrity of 2D PtSe₂/PI kirigami materials, we explored their potential applications which take advantage of strain-invariant metallic transports. We first utilized them as stretchable conductors for operating small electronic devices for which we demonstrated the powering up of a light emitting diode (LED), as illustrated in Figure 4. 3f. The optimized 2D PtSe₂/PI kirigami used for Figure 4. 3a–e was connected to an LED light and was stretched from 0 to 1500% by an automated tensile stretcher. Figure 4. 3g demonstrates that the light intensity (2 W/m²) of the LED remains unchanged even up to 1500% strain (denoted by the red circles in both Figures), indicating unimpaired charge transports in 2D PtSe₂ layers.

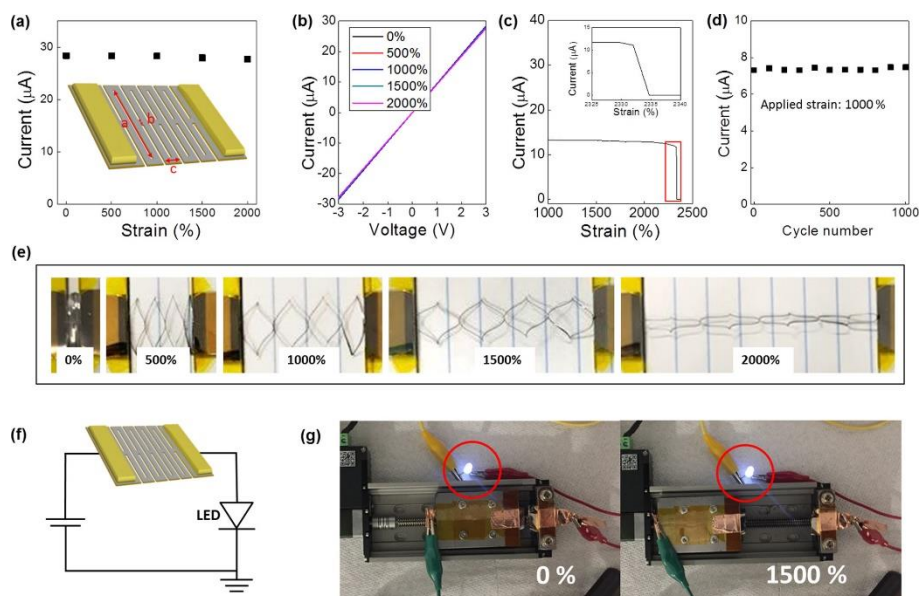


Figure 4. 3. (a) Variation of current in an optimized 2D PtSe₂/PI kirigami up to 2000% strain. The inset illustrates the corresponding kirigami design with $a = 17.2$ mm, $b = 0.4$ mm, and $c = 0.375$ mm. (b) Two-terminal I–V transport characteristics of the same kirigami compared at various strain levels. (c) Electrical failure obtained from another kirigami beyond $\sim 2300\%$ strain. (d) Cyclic test to show the variation in current with a large number of repeated stretchings measured at 3 V. (e) Camera images of the kirigami corresponding to (a) and (b) upon manual stretching up to 2000% strain. (f) Schematic of an LED continuity circuit using a 2D PtSe₂/PI kirigami as a stretchable conductor. (g) Demonstration of lighting up an LED by a 2D PtSe₂/PI kirigami stretched to 0 and 1500%.

4.1.3.4. FEM Simulation for the Optimization of Device Design

To clarify the mechanism behind the excellent strain-invariant electrical performance of 2D PtSe₂ layer-based kirigami patterns, we employed FEM simulation and studied the geometrical effects of kirigami patterns on the strain distribution introduced by a tensile stretch. We studied the patterns of two different configurations (i.e., unoptimized parameters of $a = 6.5$ mm, $b = 1.63$ mm, $c = 1.75$ mm and optimized parameters of $a = 17.2$ mm, $b = 0.4$ mm, and $c = 0.375$ mm as shown in the left and right schematics in Figure 4. 4a, respectively). FEM simulation images used to describe the spatial distribution of “global” strain on the unoptimized vs optimized patterns under stretching are presented in Figure 4. 4b, c, respectively. The unoptimized pattern in Figure 4. 4b shows that the large vertical and horizontal spacings (b and c) between the struts limit their torsional rotation, causing a high strain concentration at the cut edges even at a low strain level of $\lambda \approx 1.6$; λ is the stretch coefficient defined by $\lambda = l/l_0$, where l_0 and l denote the length before and after the stretch, respectively. On the other hand, upon stretching the kirigami with optimized parameters (Figure 4. 4c), the applied tensile force causes the pattern to readily rotate around the cut edges (orange and yellow boxes) of high strain localization. This rotation results in an efficient relaxation of accumulating strain, preserving the intrinsic electrical conduction with λ being much larger than that observed with the unoptimized kirigami. Figure 4. 4d compares the maximum in-plane principal strain values as a function of λ for the unoptimized vs optimized patterns. The maximum in-plane principal values are obtained from the edge cut areas of higher local strain presented in Figure 4. 4b, c. Because kirigami

patterns present complex strain tensors owing to their multidirectional deformation, the maximum in-plane principal strain was chosen for performance comparison. It is noted that significantly smaller maximum in-plane principal strain is realized in the optimized pattern at a given λ , suggesting its high stretchability until the failure point of >0.1 . Moreover, the optical images of the experimentally realized kirigami patterns (insets; colored in gray) look nearly identical to the simulated ones, indicating the excellent controllability of our patterning process. It is noteworthy that the major motive for presenting the two cases of “unoptimized” vs “optimized” patterns is to demonstrate the controllability of lateral stretching in the kirigami patterns by rationally defining the dimensional parameters. The criterion for achieving a large degree of stretchability is to increase the length (a) of constituting trusts and simultaneously decreasing their widths (b and c). Accordingly, the failure point of the kirigami should appear at λ of a much larger value, which corresponds to larger stretchability. The unoptimized kirigami pattern electrically breaks down at $\sim 75\%$ strain as experimentally observed, which is significantly smaller than that achieved with the optimized pattern (Figure 4. 3e) as predicted above. To further demonstrate the role of kirigami pattern designs on controlling the resultant performance, we have carried out additional FEM simulations by varying the dimensional parameters of a , b , and c in eq 4. 1. Figure 4. 4e–g shows the variation of maximum in-plane principal strain with varying a , b , and c , respectively. The analysis confirms that the stretch levels corresponding to the approximately defined failure point of 0.1 maximum in-plane principal strain drastically increase with larger a and smaller b and c . This

observation indicates that the kirigami pattern can be significantly more stretched (e.g., up to ~4000%) over what we have experimentally demonstrated by further adjusting the dimensional parameters. In this work, we have judiciously and intentionally selected the optimized parameters of a, b, and c and achieved the maximum stretchability of >2000% to avoid the technical difficulty associated with manually handling samples with b and c parameters that are too small.

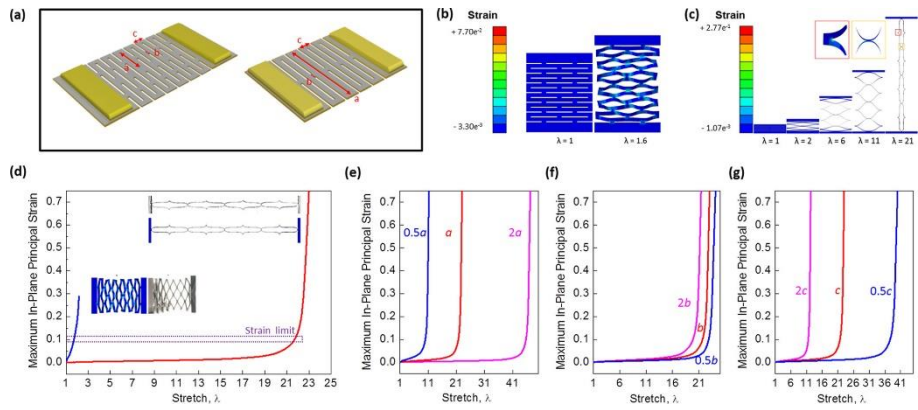


Figure 4. 4. (a) Schematics showing the defining geometrical parameters for the unoptimized (left) vs optimized (right) kirigami patterns. (b, c) FEM simulations showing the strain distribution within the kirigami patterns of (b) unoptimized and (c) optimized parameters. (d) Graphical comparison of maximum in-plane principal strain vs stretch for the unoptimized (blue plot) vs optimized (red plot) kirigami patterns. The inset compares the simulated vs experimentally demonstrated images of kirigami patterns while their failure point is approximated to be ~ 0.1 times the maximum in-plane principal strain. (e–g) Plots of maximum in-plane principal strain vs stretch with varying geometrical parameters of (e) a, (f) b, and (g) c.

4.1.3.5. Stretchable FET Device of 2D PtSe₂/PI Layer

Finally, we further explored the application aspects of 2D PtSe₂/PI kirigami patterns by taking advantage of the tunable electrical properties of 2D PtSe₂ layers of precisely controlled morphology. Two-dimensional PtSe₂ layers exhibit a semiconducting-to-metallic transition as their layer morphology and thickness vary, as modulated by CVD growth conditions[40–43, 46] (i.e., vertically aligned thick 2D PtSe₂ layers exhibit metallic transport while horizontally aligned thin layers are semiconducting[46]). While the above demonstrations (Figures 4. 3) focus on utilizing the metallic transport of 2D PtSe₂ layers, we further extend the kirigami approach to exploit their semiconducting properties in unconventional electronic applications, including kirigami FETs. To this end, we grew semiconducting 2D PtSe₂ layers in the horizontal orientation by selenizing Pt of small thickness (typically <1 nm) under CVD conditions identical to those mentioned above.[46] Figure 4. 5a shows a HRTEM image of horizontally aligned 2D PtSe₂ layers directly grown on PI revealing multiple crystalline grains and Moiré fringes. Corresponding cross-sectional TEM and EDS characterization further confirm their stoichiometric growth maintaining the horizontal-layer orientation. Prior to exploring the kirigami FET applications, we first carried out control experiments to verify the intrinsic carrier type of the horizontally aligned 2D PtSe₂ layers by characterizing FET gate responses. Figure 4. 5b presents the transfer characteristics of drain-source current vs voltage ($I_{ds}-V_{ds}$) with varying gate voltage (V_g) from a back-gated FET configured on a SiO₂/Si substrate (inset). The plots reveal *p*-type semiconducting FET gate responses (i.e.,

increasing I_{ds} with decreasing V_g at a given V_{ds}). We then attempted to develop FETs incorporating them on PI substrates and eventually their kirigami forms. For the reliable operation of FETs even under mechanical stretching, we employed electrolyte gates (e.g., potassium chloride (KCl)) as a medium to gate the devices as shown in Figure 4. 5c. Horizontally aligned 2D PtSe₂ layers on PI substrates were in top contact with metal electrodes for source-drain patterns which were electrically isolated by poly(dimethylsiloxane) (PDMS). Then, a droplet of KCl (10 mM) was applied on top of the 2D PtSe₂ layers, and it was electrically biased for gating. Figure 4. 5d shows the I_{ds} - V_g transfer characteristics of an electrolyte-gated 2D PtSe₂/PI FET (device image in the inset), and Figure 4. 5e presents its corresponding I_{ds} - V_g transfer characteristics with varying V_g . These characterization results confirm the reliable gate response of 2D PtSe₂/PI FETs, offering a basis for extending them in kirigami form. The identical electrolyte gating approach was applied to 2D PtSe₂/PI kirigami FETs, and Figure 4. 5f exhibits I_{ds} - V_g transfer characteristics from a kirigami sample of varying stretch levels. The plots clearly reveal that *p*-type semiconducting transports are well retained with slightly decreasing I_{ds} during the increasing mechanical stretch. Figure 4. 5g shows the images of the kirigami FETs corresponding to Figure 4. 5f where PDMS is used as a chamber to contain KCl of constant concentration (10 mM). It is worth mentioning that our finding of the strain-invariant I_{ds} - V_g transfer characteristics qualitatively agrees with the observation with the graphene kirigami FETs[23] of smaller dimensions gated under similar electrolyte conditions.

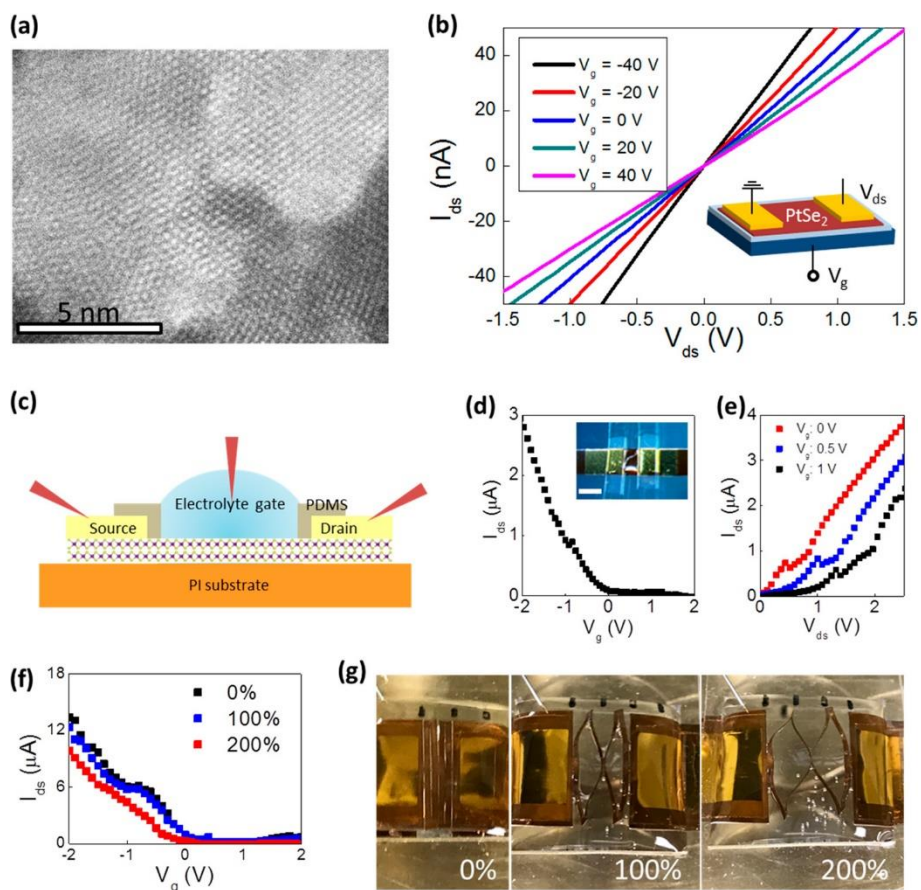


Figure 4. 5. (a) HRTEM image of horizontally aligned thin 2D PtSe₂ layers. (b) I_{ds} - V_{ds} transfer characteristics from a back-gated FET based on horizontally aligned thin 2D PtSe₂ layers conFIGured on a SiO₂/Si wafer. (c) Schematic illustration of an electrolyte gating of a 2D PtSe₂/PI FET. (d) I_{ds} - V_g and (e) I_{ds} - V_{ds} transfer characteristics from a 2D PtSe₂/PI FET. The scale bar in the inset of (d) is 1 mm. (f) I_{ds} - V_g transfer characteristics from a 2D PtSe₂/PI kirigami FET. (g) Camera images of the kirigami FETs corresponding to (f).

4.1.4. Conclusion

We have developed a multifunctional 2D PtSe₂/PI kirigami which exhibits strain-invariable electrical conductance and strain-tunable photo-responsiveness. Metallic 2D PtSe₂ kirigami patterns of optimized dimensions and geometries presented excellent electrical retention up to ~2000% tensile stretch, significantly outperforming previously explored other nanomaterial-based stretchable electrical conductors. Moreover, they presented substantive photocurrent modulation which was reversibly retained throughout significant mechanical deformation. Kirigami FETs were realized by utilizing semiconducting 2D PtSe₂ layers and exhibited electrolyte-driven tunable gate responses under mechanical stretching. This unconventional type of 2D material configured in 3D form offers exciting opportunities for futuristic stretchable and foldable electronics.

4.1.5. Reference

- (1) Okogbue, E.; Kim, J. H.; Ko, T. J.; Chung, H. S.; Krishnaprasad, A.; Flores, J. C.; Nehate, S.; Kaium, M. G.; Park, J. B.; Lee, S. J.; Sundaram, K. B.; Zhai, L.; Roy, T.; Jung, Y. *ACS Appl. Mater. Interfaces* 2018, 10 (36), 30623–30630.
- (2) Islam, M. A.; Kim, J. H.; Ko, T.-J.; Noh, C.; Nehate, S.; Kaium, M. G.; Ko, M.; Fox, D.; Zhai, L.; Cho, C.-H.; Sundaram, K. B.; Bae, T.-S.; Jung, Y.; Chung, H.-S.; Jung, Y. *Nanoscale* 2018, 10 (37), 17525–17533.
- (3) Ko, H.; Javey, A. *Acc. Chem. Res.* 2017, 50 (4), 691–702.
- (4) Song, Z.; Wang, X.; Lv, C.; An, Y.; Liang, M.; Ma, T.; He, D.; Zheng, Y.-J.; Huang, S.-Q.; Yu, H.; Jiang, H. *Sci. Rep.* 2015, 5, 10988–10997.
- (5) Hawkes, E.; An, B.; Benbernou, N. M.; Tanaka, H.; Kim, S.; Demaine, E.

- D.; Rus, D.; Wood, R. J. *Proc. Natl. Acad. Sci. U. S. A.* 2010, 107 (28), 12441–12445.
- (6) Lv, C.; Yub, H. Y.; Jiang, H. Q. *Extreme Mechanics Letters* 2014, 1, 29–34.
- (7) Morikawa, Y.; Yamagiwa, S.; Sawahata, H.; Ishida, M.; Kawano, T. An Origami-Inspired Ultrastretchable Bioprobe Film Device; 2016 IEEE 29th International Conference on Micro Electro-Mechanical Systems (MEMS), Jan 24–28, 2016; pp 149–152.
- (8) Ning, X.; Wang, X.; Zhang, Y.; Yu, X.; Choi, D.; Zheng, N.; Kim, D. S.; Huang, Y.; Zhang, Y.; Rogers, J. A. *Adv. Mater. Interfaces* 2018, 5 (13), 1800284–1800297.
- (9) Callens, S. J. P.; Zadpoor, A. A. *Mater. Today* 2018, 21 (3), 241–264.
- (10) Guan, Y.-S.; Zhang, Z.; Tang, Y.; Yin, J.; Ren, S. *Adv. Mater.* 2018, 30 (20), 1706390–1706398.
- (11) Hwang, D. G.; Bartlett, M. D. *Sci. Rep.* 2018, 8 (1), 3378–3386.
- (12) Sareh, S.; Jonathan, R. *Smart Mater. Struct.* 2013, 22 (1), 014004–014025.
- (13) Guan, Y.-S.; Li, H.; Ren, F.; Ren, S. *ACS Nano* 2018, 12 (8), 7967–7973.
- (14) Huang, G.; Mei, Y. *Small* 2018, 14 (14), 1703665–1703688.
- (15) Bertoldi, K.; Vitelli, V.; Christensen, J.; van Hecke, M. *Nature Reviews Materials* 2017, 2, 17066–17077.
- (16) Xu, L.; Shyu, T. C.; Kotov, N. A. *ACS Nano* 2017, 11 (8), 7587–7599.
- (17) Rafsanjani, A.; Bertoldi, K. *Phys. Rev. Lett.* 2017, 118 (8), 084301–084306.
- (18) Akinwande, D.; Petrone, N.; Hone, J. *Nat. Commun.* 2014, 5, 5678–5690.

- (19) Choudhary, N.; Islam, M. A.; Kim, J. H.; Ko, T.-J.; Schropp, A.; Hurtado, L.; Weitzman, D.; Zhai, L.; Jung, Y. *Nano Today* 2018, 19, 16–40.
- (20) Novoselov, K. S.; Fal'ko, V. I.; Colombo, L.; Gellert, P. R.; Schwab, M. G.; Kim, K. *Nature* 2012, 490, 192–200.
- (21) Hanakata, P. Z.; Qi, Z.; Campbell, D. K.; Park, H. S. *Nanoscale* 2016, 8 (1), 458–463.
- (22) Qi, Z.; Campbell, D. K.; Park, H. S. *Phys. Rev. B: Condens. Matter Mater. Phys.* 2014, 90 (24), 245437–245444.
- (23) Blees, M. K.; Barnard, A. W.; Rose, P. A.; Roberts, S. P.; McGill, K. L.; Huang, P. Y.; Ruyack, A. R.; Kevek, J. W.; Kobrin, B.; Muller, D. A.; McEuen, P. L. *Nature* 2015, 524, 204–213.
- (24) Choudhary, N.; Chung, H.-S.; Kim, J. H.; Noh, C.; Islam, M. A.; Oh, K. H.; Coffey, K.; Jung, Y.; Jung, Y. *Adv. Mater. Interfaces* 2018, 5 (14), 1800382–1800392.
- (25) Islam, M. A.; Kim, J. H.; Schropp, A.; Kalita, H.; Choudhary, N.; Weitzman, D.; Khondaker, S. I.; Oh, K. H.; Roy, T.; Chung, H.-S.; Jung, Y. *Nano Lett.* 2017, 17 (10), 6157–6165.
- (26) Choudhary, N.; Park, J.; Hwang, J. Y.; Chung, H.-S.; Dumas, K. H.; Khondaker, S. I.; Choi, W.; Jung, Y. *Sci. Rep.* 2016, 6, 25456–25463.
- (27) Choudhary, N.; Islam, M. R.; Kang, N.; Tetard, L.; Jung, Y.; Khondaker, S. I. *J. Phys.: Condens. Matter* 2016, 28 (36), 364002–364012.
- (28) Jung, Y.; Shen, J.; Liu, Y.; Woods, J. M.; Sun, Y.; Cha, J. J. *Nano Lett.* 2014, 14 (12), 6842–6849.
- (29) Kim, J. H.; Ko, T.-J.; Okogbue, E.; Han, S. S.; Shawkat, M. S.; Kaium, M. G.; Oh, K. H.; Chung, H.-S.; Jung, Y. *Sci. Rep.* 2019, 9 (1), 1641–1651.

- (30) Zheng, W.; Huang, W.; Gao, F.; Yang, H.; Dai, M.; Liu, G.; Yang, B.; Zhang, J.; Fu, Y. Q.; Chen, X.; Qiu, Y.; Jia, D.; Zhou, Y.; Hu, P. *Chem. Mater.* 2018, 30 (17), 6063–6070.
- (31) Yim, C.; Lee, K.; McEvoy, N.; O'Brien, M.; Riazimehr, S.; Berner, N. C.; Cullen, C. P.; Kotakoski, J.; Meyer, J. C.; Lemme, M. C.; Duesberg, G. S. *ACS Nano* 2016, 10 (10), 9550–9558.
- (32) Wagner, S.; Yim, C.; McEvoy, N.; Kataria, S.; Yokaribas, V.; Kuc, A.; Pindl, S.; Fritzen, C.-P.; Heine, T.; Duesberg, G. S.; Lemme, M. C. *Nano Lett.* 2018, 18 (6), 3738–3745.
- (33) Choudhury, I. A.; Shirley, S. *Opt. Laser Technol.* 2010, 42 (3), 503–508.
- (34) Yim, C.; Passi, V.; Lemme, M. C.; Duesberg, G. S.; Ó Coileáin, C.; Pallecchi, E.; Fadil, D.; McEvoy, N. *npj 2D Materials and Applications* 2018, 2 (1), 5–12.
- (35) Islam, M. A.; Church, J.; Han, C.; Chung, H.-S.; Ji, E.; Kim, J. H.; Choudhary, N.; Lee, G.-H.; Lee, W. H.; Jung, Y. *Sci. Rep.* 2017, 7, 14944–14954.
- (36) Wang, Z.; Zhang, L.; Duan, S.; Jiang, H.; Shen, J.; Li, C. *J. Mater. Chem. C* 2017, 5 (34), 8714–8722.
- (37) Naveau, A.; Monteil-Rivera, F.; Guillon, E.; Dumonceau, J. *Environ. Sci. Technol.* 2007, 41 (15), 5376–5382.
- (38) Zhao, Y.; Qiao, J.; Yu, Z.; Yu, P.; Xu, K.; Lau, S. P.; Zhou, W.; Liu, Z.; Wang, X.; Ji, W.; Chai, Y. *Adv. Mater.* 2017, 29 (5), 1604230–1604240.
- (39) Wang, Z.; Li, Q.; Besenbacher, F.; Dong, M. *Adv. Mater.* 2016, 28 (46), 10224–10229.
- (40) Zeng, L.-H.; Lin, S.-H.; Li, Z.-J.; Zhang, Z.-X.; Zhang, T.-F.; Xie, C.; Mak, C.-H.; Chai, Y.; Lau, S. P.; Luo, L.-B.; Tsang, Y. H. *Adv. Funct. Mater.* 2018,

28 (16), 1705970–1705981.

(41) Lin, S. H.; Liu, Y.; Hu, Z. X.; Lu, W.; Mak, C. H.; Zeng, L. H.; Zhao, J.; Li, Y. Y.; Yan, F.; Tsang, Y. H.; Zhang, X. M.; Lau, S. P. *Nano Energy* 2017, 42, 26–33.

(42) Ciarrocchi, A.; Avsar, A.; Ovchinnikov, D.; Kis, A. *Nat. Commun.* 2018, 9 (1), 919–925.

(43) Su, T.-Y.; Medina, H.; Chen, Y.-Z.; Wang, S.-W.; Lee, S.-S.; Shih, Y.-C.; Chen, C.-W.; Kuo, H.-C.; Chuang, F.-C.; Chueh, Y.-L. *Small* 2018, 14 (19), 1800032–1800042.

(44) Shyu, T. C.; Damasceno, P. F.; Dodd, P. M.; Lamoureux, A.; Xu, L.; Shlian, M.; Shtein, M.; Glotzer, S. C.; Kotov, N. A. *Nat. Mater.* 2015, 14, 785–791.

(45) Tang, Y.; Lin, G.; Yang, S.; Yi, Y. K.; Kamien, R. D.; Yin, J. *Adv. Mater.* 2017, 29 (10), 1604262–1604271.

(46) Han, S. S.; Kim, J. H.; Noh, C.; Kim, J. H.; Ji, E.; Kwon, J.; Yu, S. M.; Ko, T. J.; Okogbue, E.; Oh, K. H.; Chung, H. S.; Jung, Y.; Lee, G. H.; Jung, Y. *ACS Appl. Mater. Interfaces* 2019, 11 (14), 13598–13607.

4.2. Stretchable Electronic Heater of 2D PtTe₂ Layers

The contents of this section have been published in: Tae-Jun Ko, Sang Sub Han, Emmanuel Okogbue, Mashiyat Sumaiya Shawkat, Mengjing Wang, Jinwoo Ma, Tae-Sung Bae, Shihab Bin Hafiz, Dong-Kyun Ko, Hee-Suk Chung, Kyu Hwan Oh, Yeonwoong Jung “Wafer-scale 2D PtTe₂ layers-enabled Kirigami heaters with superior mechanical stretchability and electro-thermal responsiveness” Applied Materials Today 20 100718 (2020).

4.2.1. Introduction

2D Pt ditelluride (PtTe₂) layers are an emerging class of metallic vdW crystals possessing unusual band structure and topological transition as well as extremely high electrical conductivity, i.e., $\sim 10^6 - 10^7$ S/m.[1-3] Moreover, they exhibit high air- and thermal-stability, unlike the black phosphorus of comparable electrical conductivity, which suffers from significant oxidation-driven properties degradation.[4, 5] These combined attributes of high electrical conductivity and superior air/thermal stability coupled with their extremely small thickness project unprecedented opportunities that is difficult to achieve with any conventional 2D TMD layers or other metallic materials. Out of vastly projected applications, we particularly note their potential as an atomically thin “electrothermal material” which converts electric current into thermal energy. For decades, a large number of metallic materials with high electric-to-thermal conversion rates have been explored for a variety of electrothermal applications such as window defrosters/defoggers,[6, 7] thermotherapy pads,[8, 9] heating textiles,[10] soft actuator, [11] and smart drug delivery.[12] Recent advances in emerging technologies of various form factors, e.g., stretchable or fold-able heaters, have demanded “ultra-light” electrothermal materials in mechanically adaptable forms. A variety of low-

dimensional materials have been explored to overcome the intrinsic limitations (e.g., rigidity and bulkiness) of conventional electrothermal materials.[13] Earlier efforts have focused on combining one-dimensional (1D) conductive nanomaterials such as carbon nanotubes (CNTs) or silver nanowires (Ag NWs) with elastic and conjugated polymers[14-17] benefiting from their process simplicity. However, several drawbacks are noted in this approach; (1) It is difficult to achieve the high spatial homogeneity of electrothermal conversions on large areas as they occur by the percolation-driven transport of electrons/phonons owing to the intrinsic randomness of the way that the 1D nanomaterials are integrated. (2) Resulting composites are prone to thermally driven mechanical deformation owing to the thermal instability of polymer constituents combined with their uneven interfaces with the 1D nanomaterials. Accordingly, significant performance degradations are noted upon repeated heating.[18, 19] (3) It is challenging to reduce their thickness and maintain the high conductivity of 1D component-based composites at the same time, while the recent advances in wearable technologies have been driven toward incorporating thinner and more flexible/stretchable materials.[13]

In this study, we explore electrothermal properties of chemically grown 2D PtTe₂ layers and demonstrate their application for high-performance extremely stretchable wearable heaters. We grew wafer-scale 2D PtTe₂ multilayers via a chemical vapor deposition (CVD) tellurization of Pt thin films at a low temperature of 400 °C, which is compatible with some polymeric substrates. We characterized their electrical properties and identified intrinsically small sheet resistance down to 19.4 Ω/, significantly smaller than those of previously

developed any other 2D materials. By taking this combined advantage of low growth temperature and high electrical conductance, we developed 2D PtTe₂ layers-based stretchable and wearable heaters by directly growing them on strain-engineered polymeric substrates of Kirigami forms and evaluated their electrothermal performances. These 2D PtTe₂ layers-based heaters exhibited remarkably fast electric-to-thermal conversion rates even at low applied voltages (i.e., 26.6 °C/sec of the heating rate at 5 V). Moreover, these superior properties were identified to be strain-invariant with extremely high mechanical tolerance, benefiting from the judiciously-designed Kirigami patterns—i.e., persistent heat generation even after 1,000 times cyclic stretching. Overall, the electrothermal performances of these CVD-grown wafer-scale 2D PtTe₂ layers greatly surpass those of all other state-of-the-art 1D or 2D materials previously explored for such applications, including Ag NWs, graphene, and MXenes.

4.2.2. Experimental Method

4.2.2.1. 2D PtTe₂ Synthesis

Pt seed films of controlled thickness from 0.5 to 9 nm were deposited on two kinds of substrates, i.e., silicon dioxide (SiO₂)/Si wafers (300 nm oxide layer thickness) and polyimide (PI) sheets (50 μm thickness) by an electron beam evaporator (Thermionics VE-100) at a deposition rate of 0.15 Å/sec. The Pt-deposited substrates were placed at the center of the quartz tube inside a CVD thermal furnace (Blue M Mini-Mite, Lindberg). Tellurium (Te) powder (CAS No. 13494-80-9, 200 mesh, 99.8%, Sigma-Aldrich, Inc.) contained in an alumina boat was placed at the upstream side of the furnace. The quartz tube

containing the samples was evacuated to a basal pressure of < 20 mTorr, and argon (Ar) gas was subsequently supplied at a rate of 100 sccm to maintain the working pressure of 75 mTorr. Then, the furnace was heated up to $400\text{ }^{\circ}\text{C}$ in 50 min, and the temperature was maintained for an additional 50 min before its natural cool-down to ambient temperature. After sample preparation, the thicknesses of 2D PtTe₂ layers were measured using atomic force microscopy (AFM, NanoIR2, Anasys Instruments) with tapping mode at 0.3 Hz of the scan rate.

4.2.2.2. Crystal Structure Characterization

Aberration-corrected transmission electron microscopy (Cs- corrected TEM, ARM 200F, Jeol, USA) was utilized with 200 kV of an accelerating voltage. For the plane-view TEM observation, as- grown 2D PtTe₂ layers were detached from SiO₂/Si wafers by using a buffered oxide etchant, and they were subsequently transferred onto copper TEM grids. For the cross-sectional TEM observation, standard focused ion beam lift-out techniques were employed for sample preparation. Also, X-ray diffraction (XRD, PAN-alytical Empyrean) was carried out for revealing the crystal structure of 2D PtTe₂ layers on SiO₂/Si substrates with a copper X-ray source ($K_{\alpha 1}$, $\lambda = 1.5406\text{ }^{\circ}\text{A}$).

4.2.2.3. Raman and Electrical Characterization

Raman spectra of 2D PtTe₂ layers were acquired by inVia TM confocal Raman microscope (Renishaw, UK) at ambient condition. A laser source with 532 nm of wavelength was used for analysis, and the excitation power was set to 1 mW to minimize damage on the samples. The electrical properties of 2D PtTe₂ layers were characterized by current-voltage (I-V) measurements using a

semiconductor parameter analyzer (HP 4156 A, Hewlett-Packard, USA) connected to a home-built probe station. Sheet resistances of 2D PtTe₂ layers were obtained by a 4-point resistivity probe (SP4, Sig-natone, USA) connect to a source meter (Keithley 2400, Keithley Instruments, USA).

4.2.2.4. Heating performance Test

Joule heating performances of 2D PtTe₂ layers were evaluated by measuring their temperature change under an application of electrical bias. 2D PtTe₂ layers grown on PI substrates with a size of 1.5 × 1.5 cm² were prepared, followed by the deposition of gold (Au) electrodes (100 nm thickness), achieving the active heating zone of 1 × 1.5 cm² in a two-terminal configuration. A power supply (TP3005T Variable Linear DC Power Supply, Tekpower, USA) was used to apply DC voltage to the samples in the range of 1 to 10 V. The maximum temperature profiles of the electrically-biased samples were recorded by an infrared (IR) camera (FLIR C2, FLIR®Systems, Inc., USA) with 9 Hz, and the heating and cooling rates were calculated from the temperature profile per second.

4.2.2.5. Kirigami-pattern Fabrication and Finite Element Method

Kirigami patterns were engraved on PI substrates by a commercial mechanical cutter (Cricut Explore Air 2, Cricut, Inc., USA). Then, 2D PtTe₂ layers were grown on the patterned substrates by the CVD tellurization method, as described above. Deformation behaviors of the Kirigami patterns were analyzed by the finite element method (FEM) simulation using commercial software (Abaqus 6.13). S4R type element with an approximate mesh size of 50 μm was used.

4.2.3. Results and Discussion

4.2.3.1. 2D PtTe₂ Layer Growth

2D PtTe₂ layers were grown by the CVD tellurization of Pt- deposited growth substrates following the growth recipe presented in the *Experimental Method* Section (Figure 4. 6a). Briefly, Pt-deposited substrates are placed in the furnace center zone and vaporized Te is supplied from the upstream side of the furnace. The CVD tellurization reaction occurs at 400 °C at which the vaporized Te lowers the melting temperature of Pt by eutectic formation, enabling the growth of 2D PtTe₂ layers.[20, 21] This CVD tellurization method can grow wafer-scale 2D PtTe₂ layers of controlled thickness, as shown in Figure 4. 6b, which shows a sample of 2D PtTe₂ layers on a SiO₂/Si wafer on an area of ~12 cm². The thickness of as grown 2D PtTe₂ layers was measured with the AFM characterization collaborated with cross-sectional TEM imaging. The plots in Figure 4.6c correlate the thickness of initially deposited-Pt films vs. resulting 2D PtTe₂ layers, revealing high linearity indicating ~5 times thickness increase after the CVD tellurization. For convenience, 2D PtTe₂ samples are labeled by the thickness of Pt films; e.g., Pt PtTe₂ - 1nm denotes the sample prepared with Pt films of 1 nm thickness. The surface roughness of as-grown 2D PtTe₂ layers was also determined using AFM characterization, confirming very small roughness values of ~0.7 and ~1.89 nm, respectively. Raman spectroscopy was used to investigate the spatial and chemical uniformity of the sample shown in Figure 4. 6b, where the color-marked four different spots were inspected. Two characteristic Raman peaks were observed, as presented in Figure 4. 6d, i.e., E_g peak at 117 cm⁻¹ and A_{1g} peak at 159 cm⁻¹ corresponding to the in-plane and

out-of-plane vibration modes of 2D P_2 , respectively. The results are consistent with previous studies on single-crystal 2D $PtTe_2$ layers of much smaller dimensions (e.g., typically, a few μm^2). [1, 2, 22] Also, each spectrum exhibits nearly identical intensity ratio of E_g/A_{1g} and peak positions irrespective of the different probe locations, suggesting the high uniformity of the sample. Energy-dispersive X-ray spectroscopy (EDS) in TEM was employed to analyze the spatial distribution of constituting elements and quantify their atomic concentrations. Figure 4. 6e presents the cross-sectional EDS elemental mapping images of a $PtTe_2$ -1.5nm sample, confirming the highly uniform distribution of both Pt and Te. Figure 4. 6f shows the corresponding EDS spectrum, which identifies the atomic concentration of Pt:Te = 32.8:67.2 (i.e., 1:2.04), confirming the growth of stoichiometric 2D PtT_2 layers.

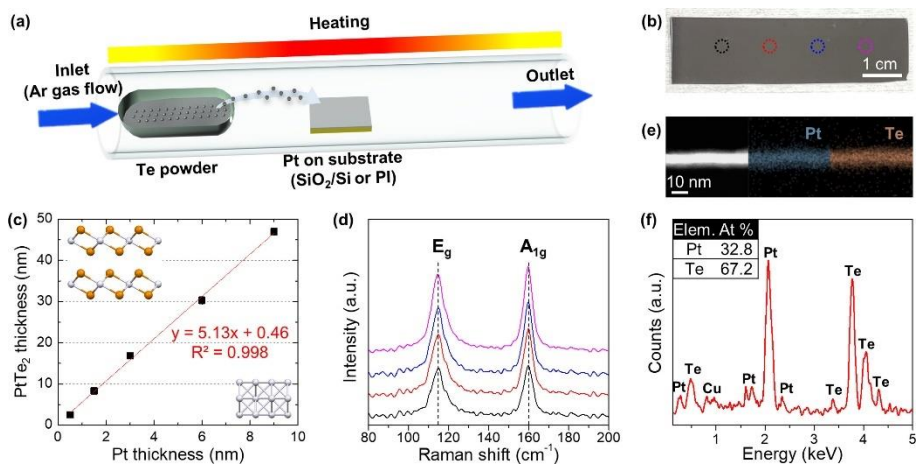


Figure 4. 6. (a) Schematic of CVD growth of wafer-scale 2D PtTe₂ layers. (b) A photo of 2D PtTe₂ layers grown on a SiO₂/Si wafer on a size of 12 cm². (c) Thickness relation of initial Pt films vs. resulting 2D PtTe₂ layers. (d) Raman spectra corresponding to the four spots marked on the sample in (b). (e) Cross-sectional TEM/EDS mapping images showing the spatial distribution of Pt and Te within 2D PtTe₂ layers. (f) EDS profile quantifying the atomic ratio of Pt and Te corresponding to (e).

4.2.3.2. Electrical and electrothermal properties of 2D PtTe₂ layer

Before investigating the electrothermal performances of 2D PtTe₂ layers in mechanically stretchable forms, we first studied their electrical conductivities. Figure 4. 7a presents the thickness-dependent sheet resistance (R_s) of 2D PtTe₂ layers obtained with Pt films of varying thicknesses. R_s values steadily decrease with increasing Pt thickness, and the PtTe₂-9 nm sample exhibits a value as low as 19.4 Ω /. This value is quite lower than those of other electrothermal nanomaterials previously developed for stretchable heaters; e.g., 43 Ω / for doped multilayer graphene, and 215 Ω / for MXene based composites.[20] Such low R_s values are essential for efficient electrothermal energy conversion as the Joule-heating efficiency is expressed by $P = V^2/R_s$, where P is power and V is voltage. Moreover, the low R_s values should be maintained even in a wide range of high temperature under actual operating conditions, which is essential for reliable and practical electrothermal device applications. Figure 4. 7b shows temperature-dependent R_s values normalized to that obtained at room temperature ($R_{s,RT}$), revealing that they are nearly unchanged ($< 0.1\%$ degradation) even up to 225 °C. Unlike most of the metal-based heaters that suffer from resistivity degradation with increasing temperature, 2D PtTe₂ layers exhibit very stable temperature-invariant electrical properties.[23] These combined attributes of intrinsically superior electrical conductivity and thermal stability coupled with the low CVD growth temperature (i.e., 400 °C) of 2D PtTe₂ layers make them a promising candidate for high-performance mechanically stretchable heaters.

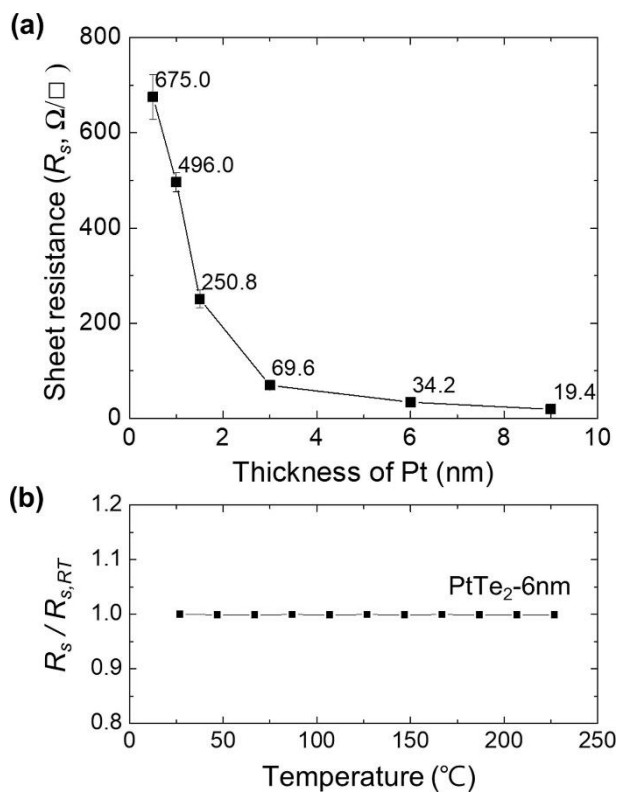


Figure 4. 7. (a) Sheet resistances of 2D PtTe₂ layers prepared with Pt films of various thicknesses. (b) The temperature-dependent ratio of sheet resistance (R_s) normalized to the room-temperature sheet resistance ($R_{s,RT}$) obtained from PtTe₂-6nm sample.

To pursue this projected opportunity, we first demonstrated the direct growth of 2D PtTe₂ layers on mechanically flexible PI substrates. By applying the identical CVD recipe adopted for SiO₂/Si as growth substrates, we grew 2D PtTe₂ layers on PI substrates which are highly stable even above 400 °C.[24] XPS characterization confirmed that the Pt 4f and Te 3d core-energy spectral peaks and positions are nearly identical for 2D PtTe₂ layers grown on both PI and SiO₂/Si substrates, confirming the generality of our CVD method. Figure 4. 8a shows optical images of as-grown 2D PtTe₂ layers on PI substrates prepared with Pt films of varying thickness, revealing decreasing optical transparency with increasing thickness. Electrothermal properties of these samples were characterized by identifying their temperature variation upon an application of electrical biasing, determined by IR imaging. Figure 4. 8b presents a diagram that correlates the maximum temperature (T_{\max}) of 2D PtTe₂/PI samples prepared with varying Pt thickness obtained at three different applied voltages. T_{\max} steadily increases with increasing thicknesses due to lower sheet resistance (Figure 4. 7a) as predicted by the Joule-heating efficiency equation ($P = V^2/R_s$). Indeed, we note that the electrically driven temperature change of these samples well follows the Joule-heating efficiency equation irrespective of their thickness. Particularly, we observe that these 2D PtTe₂/PI heaters exhibit significantly high temperature even at very low operation voltages, e.g., ~170 °C for PtTe₂- 9 nm at 7 V, much lower than the voltage regarded as non-hazardous according to International Electrotechnical Commission (IEC 60950-1).[25] Figure 4. 8c shows the time-dependent variation of T_{\max} for 2D PtTe₂ layers prepared with varying Pt thickness

operated at a constant voltage of 5 V for 30 sec. Upon the onset/termination of the voltage denoted by the first/second dashed lines, respectively, T_{\max} rapidly increases/decreases within 10 secs for all samples. Figure 4. 8d presents the first derivatives of the time- temperature plots in Figure 4. 8c, clarifying the heating/cooling kinetics of the 2D PtTe₂ layers more precisely. The PtTe₂-9nm sample exhibits the heating/cooling rate of 26.6 °C/sec and 24.2 °C/sec under 5 V, respectively, which allows the heater to reach T_{\max} much faster (5 sec) than that obtained with other nanomaterials previously explored for heater applications; e.g., nano graphite,[26] or reduced graphene oxide (rGO),[27] as summarized in Table 4. 1. These heating/cooling rates can be further increased to 46.8 °C/sec and 36.6 °C/sec by applying a higher voltage of 7 V, respectively, achieving significantly faster thermal responses. Moreover, we also evaluated the electrothermal endurance of these samples by applying/terminating a constant voltage in a cyclic manner and identifying resulting temperature variation. The plot of cycle number vs. temperature in Figure 4. 8e presents the cyclic heating/cooling of an identical sample (i.e., 2D PtTe₂-6nm) obtained under a cyclic application/termination of 4 V for 50 times. Considering the fast heating/cooling rate of the sample for achieving T_{\max} /ambient temperature, a fixed interval of 10 sec was assigned for the voltage application/termination in each cycle. It is noteworthy that the average T_{\max} of 81.9 °C is well retained throughout the entire cyclic period accompanying a very small deviation of ~1.0 °C, confirming excellent electrothermal endurance essential for practical applications. Fig. 4. 9f presents IR images of the same sample in Figure 4. 8e, obtained at specific periods of 1st, 25th, and 50thcycles, showing the stable

operation with multiple cycles. Furthermore, in a way to assess the technological potential of 2D PtTe₂/PI materials as a portable heater for practical applications, we characterized their electrothermal performances driven by solar energy. Figure 4. 8g shows a representative image (left) of a 2D PtTe₂-6nm sample connected to a portable solar panel and its corresponding IR images without (mid) and with (right) sunlight illumination. Figure 4. 8h presents the variation of temperature for the samples of various thickness operated at ~4 V driven by solar energy. (Air mass: ~1.3, Ambient temperature ~30 °C) It is noteworthy the 2D PtTe₂-6nm sample reaches T_{max} of 53.0 °C in its ON state (with illumination), which is > ~25 °C increase compared to its OFF state (without illumination). All these results comprehensively indicate that 2D PtTe₂ layers possess a large set of electrothermal properties essential for high-performance heating devices; i.e., low operational voltage, rapid responsiveness as well as high thermal stability and endurance.

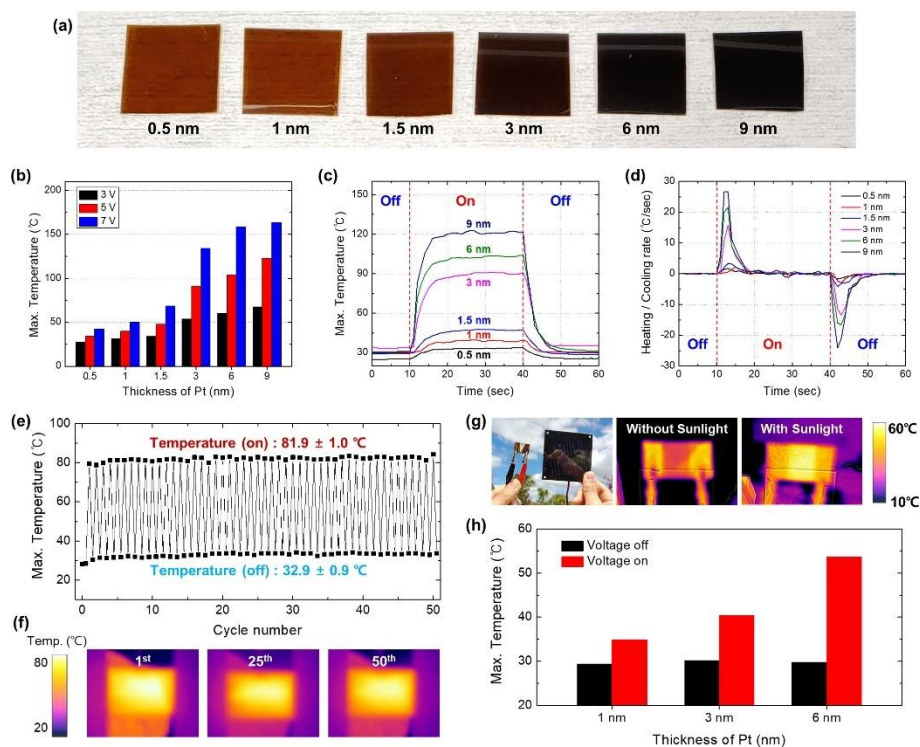


Figure 4. 8. (a) Photos of 2D PtTe₂ layers-grown flexible PI substrates prepared with Pt films of various thicknesses. (b) The maximum temperature of 2D PtTe₂/PI samples prepared with various Pt thickness achieved at biases of 3, 5, and 7 V. (c) Time-dependent temperature fall/rise of the same samples in (b) obtained at 5 V. (d) Determination of the heating/cooling rate corresponding to (c). (e) Temperature variation obtained from a 2D PtTe₂-6nm/PI sample during the cyclic heating/cooling of 50 times at 4 V. (f) Representative IR images of the sample in (e) at three different cycle numbers. (g) Demonstration of the solar energy-driven operation of 2D PtTe₂/PI heaters. (h) Temperature variations achieved with 2D PtTe₂/PI heaters of various thickness driven by solar energy.

Material	T _{max} (°C)/Voltage (V)	Time required for T _{max}	Flexibility	Ref.
Cu/PI	95 °C/3.8 V	2 sec	Bendable, Stretchable (800%)	[39]
Liquid-metal/PDMS	90 °C/3.5 V	> 180 sec	Stretchable (100%)	[38]
Ag dendrites/PET	135 °C/4 V	35 sec	Bendable	[42]
Graphite/PVC	35 °C/5 V	30 sec	Bendable	[43]
Graphite nanoplatelet/PI	50 °C/6 V	– 100 sec	Bendable	[33]
rGO/PI	86 °C/9 V	– 10 sec	Bendable	[34]
Ag + rGO/PI	70 °C/9 V	– 5 sec	Bendable	[26]
Ag NW + SWCNT/PDMS	87 °C/5 V	– 120 sec	Bendable, Stretchable (–50%)	[12]
MXene/PET	35 °C/5 V	– 40 sec	Bendable	[27]
2D	120 °C/5 V	5 sec	Bendable	This
PtTe ₂ /PI	58 °C/5 V	5 sec	Stretchable (–130%)	work

Table 4. 1. Comparison of the electrothermal performance and the flexibility with the recently developed nanomaterial-based wear-able heaters.

4.2.3.3. Flexibility of 2D PtTe₂ Layer on PI Substrate

We experimentally evaluated the electrothermal performance of the sample by measuring its temperature and resistance changes under outward bending, circumventing any noticeable degradation caused by crack generation.[28] Figure 4. 9a presents IR images of the sample subjected to the mechanical deformation of controlled bending angle from 0° to 180°, which are viewed in a top-to-bottom orientation. It is noted that the sample does not exhibit any significant performance degradation manifested by temperature reduction even under the bending up to 180°, measured with a bending radius of 2 mm at 3 V. The inset in Figure 4. 9b presents the side-view schematic illustration of the sample corresponding to Figure 4. 9a, defining measurement parameters of bending angle (α) and radius (r). Figure 4. 9b presents the change of T_{\max} (top panel) and normalized resistance, R/R_0 , where R_0 denotes the resistance at unbent state (bottom panel) as a function of bending angle (α) and radius (r). It is rational to assume that smaller bending radii and larger bending angles would lead to more significant deformation in 2D PtTe₂ layers as their outward surface will experience high mechanical tension. Indeed, the plots in Figure 4. 9b confirms a significant increase in R/R_0 and decrease in T_{\max} with increasing bending angles, noticeably observed with the sample with a small bending radius of 1 mm (2.3% of tensile strain). However, with a larger bending radius of 5 mm (0.5% of tensile strain), such a significant change is not observed in both R/R_0 and T_{\max} even under deformation up to the bending angle of 180°. This observation confirms that 2D PtTe₂ layers do not undergo any significant structural degradation even under a large extent of mechanical deformation,

preserving their intrinsic property advantages. With consideration of the realistic deformation range in human body joints, the results are highly encouraging for the application of 2D PtTe₂ layers in wearable and attachable heater devices for personalized applications.

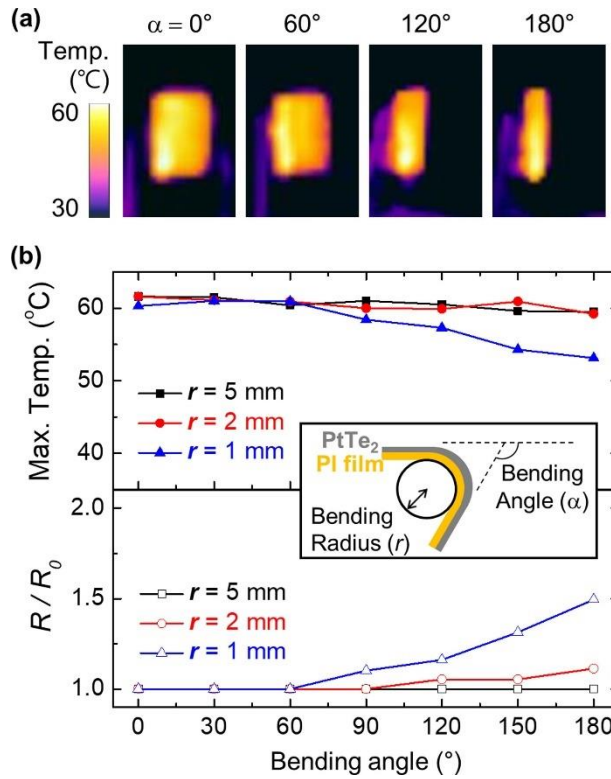


Figure 4. 9. (a) IR images of a PtTe₂-6nm/PI sample at various bending angles obtained with the bending radius of 2 mm at 3 V. (b) Variation of the maximum temperature and relative resistance for the same sample in (a) as a function of bending angle and bending radius.

4.2.3.4. Kirigami-patterned stretchable heater based on 2D PtTe₂

Encouraged by these intrinsically superior electrothermal properties and deformation-insensitive structural integrity inherent to 2D PtTe₂ layers, we set on exploring them for skin-attachable flexible heaters. To this end, it is particularly essential to configure the 2D PtTe₂/PI heaters in mechanically stretchable forms well to suit the demands of complex human body motions. Notably, recent studies suggested that stretchability up to at least 70% is demanded to accommodate maximum human body linear elongation into wearable device technologies.[8, 29] Various strain engineering schemes employing judiciously designed patterns and structures have been explored to achieve strain-invariant properties in stretchable devices, which includes wavy, [30] island-interconnect,[31] and Kirigami geometries. [32, 33, 34] Adopting these pattern-based strategies to the wearable heater application, we developed strain-invariant 2D PtTe₂/PI heaters by employing the concept of Kirigami pattern designing and evaluated their electrothermal performances under varying stretch levels. Kirigami patterning approaches inspired the ancient paper-cutting arts have been employed to efficiently relieve externally applied tensile stress within 2D objects by converting it to 3D torsional stress. We applied same process of Kirigami patterning which we used for 2000% stretchable PtSe₂/PI device to the stretchable PtTe₂/PI electronic heater. We experimentally demonstrated electrothermal performances of 2D PtTe₂/PI Kirigami heaters under varying tensile stretch conditions and compared them to the FEM predictions. The insets in Figure 4. 10a show the representative IR images of a Kirigami-patterned 2D PtTe₂-9nm/PI sample (initial size; 18 ×12

mm²) in a range of 3 to 10 V under varying stretch levels. The plots in Figure 4. 10a show that the temperature of the corresponding Kirigami sample increases with increasing voltage, which is well retained up to 110 % strain at each applied voltage. For in-stance, T_{\max} of ~ 115 °C achieved by 10 V remains nearly constant up to $\sim 130\%$ of strain after which it drastically drops to ~ 44 °C as a result of mechanical fracture at the cut edges of the Kirigami pattern. Voltage-driven temperature variations of the same sample were also identified, showing a high heating rate of 22.4 °C/sec was observed to reach T_{\max} of ~ 119.3 °C at 10 V. Next, we examined the durability and robustness of this 2D PtTe₂/PI Kirigami heater by repeatedly applying/releasing a fixed tensile stain in a cyclic manner. Figure 4. 10b shows the plots of T_{\max} and R/R_0 obtained from the same sample during the course of 1,000 cycles at 70% strain under 7 V. It is observed that T_{\max} varies within ± 1 °C and R/R_0 slightly increases by less than 2% after the 1,000 times cyclic stretching, indicating its outstanding fatigue tolerance.

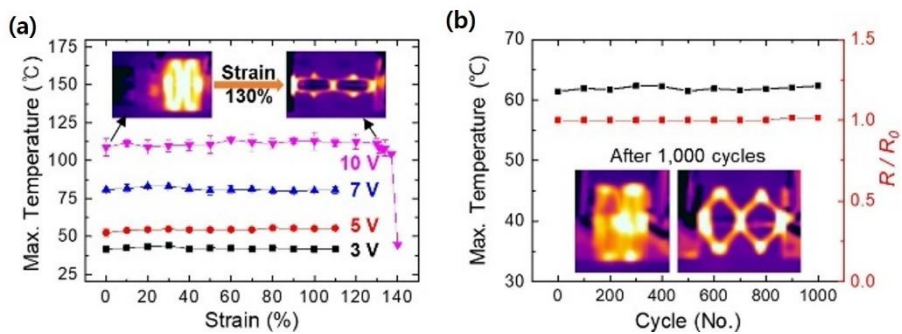


Figure 4. 10. (a) IR images of a 2D PtTe₂/PI Kirigami heater (insets) and the corresponding plots of T_{max} vs. strain rate. (b) Variations of T_{max} and R/R_0 obtained from the same sample in (a) during the cyclic stretch of 1,000 times with 70% of strain.

Lastly, we demonstrated the applicability of our 2D PtTe₂/PI Kirigami devices for skin-attachable wearable heaters. Figure 4. 11a shows the optical images (top panel) and the corresponding IR images (bottom panel) of a large 2D PtTe₂/PI Kirigami heater (size: 36×24 mm²) attached to a wrist undergoing realized and stretched motions. The images confirm the excellent attachability and stretchability of the Kirigami heater, which well performs even integrated on the highly curved surface in dynamic motions of the human body. Figure 4. 11b compares the IR images of the wrist with and without the Kirigami heater operated at 10 V, revealing a temperature difference of > 10 °C.

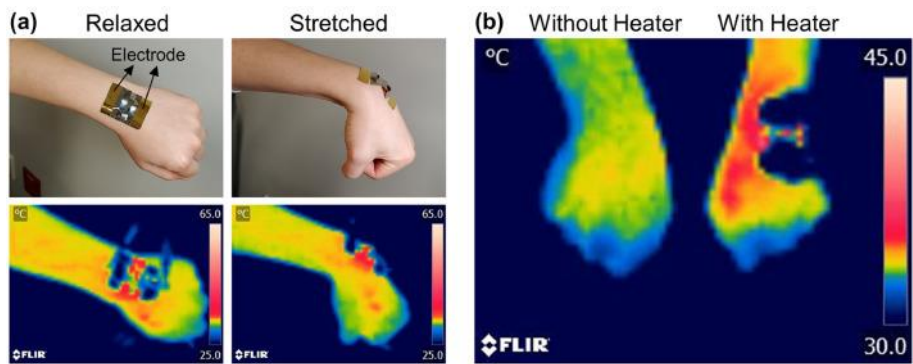


Figure 4. 11. (a) Demonstration of skin-attachable 2D PTe₂ layers-based Kirigami heaters in accordance with the mechanical motions of a human wrist. The IR images on the bottom panels show temperature distribution on the wrist when the heater was electrically biased. (b) IR images showing the temperature distribution of the wrists with (right) and without (left) attaching the heater.

4.2.4. Conclusion

In summary, we explored wafer-scale CVD-grown 2D PtTe₂ layers for high-performance mechanically deformable heaters by employing their intrinsically superior mechanical, electrical, and thermal properties. CVD-2D PtTe₂ layers directly grown on large PI substrates at 400 °C exhibited excellent Joule heating efficiency – i.e., the fast rise of high temperature at a given voltage – superior to those of previously explored all other state-of-the-art nanomaterials. Furthermore, we prepared for them in the form of judiciously-designed Kirigami patterns and demonstrated high-performance skin-attachable heaters, which exhibited strain invariant electrothermal properties and large stretchability. This study confirms the high promise of these emerging metallic 2D layered materials for a wide range of futuristic stretchable device technologies.

4.2.5. Reference

- (1) L. Fu., et al. Highly organized epitaxy of dirac-semimetallic PtTe₂ crystals with extra-high conductivity and visible surface plasmons at edges, *ACS Nano* 12 (2018) 9405–9411
- (2) S. Hao., et al. Low-temperature eutectic synthesis of PtTe₂ with weak antilocalization and controlled layer thinning, *Adv. Funct. Mater.* 28 (2018) 1803746
- (3) M. Wang., et al. Wafer-scale growth of 2D PtTe₂ with layer orientation tunable high electrical conductivity and superior hydrophobicity, *ACS Appl. Mater. Interfaces* 12 (2020) 10839–10851
- (4) A. Favron., et al. Photooxidation and quantum confinement effects in exfoliated black phosphorus, *Nat. Mater.* 14 (2015) 826–832

- (5) J.O. Island., et al. Environmental instability of few-layer black phosphorus, *2D Mater.* 2 (2015) 011002
- (6) L. Tan., et al. Direct growth of ultrafast transparent single-layer graphene defoggers, *Small* 11 (2015) 1840–1846
- (7) E. Okogbue., et al. Wafer-scale 2D PtTe₂ layers for high-efficiency mechanically flexible electro-thermal smart window applications, *Nanoscale* (2020)
- (8) H. Kim., et al. Highly stretchable and wearable thermotherapy pad with micropatterned thermochromic display based on Ag nanowire–single-walled carbon nanotube composite, *Adv. Funct. Mater.* 29 (2019) 1901061
- (9) Y. Guo., et al. Ultrathin, washable, and large-area graphene papers for personal thermal management, *Small* 13 (2017) 1702645
- (10) J. Ahn., et al. Printed fabric heater based on Ag nanowire/Carbon nanotube composites, *Nanotechnology* 30 (2019) 455707
- (11) S. Yao., et al. Soft electrothermal actuators using silver nanowire heaters, *Nanoscale* 9 (2017) 3797–3805
- (12) P. Mostafalu., et al. Smart bandage for monitoring and treatment of chronic wounds, *Small* 14 (2018) 1703509
- (13) T.-J. Ko., et al. Large-area 2D TMD layers for mechanically reconfigurable electronic devices, *J. Phys. D: Appl. Phys.* 53 (2020) 313002
- (14) S. Hong., et al. Highly stretchable and transparent metal nanowire heater for wearable electronics applications, *Adv. Mater.* 27 (2015) 4744–4751
- (15) P. Lee., et al. Highly stretchable or transparent conductor fabrication by a hierarchical multiscale hybrid nanocomposite, *Adv. Funct. Mater.* 24 (2014) 5671–5678
- (16) P. Lee., et al. Highly Stretchable and highly conductive metal electrode by very long metal nanowire percolation network, *Adv. Mater.* 24 (2012) 3326–3332

- (17) S.-P. Chen, Y.-C. Liao, Highly stretchable and conductive silver nanowire thin films formed by soldering nano-mesh junctions, *Phys. Chem. Chem. Phys.* 16 (2014) 19856–19860
- (18) K. Chu., et al. Study of electric heating effects on carbon nanotube polymer composites, *Org. Electron.* 15 (2014) 2734–2741
- (19) H.H. Khaligh., et al. The joule heating problem in silver nanowire transparent electrodes, *Nanotechnology* 28 (2017) 425703
- (20) Y. Gong., et al. Vertical and In-Plane heterostructures from WS₂/MoS₂ monolayers, *Nat. Mater.* 13 (2014) 1135–1142
- (21) Y. Gong., et al. Tellurium-assisted low- temperature synthesis of MoS₂ and WS₂ monolayers, *ACS Nano* 9 (2015) 11658–11666
- (22) H. Ma., et al. Thickness-tunable synthesis of ultrathin type-II dirac-semimetal PtTe₂ single crystals and their thickness-dependent electronic properties, *Nano Lett.* 18 (2018) 3523–3529
- (23) D. Jung., et al. Transparent film heaters using multi-walled carbon nanotube sheets, *Sens. Actuators, A* 199 (2013) 176–180
- (24) S.S. Han., et al. Horizontal-to-vertical transition of 2D layer orientation in low-temperature chemical vapor deposition-grown PtSe₂ and its influences on electrical properties and device applications, *ACS Appl. Mater. Interfaces* 11 (2019) 13598–13607
- (25) D. Gies, Human Body impedance model at radio frequencies, 2016 IEEE Symposium on Product Compliance Engineering (ISPCE), (2016) 1-6.
- (26) K.-Y. Shin., et al. High electrothermal performance of expanded graphite nanoplatelet-based patch heater, *J. Mater. Chem.* 22 (2012) 23404–23410
- (27) T.-Y. Zhang., et al. A super flexible and custom-shaped graphene heater, *Nanoscale* 9 (2017) 14357–14363
- (28) H. Gleskova, S. Wagner, Z. Suo, A Si:H thin film transistors after very high strain, *J. Non Cryst. Solids* 266-269 (20 0 0) 1320–1324

- (29) A. NíAnnaidh., et al. Characterization of the anisotropic mechanical properties of excised human skin, *J. Mech. Behav. Biomed. Mater.* 5 (2012)
- (30) Y. Wang., et al. Printable liquid-metal at PDMS stretchable heater with high stretchability and dynamic stability for wearable thermotherapy, *Adv. Mater. Technol.* 4 (2019) 1800435
- (31) A.M. Hussain., et al. Ultra-stretchable and flexible copper interconnect-based smart patch for adaptive thermotherapy, *Adv. Healthcare Mater.* 4 (2015) 665–673
- (32) E. Okogbue., et al. Multifunctional two-dimensional PtSe₂ layer kirigami conductors with 2000% stretchability and metallic-to-semiconducting tunability, *Nano Lett.* 19 (2019) 7598–7607
- (33) N.S. Jang., et al. Simple approach to high-performance stretchable heaters based on kirigami patterning of conductive paper for wearable thermotherapy applications, *ACS Appl. Mater. Interfaces* 9 (2017) 19612–19621
- (34) P. Won., et al. Stretchable and transparent Kirigami conductor of nanowire percolation network for electronic skin applications, *Nano Lett.* 19 (2019) 6087–6096

4.3. Stretchable High-Performance Gas Sensor

The contents of this section have been published in: Md Ashrafur Islam, Hao Li, Seokjin Moon, Sang Sub Han, Hee-Suk Chung, Jinwoo Ma, Changhyeon Yoo, Tae-Jun Ko, Kyu Hwan Oh, YounJoon Jung, and Yeonwoong Jung “Vertically Aligned 2D MoS₂ Layers with Strain-Engineered Serpentine Patterns for High-Performance Stretchable Gas Sensors: Experimental and Theoretical Demonstration” ACS Appl. Mater. Interfaces 12, 47, 53174–53183 (2020).*

4.3.1. Introduction

Recently, considerable efforts have been devoted to 2D transition metal dichalcogenide (TMD) layers in exploiting their intrinsic advantages of chemical versatility and preparation simplicity compared to graphene and its derivatives, which generally demand additional burdens of surface functionalizations for improved sensitivity.[1, 2, 3] Particularly, 2D molybdenum disulfide (MoS₂) layers garnered significant interests owing to their unique structural tunability enabling two distinct layer orientations, i.e., horizontally vs vertically aligned layers.[4, 5, 6–15] Prior investigations of their gas sensing potential primarily focused on utilizing horizontally aligned layers commonly obtained via chemical exfoliation or chemical vapor deposition (CVD) process.[16, 17] Extensive studies demonstrated their intrinsic sensing capability for various gas species, particularly NO₂, which prompts grievous environmental burdens and respiratory ailments at high concentration.[18, 19] For instance, Kumar et al. employed CVD-grown horizontally aligned 2D MoS₂ multilayers and demonstrated their application of ultraviolet (UV) illumination-enhanced NO₂ gas sensing at room temperature.[2] Guo et al. developed horizontally aligned monolayer 2D MoS₂-based flexible devices for

NO₂ gas sensing and demonstrated enhanced sensitivity by tuning their Schottky barrier heights through photogating and piezo-phototronic effects.[20] Although the devices exhibited fairly high sensitivity promoted by a highintensity light-emitting diode (LED) illumination, their lateral stretchability was limited to be 0.67%. Cho et al. explored vertically aligned (VA)-2D MoS₂ layers for nonflexible chemiresistors and experimentally demonstrated NO₂ gas sensing.[17] They also employed density functional theory (DFT) calculations and verified a fivefold higher sensitivity of VA-2D MoS₂ layers compared to their horizontally aligned counterparts. Another experimental study reported that interconnected VA-2D MoS₂ nanoflakes presented a doubled sensitivity of ~ 48% over horizontally aligned layers under 50 ppm NO₂ at room temperature.[21] Despite these efforts, there exist no experimental demonstrations of VA-2D MoS₂ layer enabled NO₂ gas sensors congruently accompanying high electrical sensitivity as well as large mechanical stretchability (e.g., >30%). Indeed, the lateral stretchability of the above discussed current approaches is still far below the theoretically predicted in-plane strain limit of 2D MoS₂ layers,[4] severely limiting their potential for high-performance gas sensors with multifunctionalities.

In this study, we report a VA-2D MoS₂ layer-based multifunctional gas sensor, which can electrically detect NO₂ gas with high sensitivity while laterally expanding and shrinking. We directly integrated large-area (>cm²) CVD-grown VA-2D MoS₂ layers onto mechanically deformable substrates and created “serpentine” patterns capable of accommodating a large degree of tensile strain. This VA-2D MoS₂ layer-based sensor reliably detected NO₂ gas

in a range of 5–30 ppm achieving a high sensitivity of ~ 160 – 380% even without incorporating additional sensitivity enhancement methods. Furthermore, they were demonstrated to reversibly stretch up to $\sim 40\%$ without significantly compromising intrinsic high sensitivity, much superior to previously explored 2D MoS₂ layer-based stretchable sensors.

4.3.2. Experimental Method

4.3.2.1. CVD Growth of VA-2D MoS₂ Layers

An ultrahigh purity (99.99%) Mo thin film was deposited (typical thickness >5 nm) onto a SiO₂/Si substrate via an electron beam evaporator (Thermionics VE-100) at a deposition rate of 0.1 \AA/s . The Mo-deposited substrate was placed at the central heating zone of a quartz tube furnace (Lindberg), which contains S powder (99.5%, Sigma-Aldrich; 100 mg) at the upstream side. The furnace was pumped down to a 1 mTorr base pressure followed by heating to $650 \text{ }^\circ\text{C}$ at a ramping rate of $43 \text{ }^\circ\text{C/min}$. Ultrahigh purity Ar gas (flow rate: 100 SCCM) was supplied throughout the entire CVD reaction, which was retained for 30 minutes followed by natural cooling to room temperature.

4.3.2.2. VA-2D MoS₂ Layer Transfer and Integration Process

A thin layer of polymers was deposited onto an as-grown VA-2D MoS₂ layer/SiO₂/Si substrate followed by curing at room temperature. The prepared sample was immersed in water to weaken the binding of VA-2D MoS₂ layers against the SiO₂ surface followed by a subsequent manual peeling. The serpentine pattern was formed by cutting the sample using a mechanical cutter plotter.

4.3.2.3. AFM, UV–Vis, Raman, XPS, and TEM Characterizations

The surface topography of VA-2D MoS₂ layers was characterized via an atomic force microscope (Anasys Instruments nanoIR2) and their optical transmittance was measured by UV–vis spectroscopy (Agilent Cary 300) in the wavelength range of 200–800 nm. Raman spectroscopy characterization was performed using a Micro-Raman Spectrometer (Renishaw RM 1000B) with a laser wavelength of 514 nm and a spot size of 1 μm. The chemical bonding of VA-2D MoS₂ layers was identified by XPS (Physical Electronics 5400 ESCA). TEM characterization was performed with a probe-corrected TEM (ARM200F, JEOL) operating at 200 kV.

4.3.2.4. Device Fabrication and Electrical/Optical Characterization

Au IDEs (50 nm thickness) were deposited onto serpentine-patterned VA-2D MoS₂ layers/polymer substrates using a polyamide shadow mask. I–V characteristics of the sensors were recorded with a semiconductor parameter analyzer (HP 4156A) connected to a homebuilt probe station. They were connected with alligator clips and were introduced to tensile stretching using a homebuilt linear translation stage. The photo-response characterization was performed while the device was globally illuminated with a white LED source (intensity: 20 W/m²).

4.3.2.5. Gas Sensing Characterization

The real-time gas sensing measurements were performed inside a sealed acrylic vacuum chamber (Sanatron LLC.) equipped with electrical feed throughs and gas inlets/outlets. NO₂ gas of controlled concentration was injected into the chamber by reacting nitric acid (HNO₃) with copper (Cu)

pallets using the known reaction mechanism,[22] i.e., $4 \text{HNO}_3(\text{l}) + \text{Cu}(\text{s}) \Rightarrow \text{Cu}(\text{NO}_3)_2(\text{s and aq}) + 2 \text{NO}_2(\text{g}) + 2 \text{H}_2\text{O}(\text{l})$. The molar mass of HNO_3 , NO_2 , and Cu is 63.012, 46.006, and 63.55 g/m, respectively. The volume of the gas sensing chamber is 7125 cm^3 (25 cm length \times 19 cm width \times 15 cm height). From the above equation, HNO_3 0.195 g/m reacts with Cu of 0.04921 g/m, yielding NO_2 of 0.07125 g/m, which corresponds to 10 ppm. Similarly, HNO_3 of 0.095 g/m reacts with Cu of 0.0246 gm, producing $\text{NO}_2 = 5$ ppm, and so on. The concentration of the generated NO_2 gas was also monitored using a commercial NO_2 gas sensor (DGS Spec Sensor, Part #DGS-NO2 968-043) to ensure measurement precision. Once the gas sensing measurement was completed, the chamber was degassed with nitrogen gas.

4.3.2.6. FEM Simulation and DFT Calculation

The deformation behavior of the serpentine pattern was analyzed by the FEM simulation using a commercial software (Abaqus 6.13) using the C3D8R type element with a mesh size of ~ 5 mm. To simulate the out-of-plane rotation, buckling and post buckling modeling with imperfection were utilized.

DFT calculations were performed with the Vienna ab initio simulation package (VASP). We constructed a conventional slab-vacuum-slab model for 2D MoS_2 layers where the vacuum distance (along the c- and a-axes in the basal plane and VA-2D MoS_2 , respectively) is set to be larger than 20 \AA to avoid artificial interactions among periodic images. Periodic boundary conditions were implemented with the plane-wave basis set,[23] which adopts projector-augmented wave (PAW) pseudo-potentials.[24] The generalized gradient approximation (GGA)-based Perdew–Burke–Ernzerhof (PBE)68 functional

was adopted to describe the exchange–correlation functional of DFT calculations, corrected by the zero-damping DFT-3 method of Grimme[25] for better description of vdW-dispersion interaction. Ion positions were updated based on the conjugate gradient method and were relaxed until the maximum force on each ion and energy difference between two steps became smaller than 0.001 eV/Å and 1.0×10^{-5} eV, respectively. The adsorption energies were calculated when the system reached its asymptotical minimum energy states. The Γ -type $3 \times 3 \times 1$ Monkhorst–Pack[26] k-point mesh ($1 \times 3 \times 3$ for VA-2D MoS₂) was implemented using 400 eV as the kinetic energy cutoff for the plane-wave basis set. The system of the basal plane contains 18 Mo, 36 S, 1 N, and 2 O atoms, and the vacuum direction is set to be c-axis, while each system of VA-2D MoS₂ contains 24 Mo, 48 S, 1 N, and 2 O atoms, and the vacuum direction is a-axis. For all VA-2D MoS₂ systems, the distance between each MoS₂ layer is set to be 6.184 Å.

4.3.3. Results and Discussion

4.3.3.1. The Sequential Growth, Integration, and Patterning Process of the VA-2D MoS₂ Layers

Figure 4. 12a shows a schematic illustration of the sequential growth, integration, and patterning process of the VA-2D MoS₂ layers with serpentine patterns. Molybdenum (Mo) film of a controlled thickness (typically, >5 nm) was first deposited on a clean silicon dioxide/silicon (SiO₂/Si) substrate via electron beam evaporation. Subsequently, the sample of a Mo deposited SiO₂/Si substrate was thermally sulfurized in a CVD chamber, which converted Mo to VA-2D MoS₂ layers as demonstrated in our previous studies.[9, 11] Detailed

conditions for the CVD growth are presented in the *Experimental Method* Section. The surface of the as-prepared VA-2D MoS₂ layers/SiO₂/Si sample was then coated with a variety of adhesive polymers including poly(dimethylsiloxane) (PDMS), poly(methyl methacrylate) (PMMA), and 2,2,6,6-tetramethylpiperidine-1-oxyl (TEMPO)-oxidized cellulose nanofiber (TOCN)[30] followed by curing at elevated temperature.[13] The entire body of the sample was subsequently immersed in water followed by the manual peeling of the VA-2D MoS₂ layers/polymer film only, as previously demonstrated.[5, 13, 28, 29] The separated VA-2D MoS₂ layers/polymer film was then carved into a horseshoe-like serpentine pattern using a benchtop programmable mechanical cutter plotter. A shadow mask with a prepatterned design was integrated onto the prepared film, and gold (Au) was deposited through it defining an interdigitated electrode (IDE) serpentine pattern. All dimensional parameters, e.g., width/length of each IDE finger and the arc angle of the overall serpentine pattern, were judiciously chosen to ensure large lateral stretchability.[30] This water-assisted integration of VA-2D MoS₂ layers onto polymer films well preserves their original structural and chemical integrity, as verified in the next section. Furthermore, this serpentine-patterned VA-2D MoS₂ layers/polymer film can be translocated and attached to objects of any curvature due to its very small thickness, i.e., the polymer thickness is typically smaller than 1 μm. This serpentine pattern offers several advantages for mechanical deformability including large in-plane stretchability as well as increased allowances for out-of-plane twisting and bending, as previously demonstrated.[31, 32] Figure 4. 12b presents representative images of VA-2D

MoS₂ layers integrated onto various polymeric substrates such as PDMS and TOCN as well as an image of Au IDE-deposited VA-2D MoS₂ layer-based stretchable sensor. The optical microscopy images of as-grown VA-2D MoS₂ layers on SiO₂/Si substrates and those after transfer onto a polymeric substrate (e.g., TOCNs) confirm their highly uniform and continuous morphology on a large area.

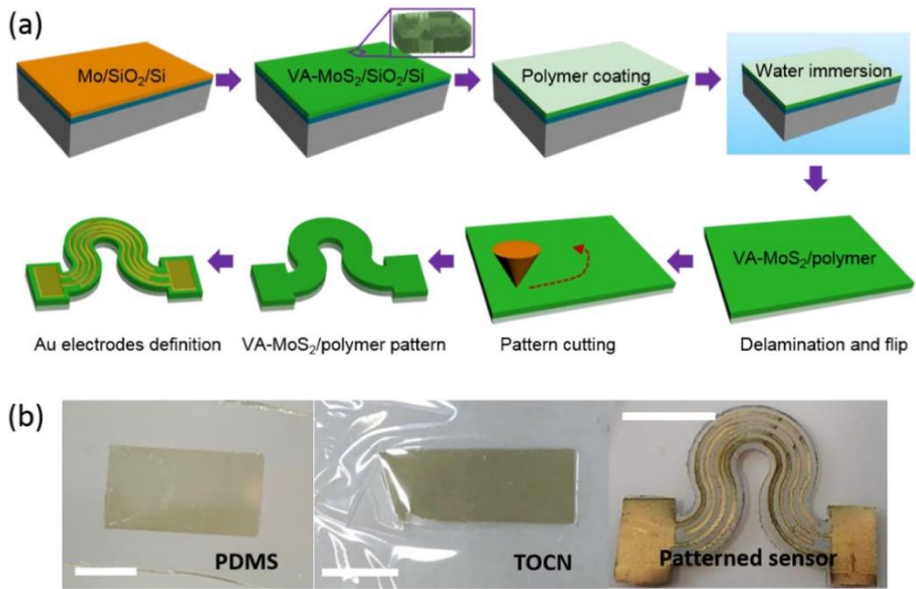


Figure 4. 12. (a) Schematic illustration of fabrication steps for VA-2D MoS₂ layer-enabled stretchable sensors. (b) Demonstration of the VA-2D MoS₂ layer integration onto various polymeric substrates and serpentine-patterned sensors. The scale bars are 1 cm in all images.

4.3.3.2. Structural and Chemical Analysis of 2D VA-MoS₂ Layers

Prior to demonstrating sensing performances of the patterned VA-2D MoS₂ layers, their material quality was verified by extensive spectroscopic and microscopic characterization techniques. Figure 4.13a shows a high-resolution transmission electron microscopy (HRTEM) image of as-grown VA-2D MoS₂ layers revealing their surface-exposed edges with uniformly spaced van der Waals (vdW) gaps of high density. The vdW gap spacing is measured to be ~ 0.65 nm homogeneously spanning across the entire sample area, consistent with our previous studies.[9, 11, 13, 14] The inset shows an optical image of the as-grown VA-2D MoS₂ layers on a SiO₂/Si substrate before their transfer and conversion to a stretchable sensor. The thickness of the as-integrated VA-2D MoS₂ layers was identified via the atomic force microscopy (AFM), which reveals that it is ~ 16 nm (Figure 4. 13b). The inset presents an AFM topography image of the corresponding VA-2D MoS₂ layers/PMMA interface within the sample. As demonstrated in Figure 4. 12b, all of the adopted polymeric substrates accompany high optical transparency (near-100% transmittance) and superior mechanical stretchability to be verified in the next section. Figure 4. 13c compares UV-visible (UV-vis) spectra of VA-2D MoS₂ layers/PMMA (red) vs bare PMMA (black). Similarly, optical transmittance is significantly reduced upon integrating VA-2D MoS₂ layers onto bare TOCN (blue and purple lines). Optical transmittance of ~ 82% was observed with the VA-2D MoS₂ layers/PMMA at a 550 nm wavelength, while the bare PMMA yielded ~ 97% transmittance, consistent with previous studies.[33–36] Figure 4. 13d shows Raman spectroscopy characterization comparing the characteristic peaks

obtained from identical VA-2D MoS₂ layers before (black) and after (red) their transfer. In both cases, peaks corresponding to in-plane (E^{1_{2g}}, at 381 cm⁻¹) and out-of-plane (A_{1g}, at 407 cm⁻¹) vibration modes are noted with a 532 nm laser line, a clear indication of the well-defined 2D MoS₂ structure. The intensity ratio of the peaks (i.e., E^{1_{2g}}/A_{1g}) is ~ 0.5, which indicates a dominance of the A_{1g} vibration mode owing to the pronouncedly exposed 2D edge sites of the vertically aligned layers.[13, 15, 37] Remarkably, there is no noticeable difference in terms of peak positions and intensity ratios before/after the transfer, indicating that the VA-2D MoS₂ layers precisely preserve their intrinsic bonding characteristics irrespective of their integration onto PMMA. Figure 4. 13e, f presents X-ray photoelectron spectroscopy (XPS) data for the identical sample before (black) and after (red) transfer in terms of the Mo 3d and S 2p orbital binding energies, respectively. In Figure 4. 13e, two distinct peaks at 229.68 and 232.88 eV are attributed, respectively, to the doublets Mo 3d_{5/2} and Mo 3d_{3/2} from the spin-orbit split of the Mo 3d core levels. Moreover, the negligible appearance of a peak at 236.2 eV corresponding to a Mo-O bonding state indicates an insignificant level of oxidation into the sample if any exists. In Figure 4. 13f, two additional peaks corresponding to the S 2p_{3/2} and S 2p_{1/2} orbitals of divalent sulfide ions (S²⁻) are observed at 162.79 and 163.97 eV binding energies, respectively. This XPS analysis yields an estimated atomic ratio of Mo/S = ~ 1:2.17 indicating the sulfur (S)-rich nature of the VA-2D MoS₂ layers. Previous studies suggest that such VA-2D MoS₂ layers grown by the direct sulfurization of Mo films exhibit *p*-type semiconducting characteristics due to their S-rich (or Mo-deficient)

stoichiometry,[38–40] which is also consistent with our own observation to be presented in the next section. Furthermore, XPS peaks specific to the orbital states of elemental Mo are not observed, indicating that Mo atoms were entirely converted to crystalline 2D MoS₂ layers through the CVD sulfurization reaction. All of the above discussed structural and chemical analyses confirm that VA-2D MoS₂ layers well maintain their original material quality even after integration to polymer substrates.

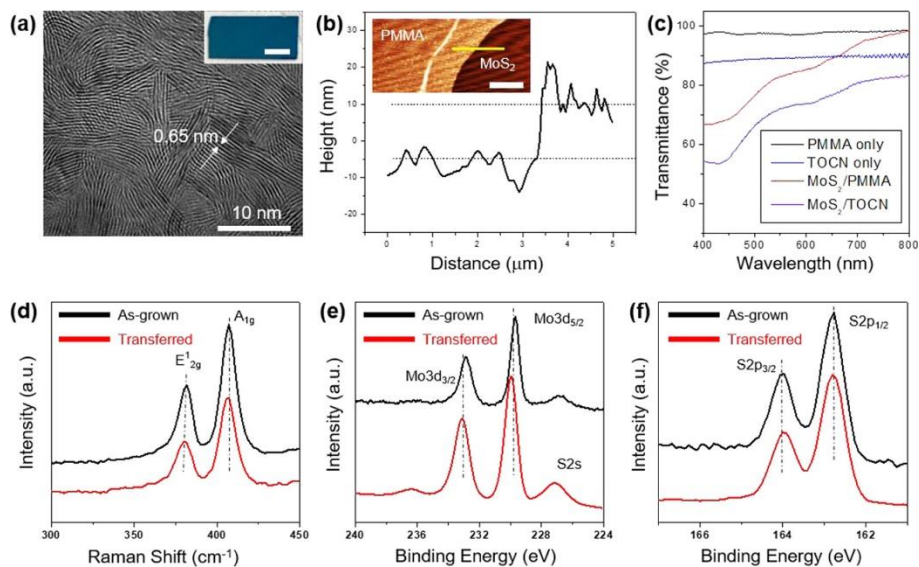


Figure 4. 13. (a) Plane-view HRTEM image of VA-2D MoS₂ layers and the corresponding sample image (inset). The scale bar in the inset is 1 cm. (b) AFM height profile of VA-2D MoS₂ layers/PMMA interface and the corresponding topography image (inset). The scale bar in the inset is 5 μm. (c) Optical transmittance spectra of PMMA and TOCN before/after integrating VA-2D MoS₂ layers. (d) Raman spectra from VA-2D MoS₂ layers in their pristine (black) and transferred (red) states. (e, f) XPS spectra for Mo and S binding energies of VA-2D MoS₂ layers: (e) Mo 3d core level before (black) and after (red) transfer and (f) S 2p core level before (black) and after (red) transfer.

4.3.3.3. Gas Sensing Performance of Serpentine VA-MoS₂ Layers

Prepared VA-2D MoS₂ layers in serpentine patterns were electrically evaluated with/without mechanical stretching. Figure 4. 14a shows representative images of serpentine-patterned VA-2D MoS₂ layers with Au electrodes undergoing sequential lateral stretching. The strain ratio is defined to be $\Delta l/l_0$, where l_0 is the initial lateral length between the large left/right contact pads and Δl is the increase in the length. It is noted that the sample becomes gradually distorted in the out-of-plane orientation with increasing the strain ratio, particularly pronounced with >70% strain. The electrical performance of the same sample undergoing the lateral stretching is manifested by its current–voltage (I–V) characteristics obtained at various strain levels, as shown in Figure 4. 14b. Although the current steadily decreases with increasing strain levels, the sample remains highly conductive even under 40% stretch retaining ~ 25% of the initial conductance. The inset shows an image of the sample corresponding to the presented I–V plots. We then characterized the structural and chemical integrity of the sample with/without the stretching by employing Raman spectroscopy. Figure 4. 14c compares the Raman spectra of the same sample in its pristine state (black) and under 40% strain (red). The signature peaks corresponding to the in-plane (E_{2g}^1) and the out-of-plane (A_{1g}) vibration modes are observed to be at identical positions irrespective of the lateral stretching. No peak splitting is present at a 40% strain, which would otherwise appear if the applied strain significantly modified the lattice structure of the sample or broke its symmetry.[32, 41, 42] These observations indicate that the serpentine-patterned VA-2D MoS₂ layers sustainably retain a high

degree of electrical and structural quality even up to 40% strain, significantly higher than the in-plane strain limit of 2D MoS₂ layers.[43] The gas sensing capability of the serpentine-patterned VA-2D MoS₂ layers was tested inside a sealed acrylic vacuum chamber through which NO₂ gas of controlled concentration was fed in. A commercial NO₂ gas sensor positioned right next to the sensing sample was used as a reference to ensure precision monitoring of the gas concentration. Figure 4. 14d presents a real-time electrical sensing of NO₂ gas of increasing concentration, manifested by time (T; x-axis) vs sensitivity (S; y-axis). The sensitivity is defined to be $S = \Delta I/I_0 \times 100$ (%), where ΔI represents the gas-induced current change; i.e., I_0 and I_g are the current of the sensor with/without the gas, respectively.[44, 45] The plot reveals the prominent current increase of the serpentine-patterned VA-2D MoS₂ layers in the pristine state (0% strain) with NO₂ gas of increasing concentration, measured at a constant voltage of 7 V. Figure 4. 14e exhibits a plot of concentration vs sensitivity, similar to the trends observed in recent studies on 2D MoS₂ layer-based NO₂ gas sensing.[46, 47] The observed sensitivity value is in a range of ~160–380% for the concentration of 5–30 ppm, much higher than those obtained with horizontally aligned 2D MoS₂ layers exposing basal planes. The practical feasibility of the VA-2D MoS₂ layers as a stretchable sensor was demonstrated by measuring their current change under tensile stretching. The sample was maintained to be laterally stretched at a uniaxial strain of 40%, and its temporal current was monitored under a periodic supply of a 5 ppm NO₂ concentration. Figure 4. 14f presents a highly uniform increase of the current upon the introduction of NO₂ gas, which reversibly returns to the

original value upon its termination. Although the sensitivity is reduced to ~ 125%, i.e., ~ 78% of that achieved at 0% strain under the same concentration (Figure 4. 13d), this value is still much higher than those in previous reports despite the large lateral stretching. Such reproducible and consistent current responses must be attributed to the serpentine pattern, which efficiently minimizes the distortion of the vertical alignment of 2D layers maintaining their surface-exposed dangling bonds. Figure 4. 13g shows a plot to comprehensively compare the sensing performances of VA-2D MoS₂ layers in this study vs other MoS₂ layer-based sensors in terms of NO₂ sensitivity and concentration.[2, 7, 18, 21, 44, 48–57] Our VA-2D MoS₂ layer-based sensor presents significantly higher sensitivity in detecting NO₂ gas of comparable concentration as well as the additional advantage of large stretchability unprecedented in previous approaches. This “intrinsically” superior sensitivity must be a combined result of (1) the richness of the surface-exposed dangling bonds inherent to VA-2D layers, which significantly facilitates the chemisorption of gas molecules as predicted by a recent DFT study;[17] and (2) the increased surface area of VA-2D layers, providing a significantly larger density of chemisorption sites compared to their horizontally aligned 2D layer counterparts. Indeed, the surface roughness of 2D layers is known to significantly (>10 times) increase as their layer orientation undergoes a horizontal-to-vertical transition, generally observed in various 2D TMD layers.[11] This structural distinction of VA-2D layers becomes particularly pronounced if compared to mechanically exfoliated 2D flakes, which expose atomically smooth basal planes with saturated atomic bonds, thus limiting

sensitivity. Moreover, the prominent current increase introduced by NO₂ molecules is attributed to the chemisorption-driven charge transfer between them and VA-2D MoS₂ layers, where NO₂ molecules can be easily chemisorbed on the layer surfaces as facilitated by enriched dangling bonds. Owing to their highly oxidizing nature, NO₂ molecules extract electrons from VA-2D MoS₂ layers (*p*-type, in this case) increasing their hole concentration and thus the increased electrical conductivity. Indeed, it is well known that NO₂ acts as an electron acceptor (*p*-type doping) as observed in previous studies reporting NO₂-driven increase of electrical conductivity.[6, 7, 55, 58] Our VA-2D MoS₂ layers in their pristine state were confirmed to exhibit *p*-type characteristics by a field-effect transistor (FET) measurement in a back-gate configuration. It is worth mentioning that NO₂ molecules exert a considerably higher binding energy when interfaced with 2D layer edges compared to basal planes, which must be drastically promoted in this case of VA-2D MoS₂ layers.[6, 17, 21, 55, 59] Furthermore, we note that the NO₂ sensing performance of our VA-2D MoS₂ layers in stretchable forms is significantly superior to that of other VA-2D MoS₂ layers employed for flexible sensing devices.[46] This distinction is attributed to the fact that our materials exhibit an extremely high density of all vertically aligned 2D layers (Figure 4. 13a), while the previously developed ones typically contain some domains of horizontally aligned 2D layers with surface-exposed basal planes.[46] To further verify the well-preserved electrical characteristics of VA-2D MoS₂ layers upon mechanical deformation, we also demonstrated additional functionalities of the sensing devices. Figure 4. 13h shows temporal photo-responsiveness obtained from another sample

under a periodic illumination of a white LED (intensity: 20 W/m²). The sample in its pristine state exhibited pronounced generation/decay of photocurrent in response to the ON/OFF illumination switching in a reversible manner (black plot). This reliable photocurrent generation was well retained even when the sample was laterally stretched at a 40% strain (red plot). We emphasize that the present study focuses on a precisely defined large-area (>2 cm²) VA-2D MoS₂ layers in stretchable forms for multifunctional high-performance sensing applications, difficult to attain with conventional approaches.

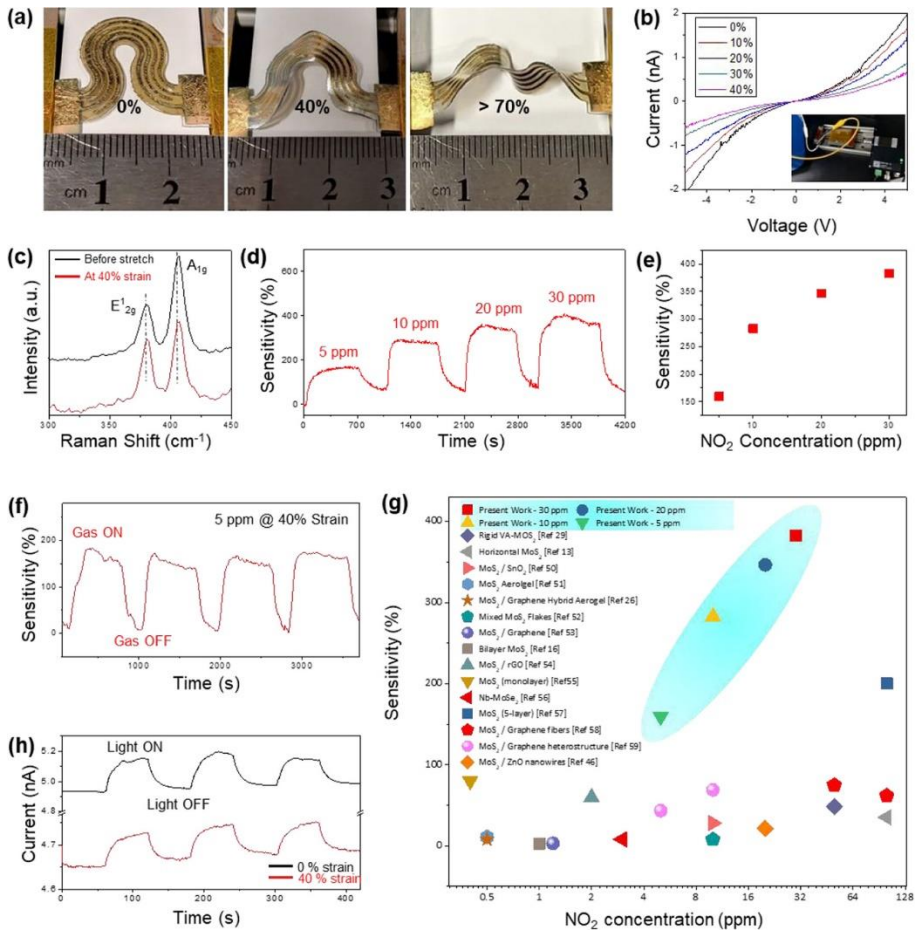


Figure 4. 14. (a) Demonstration of lateral stretching in VA-2D MoS₂ layers. (b) I-V characterization corresponding to the sample in (a) with up to 40% strain. (c) Raman characterization corresponding to the sample in (a) before/after 40% stretching. (d) Electrical sensing of NO₂ gas with increasing concentration without stretching. (e) Concentration-dependent sensitivity. (f) NO₂ gas sensing with laterally stretched VA-2D MoS₂ layers at a 40% strain. (g) NO₂ sensing performance comparisons of this work vs other 2D MoS₂ layer-based sensors. (h) Demonstration of photocurrent generation in VA-2D MoS₂ layers at 0 and 40% strain.

4.3.3.4. FEM Simulation for Mechanical Stretching

To gain insight into the influence of the mechanical stretching on resulting properties, we employed a three-dimensional (3D) finite element method (FEM) simulation and verified the lateral stretchability of the serpentine-patterned VA-2D MoS₂ layers. Figure 4. 15a presents a schematic illustration of the serpentine pattern with dimensional parameters adopted for the experimental demonstration as well as for the FEM simulation. The pattern is composed of four main parameters, i.e., path width (w), arc radius (r), arc angle (α), and arm length (l), following the convention used in previous serpentine studies.[30, 60] The stretchability of the serpentine pattern can be qualitatively predicted by a generic function for linear elastic materials, i.e., $\epsilon_{\max}/\epsilon_{\text{app}} = f(\alpha, w/r, l/r)$, where ϵ_{\max} and ϵ_{app} present the maximum normal strain and the applied strain, respectively. The stretchability value increases with increasing l/r and α as well as decreasing w/r as known in the literature.[30] We used the parameter values of $w = 6 \text{ mm}$, $r = 5 \text{ mm}$, $\alpha = 27.5^\circ$, and $l = 0 \text{ mm}$ for both the experiments and the simulation, which were judiciously selected to achieve large lateral stretchability considering the physical limitation of our experimental setup. Figure 4. 15b presents FEM simulation images revealing the spatial distribution of the maximum principal strain within the serpentine pattern at the tensile stretch levels of 0, 20, and 40%. The maximum principal strain is observed to be concentrated in the center of the inner edges of the pattern with high curvature, which becomes more pronounced with increasing stretching. Plots of stretch rate vs resulting maximum principal strain are presented in Figure 4. 15c, which is complementary to Figure 4. 15b. Furthermore, a transition from

2D in-plane to 3D out-of-plane deformation is observed with increasing stretch levels, which results in twisting these edges in a way to relieve their concentrated strain. Accordingly, these local areas are anticipated to exhibit more significant deformation than any others in the actual experiment. Indeed, the FEM simulation image well agrees with the experimental observation obtained at a 40% strain. Similarly, a variety of strain-engineering approaches have been employed to realize strain-invariant electrical properties in laterally patterned large area 2D layers.[61, 62] The underlying common principle is to efficiently relieve externally exerted in-plane strain by converting it into out-of-plane torsional strain.[61, 62]

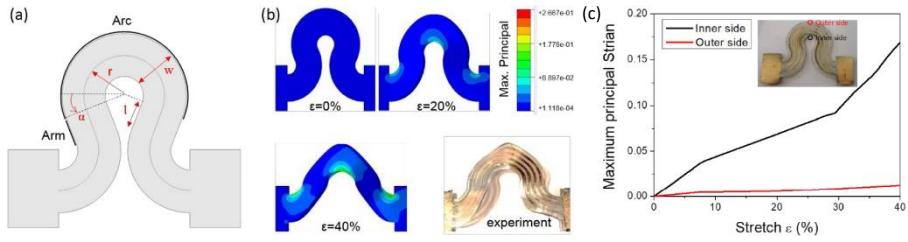


Figure 4. 15. (a) Schematic of the serpentine pattern with dimensional parameters. (b) FEM images showing the spatial distribution of maximum principal strain and their consistency with the experimental observation. (c) Plots of stretch rate vs. resulting maximum principal strain corresponding to the two different locations in the inset image.

4.3.3.5. DFT Calculations for the Superiority of VA-2D MoS₂ Layers for NO₂ Gas Sensing

The superiority of VA-2D MoS₂ layers for NO₂ gas sensing in their pristine and stretch forms was corroborated by DFT calculations, as presented in Figure 4. 16. For this, we developed slab-vacuum-slab models for the 2D MoS₂ layers exposing basal planes and edge sites on their surface and calculated their corresponding adsorption energies of NO₂ molecules. The gas adsorption energy, E_{ads} , with respect to the 2D MoS₂ surfaces is defined as $E_{\text{ads}} = E_{\text{tot}} - (E_{\text{MoS}_2} + E_{\text{gas}})$, where E_{tot} refers to the total energy of a fully relaxed system containing both 2D layers and molecules, while E_{MoS_2} and E_{gas} indicate the total energy of fully relaxed 2D layers and molecules, respectively. Figure 4. 16a presents the case of NO₂ molecules adsorbed to the basal plane of 2D MoS₂ layers, confirming a very weak adsorption energy of -0.292 eV and a long bond distance of 3.109 Å between the oxygen (O) atom (red sphere) and the S atom (yellow sphere). Adsorptions of NO₂ molecules to the surface of VA-2D MoS₂ layers are presented for the cases of S (Figure 4. 16b, c) and Mo (Figure 4. 16d, e) atom-exposed edges, respectively. In Figure 4. 16b, the adsorption energy of NO₂ molecules with respect to the S edges is calculated to be -0.680 eV, significantly higher than that observed with the 2D MoS₂ basal plane in Figure 4. 16a. Furthermore, the O–S bond distance between the NO₂ molecule and the 2D MoS₂ layer edge is 1.609 Å, much shorter than that observed with the basal plane adsorption. Such distinct characteristics indicate that NO₂ molecules are predominantly chemi-adsorbed to the surface of VA-2D MoS₂ layers while they prefer physisorption on the 2D MoS₂ basal plane. In addition to studying

pristine VA-2D MoS₂ layers, we also investigated the adsorption characteristics of NO₂ molecules with respect to the VA-2D MoS₂ layers subjected to a tensile stretching. We elongated the pristine VA- 2D MoS₂ layers in Figure 4. 16b along the b-axis (zigzag direction) by 10% and identified the NO₂ absorption characteristics with respect to S edges (Figure 4. 16c). Interestingly, the adsorption energy increases from -0.680 to -0.917 eV following the 10% stretching and the O atom is observed to bind to the Mo atom (purple sphere) instead of a S atom; the O–Mo bond distance of 2.302 Å in this stretched form is significantly shorter than 3.327 Å of the O–Mo bond in the pristine form. This preferred binding configuration of O–Mo over O–S might have been caused by the reduced steric effect of S atoms at the layer edges, promoted by the deformation of VA-2D MoS₂ layers along the b-axis. We also examined the case of NO₂ adsorption with respect to the Mo edges of VA-2D MoS₂ layers in their pristine (Figure 4. 16d) vs 10%-stretched (Figure 4. 16e) forms. The adsorption energy of NO₂–Mo in the pristine state is calculated to be -4.500 eV, which is significantly higher than those observed with the binding of NO₂ molecules to the basal planes and S edge-exposed VA-2D MoS₂ layers. This observation indicates that the large density of surface-exposed Mo atoms in VA-2D MoS₂ layers plays the most significant role in determining the overall gas sensing performance, possibly outweighing contributions from the S edges. Furthermore, this analysis well accounts for the significantly higher (typically, >5 times) sensitivity of our VA-2D MoS₂ layer-based sensors over the previous developments employing horizontally aligned layers (Figure 4. 14g). In Figure 4. 16e, NO₂ molecules start to interact with Mo atoms even more strongly upon

10% stretching, manifested by a higher adsorption energy of -4.762 eV and a shorter Mo–O bond distance of 1.916 Å compared to the pristine state. These DFT calculations strongly confirm that VA-2D MoS₂ layers well preserve their intrinsically superior NO₂ gas sensing capability and mechanical robustness under tensile stretching in terms of both adsorption energy and atomic bond distances. The slightly degraded sensitivity under stretching observed in our experiments (i.e., Figure 4. 14f) might be attributed to the randomness of the vertical orientation of individual 2D layers (Figure 4. 13a), which must complicate the application of tensile stretching along a well-defined axis (e.g., b-axis), unlike the DFT modeling.

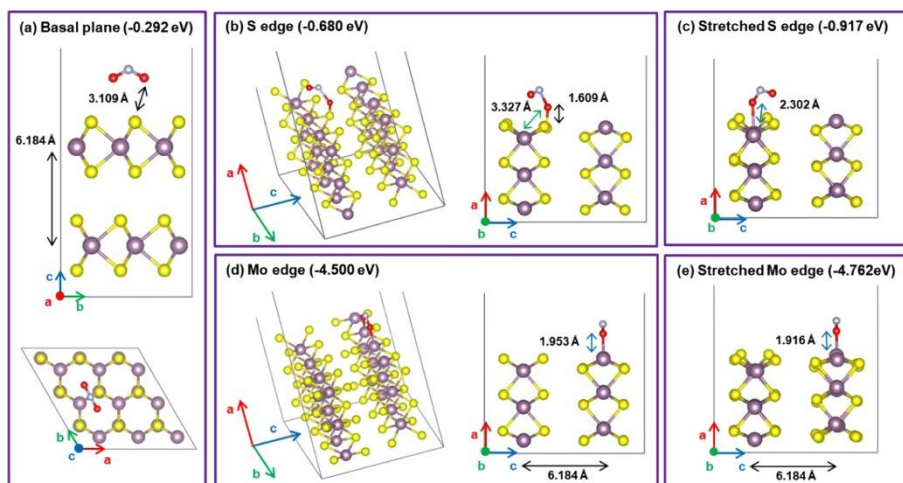


Figure 4. 16. DFT calculations for the adsorption states of NO₂ molecules with 2D MoS₂ layers in various configurations. (a) Snapshots of the relaxed configuration of the 2D MoS₂ layer basal plane viewed along the a- (top) and c-axis (bottom). (b) Snapshots of the relaxed configuration of VA-2D MoS₂ layers with NO₂ adsorbed to a S-exposed edge. (c) Snapshots of the relaxed configuration of VA-2D MoS₂ stretched along the b-axis (zigzag direction) by 10% of its original lattice constant with NO₂ adsorbed to a S-exposed edge. (d) Snapshots of the relaxed configuration of VA-2D MoS₂ layers with NO₂ adsorbed to a Mo-exposed edge. (e) Snapshots of the relaxed configuration of VA-2D MoS₂ stretched along the b-axis by 10% of its original lattice constant with NO₂ adsorbed to a Mo-exposed edge. In all Figures, the yellow-, purple-, gray-, and red-colored spheres indicate S, Mo, N, and O atoms, respectively.

4.3.4. Conclusion

In summary, we report high-performance VA-2D MoS₂ layer based NO₂ sensors with serpentine patterns, which combine extremely high sensitivity and large lateral stretchability. In addition to these combined advantages, the areal dimension of VA-2D MoS₂ layers is >cm² and they can be integrated onto versatile substrates, suggesting their great versatility for practically relevant applications. The material properties and the gas sensing principle unveiled in this study must be critically useful for further exploring them for futuristic sensor devices of unconventional form factors and unprecedented multifunctionalities.

4.3.5. Reference

- (1) Lee, K., et al. High-performance Sensors Based on Molybdenum Disulfide Thin Films. *Adv. Mater.* 2013, 25, 6699–6702.
- (2) Kumar, R., et al. UV-activated MoS₂ Based Fast and Reversible NO₂ Sensor at Room Temperature. *ACS Sens.* 2017, 2, 1744–1752.
- (3) Islam, M., et al. Three dimensionally ordered 2D MoS₂ vertical layers integrated on flexible substrates with stretchtunable functionality and improved sensing capability. *Nanoscale* 2018, 10, 17525–17533.
- (4) Ko, T.-J., et al. Large-area 2D TMD Layers for Mechanically Reconfigurable Electronic Devices. *J. Phys. D: Appl. Phys.* 2020, 53, 313002–313028.
- (5) Wang, M., et al. Manufacturing Strategies for Wafer-scale Two-dimensional Transition Metal Dichalcogenide Heterolayers. *J. Mater. Res.* 2020, 35, 1350–1368.

- (6) Kim, J.-S., et al. Tunable Volatile Organic Compounds Sensor by Using Thiolated Ligand Conjugation on MoS₂. *Nano Lett.* 2014, 14, 5941–5947.
- (7) Xu, T., et al. High-response NO₂ Resistive Gas Sensor Based on Bilayer MoS₂ Grown by a New Two-step Chemical Vapor Deposition Method. *J. Alloys Compd.* 2017, 725, 253–259.
- (8) Han, S. S., et al. Automated Assembly of Wafer-Scale 2D TMD Heterostructures of Arbitrary Layer Orientation and Stacking Sequence Using Water Dissoluble Salt Substrates. *Nano Lett.* 2020, 20, 3925–3934.
- (9) Wang, M., et al. Structural Evolutions of Vertically Aligned Two-Dimensional MoS₂ Layers Revealed by in Situ Heating Transmission Electron Microscopy. *J. Phys. Chem. C* 2019, 123, 27843–27853.
- (10) Hwang, J.-H., et al. Improving Electrochemical Pb²⁺ Detection using a Vertically Aligned 2D MoS₂ Nanofilm. *Anal. Chem.* 2019, 91, 11770–11777.
- (11) Han, S. S., et al. Horizontal-to-vertical Transition of 2D Layer Orientation in Low-temperature Chemical Vapor Deposition-grown PtSe₂ and its Influences on Electrical Properties and Device Applications. *ACS Appl. Mater. Interfaces* 2019, 11, 13598–13607.
- (12) Kalita, H., et al. Artificial Neuron using Vertical MoS₂/Graphene Threshold Switching Memristors. *Sci. Rep.* 2019, 9, No. 53.
- (13) Choudhary, N., et al. Strain-Driven and Layer-Number-Dependent Crossover of Growth Mode in van der Waals Heterostructures: 2D/2D Layer-By-Layer Horizontal Epitaxy to 2D/3D Vertical Reorientation. *Adv. Mater. Interfaces* 2018, 5, No. 1800382.
- (14) Islam, M. A., et al. Centimeter-scale 2D Van der Waals Vertical Heterostructures Integrated on Deformable Substrates Enabled by Gold Sacrificial Layer-assisted Growth. *Nano Lett.* 2017, 17, 6157–6165.

- (15) Choudhary, N., et al. Centimeter Scale Patterned Growth of Vertically Stacked Few Layer Only 2D MoS₂/WS₂ Van der Waals Heterostructure. *Sci. Rep.* 2016, 6, No. 25456.
- (16) Lee, E., et al. Two-dimensional Transition Metal Dichalcogenides and Metal Oxide Hybrids for Gas Sensing. *ACS Sens.* 2018, 3, 2045–2060.
- (17) Cho, S.-Y., et al. Highly Enhanced Gas Adsorption Properties in Vertically Aligned MoS₂ Layers. *ACS Nano* 2015, 9, 9314–9321.
- (18) Long, H., et al. High Surface Area MoS₂/Graphene Hybrid Aerogel for Ultrasensitive NO₂ Detection. *Adv. Funct. Mater.* 2016, 26, 5158–5165.
- (19) Zhang, D., et al. Detection of NO₂ Down to ppb Levels Using Individual and Multiple In₂O₃ Nanowire Devices. *Nano Lett.* 2004, 4, 1919–1924.
- (20) Guo, J., et al. Enhanced NO₂ Gas Sensing of A Single-layer MoS₂ by Photogating and Piezo-phototronic Effects. *Sci. Bull.* 2019, 64, 128–135.
- (21) Kumar, R., et al. Highly Selective and Reversible NO₂ Gas Sensor Using Vertically Aligned MoS₂ Flake Networks. *Nanotechnology* 2018, 29, No. 464001.
- (22) Summerlin, L. R., et al. Investigation of Nitric Acid: Chemical Demonstrations: A Sourcebook for Teachers, 2nd ed.; American Chemical Society: Washington, D.C., 1988; Vol. 2.
- (23) Kresse, G.; Furthmüller, J. Efficient Iterative Schemes for ab initio Total-energy Calculations using a Plane-wave Basis Set. *Phys. Rev. B: Condens. Matter Mater. Phys.* 1996, 54, 11169–11186.
- (24) Kresse, G.; Joubert, D. From ultrasoft pseudopotentials to the projector augmented-wave method. *Phys. Rev. B: Condens. Matter Mater. Phys.* 1999, 59, 1758–1775.
- (25) Grimme, S.; Antony, J.; Ehrlich, S.; Krieg, H. A consistent and accurate

ab initio Parametrization of Density Functional Dispersion Correction (DFT-D) for the 94 Elements H-Pu. *J. Chem. Phys.* 2010, 132, No. 154104.

(26) Monkhorst, H. J.; Pack, J. D. Special Points for Brillouin-zone Integrations. *Phys. Rev. B: Condens. Matter Mater. Phys.* 1976, 13, 5188–5192.

(27) Yoo, C., et al. Wafer-Scale 2D MoS₂ Layers Integrated on Cellulose Substrates Towards Environmentally Friendly Transient Electronic Devices. *ACS Appl. Mater. Interfaces* 2020, 12, 25200–25210.

(28) Li, H., et al. Experimental Realization of Few Layer Two-Dimensional MoS₂ Membranes of Near Atomic Thickness for High Efficiency Water Desalination. *Nano Lett.* 2019, 19, 5194–5204.

(29) Kim, J. H., et al. Centimeter-scale Green Integration of Layer-by-Layer 2D TMD vdW Heterostructures on Arbitrary Substrates by Water-Assisted Layer Transfer. *Sci. Rep.* 2019, 9, No. 1641.

(30) Lee, Y., et al. Approaches to Stretchable Polymer Active Channels for Deformable Transistors. *Macromolecules* 2016, 49, 433–444.

(31) Sim, K., et al. Biaxially Stretchable Ultrathin Si Enabled by Serpentine Structures on Pre-strained Elastomers. *Adv. Mater. Technol.* 2019, 4, No. 1800489.

(32) Trung, T. Q.; Lee, N.-E. Materials and Devices for Transparent Stretchable Electronics. *J. Mater. Chem. C* 2017, 5, 2202–2222.

(33) Kong, D., et al. Synthesis of MoS₂ and MoSe₂ Films with Vertically Aligned Layers. *Nano Lett.* 2013, 13, 1341–1347.

(34) Park, M., et al. MoS₂-based Tactile Sensor for Electronic Skin Applications. *Adv. Mater.* 2016, 28, 2556–2562.

(35) Kim, T.-Y., et al. Transparent Large-area MoS₂ Phototransistors with Inkjet-Printed Components on Flexible Platforms. *ACS Nano* 2017, 11,

10273–10280.

(36) Wang, D., et al. MoS₂ Incorporated Hybrid Hole Transport Layer for High Performance and Stable Perovskite Solar Cells. *Synth. Met.* 2018, 246, 195–203.

(37) Islam, M. A., et al. Noble Metal coated MoS₂ Nanofilms with Vertically-aligned 2D Layers for Visible Light-driven Photocatalytic Degradation of Emerging Water Contaminants. *Sci. Rep.* 2017, 7, No. 14944.

(38) McDonnell, S., et al. Defect-dominated Doping and Contact Resistance in MoS₂. *ACS Nano* 2014, 8, 2880–2888.

(39) Park, J., et al. Thickness Modulated MoS₂ Grown by Chemical Vapor Deposition for Transparent and Flexible Electronic Devices. *Appl. Phys. Lett.* 2015, 106, No. 012104.

(40) Liu, C., et al. Rapid Water Disinfection Using Vertically Aligned MoS₂ Nanofilms and Visible Light. *Nat. Nanotechnol.* 2016, 11, 1098–1104.

(41) Yang, R., et al. Tuning Optical Signatures of Single and few-layer MoS₂ by Blown-bubble Bulge Straining up to Fracture. *Nano Lett.* 2017, 17, 4568–4575.

(42) Conley, H. J., et al. Bandgap Engineering of Strained Monolayer and Nilayer MoS₂. *Nano Lett.* 2013, 13, 3626–3630.

(43) Bhimanapati, G. R., et al. Recent Advances in Two-Dimensional Materials Beyond Graphene. *ACS Nano* 2015, 9, 11509–11539.

(44) Zhao, S., et al. Vertically Aligned MoS₂/ZnO Nanowires Nanostructures with Highly Enhanced NO₂ Sensing Activities. *Appl. Surf. Sci.* 2018, 456, 808–816.

(45) Li, Z., et al. Room-temperature Synthesis of CuO/reduced Graphene Oxide Nanohybrids for High-performance NO₂ Gas Sensor. *Sens. Actuators, B* 2018,

271, 306–310.

(46) Zhao, Y., et al. Low-temperature Synthesis of 2D MoS₂ on a Plastic Substrate for a Flexible Gas Sensor. *Nanoscale* 2018, 10, 9338–9345.

(47) Cho, B., et al. Bifunctional Sensing Characteristics of Chemical Vapor Deposition Synthesized Atomic layered MoS₂. *ACS Appl. Mater. Interfaces* 2015, 7, 2952–2959.

(48) Cui, S., et al. Stabilizing MoS₂ Nanosheets through SnO₂ Nanocrystal Decoration for High-performance Gas Sensing in Air. *Small* 2015, 11, 2305–2313.

(49) Long, H., et al. 3D MoS₂ Aerogel for Ultrasensitive NO₂ Detection and its Tunable Sensing Behavior. *Adv. Mater. Interfaces* 2017, 4, No. 1700217.

(50) Agrawal, A. V., et al. Photoactivated Mixed In-plane and Edge-enriched P-type MoS₂ Flake-based NO₂ Sensor Working at Room Temperature. *ACS Sens.* 2018, 3, 998–1004.

(51) Cho, B., et al. Chemical Sensing of 2D Graphene/MoS₂ Heterostructure Device. *ACS Appl. Mater. Interfaces* 2015, 7, 16775–16780.

(52) Zhou, Y., et al. Ultrasensitive NO₂ Gas Sensing Based on rGO/MoS₂ Nanocomposite Film at Low Temperature. *Sens. Actuators, B* 2017, 251, 280–290.

(53) Liu, B., et al. High-performance Chemical Sensing Using Schottky-contacted Chemical Vapor Deposition Grown Monolayer MoS₂ Transistors. *ACS Nano* 2014, 8, 5304–5314.

(54) Choi, S. Y., et al. Effect of Nb Doping on Chemical Sensing Performance of Two-Dimensional Layered MoSe₂. *ACS Appl. Mater. Interfaces* 2017, 9, 3817–3823.

(55) Late, D. J., et al. Sensing Behavior of Atomically Thin-layered MoS₂

Transistors. ACS Nano 2013, 7, 4879–4891.

(56) Niu, Y., et al. MoS₂ Graphene Fiber Based Gas Sensing Devices. Carbon 2015, 95, 34–41.

(57) Hong, H. S., et al. Highly Sensitive and Low Detection Limit of Resistive NO₂ Gas Sensor Based on A MoS₂/graphene Two-dimensional Heterostructures. Appl. Surf. Sci. 2019, 492, 449–454.

(58) Kim, H.-J.; Lee, J.-H. Highly Sensitive and Selective Gas Sensors using P-type Oxide Semiconductors: Overview. Sens. Actuators, B 2014, 192, 607–627.

(59) Jaramillo, T. F., et al. Identification of Active Edge Sites for Electrochemical H₂ Evolution from MoS₂ Nanocatalysts. Science 2007, 317, 100–102.

(60) Yang, S.; Ng, E.; Lu, N. Indium Tin Oxide (ITO) Serpentine Ribbons on Soft Substrates Stretched Beyond 100%. Extreme Mech. Lett. 2015, 2, 37–45.

(61) Okogbue, E., et al. Multifunctional Two-Dimensional PtSe₂-Layer Kirigami Conductors with 2000% Stretchability and Metallic-to-Semiconducting Tunability. Nano Lett. 2019, 19, 7598–7607.

(62) Ko, T.-J., et al. Wafer-scale 2D PtTe₂ layers-enabled Kirigami heaters with superior mechanical stretchability and electro-thermal responsiveness. Appl. Mater. Today 2020, 20, 100718–100727.

Chapter 5. Total Conclusion

In this thesis, I have studied a horizontal to vertical orientation transition mechanism of 2D PtSe₂ and 2D PtTe₂ layers and the transfer approach using the water-assisted method and water-soluble salts substrates onto elastomeric substrates including paper, polymers. I then advanced my study and demonstrated a stretchable future electronic device (e.g., ultra-high stretchable conductors, stretchable FET device, stretchable electronic heater, and transparent smart window) using the kirigami and the serpentine pattern techniques.

First, this thesis work indicates that the transition from the horizontal-to-vertical growth direction of 2D TMDs layer growth strongly depends on the strain that comes from the lack of space of 2D TMDs growth. With the increase of the initial metal (Pt) thickness, the 2D TMDs layers (PtSe₂ and PtTe₂ layers) don't secure the space for horizontal growth having a low energy state compare to vertical growth. The collision of growing horizontal aligned 2D TMDs layers causes strains and the growth changes the direction to open space which means vertical direction. I conducted the orientation transition behavior with the initial thickness of the metal layer controlling the empty space for the 2D TMDs growth. With the orientation control growth, I achieve the control of the electronic property of 2D TMDs layer from semiconductor to high-metallic property.

Second, I developed the transfer method using water. The key factor of the water-assisted transfer is the water penetration between the growth substrate (SiO₂/Si wafer) and the 2D TMDs layers. This water penetration strongly

depends on the surface energy difference between the hydrophilic SiO₂/Si wafer and the hydrophobic 2D TMDs layer. And the adhesion between the SiO₂ surface and 2D TMDs dominantly effect to separation of 2D TMDs layers. I conducted the delamination of large area horizontally aligned 2D MoS₂ layer on SiO₂/Si wafer using the water-assisted transfer method and integrate onto secondary elastomeric substrates. The aging effect on the 2D MoS₂ layer causing the increase of hydrophobic property makes the delamination of the layer more easily, which supports the theory of the delamination mechanism. I then applied the water-soluble salt substrates including NaCl, KCl, and KBr for the vertically aligned 2D TMDs layers. With the mechanism of the water-assisted transfer, the vertically aligned 2D TMDs layers are not delaminated from the growth substrate due to its strong adhesion between 2D TMDs layers and the growth substrate. The water-soluble substrates offer the facile direction of delamination and good quality of the 2D TMDs growth. I successfully demonstrated the delamination of 2D TMDs regardless of the orientation of the growth and integrated them onto various elastomeric substrates.

Lastly, I demonstrated various electronic applications using the orientation control growth and water-assisted transfer method. I employed the kirigami pattern and the serpentine pattern in order to apply the stretchability to the electronic devices using the transition from 2D structure to 3D structure. I optimized the design of the pattern and achieved high lateral stretchability over 2000% and 100% biaxial stretchability. With all of the techniques described above(the orientation control, the water-assisted transfer, the 3D patterning of 2D materials), I successfully demonstrated the future electronic devices

including the ultra-high stretchable conductors, stretchable FET device, stretchable electronic heater, smart window, and high-performance stretchable gas sensor.

Abstract in Korean

MX_2 (M: 전이 금속, X: 칼코젠) 형태를 나타내는 2 차원 (2D) 전이 금속 디칼코제나이드 (TMDs) 물질은 뛰어난 구조적, 물리적, 그리고 화학적 특성으로 인하여 전자기기장치 분야에서 많은 흥미를 받고 있다. 특히 백금 (Pt) 기반의 2D TMDs 물질은 두께에 따른 반도체에서 금속으로의 성질 변화, 높은 안정성, 그리고 낮은 합성온도 등의 기존 2D TMDs 물질에서는 나타나지 않는 다양한 이점을 가지고 있다. 이러한 반도체-금속의 전기적 물성 전이 특성은 2D TMDs 물질의 층상구조와 관련이 있는 것으로 알려져 있으나, 많은 연구에도 불구하고 아직까지 2D TMDs 물질의 구조적 특성과 전기적 특성 사이의 관계가 명확하게 밝혀지지 않고 있다.

또한 작은 두께로 기인되는 2D TMDs 물질은 그들의 뛰어난 전기적, 물리적, 광학적 특성으로 미래의 신축성 및 접이식 전자 장치의 우수한 후보로 여겨지고 있으며, 이러한 미래 전자장비로의 적용을 위하여 2D TMDs 물질을 유연한 기판으로의 박리 및 전사하는 기술이 요구되어 관련된 활발한 연구가 이루어지고 있다. 그러나 2D TMDs 물질의 큰 변형률의 한계를 갖는 뛰어난 물리적 특성에도 불구하고, 박리 및 전사를 통한 2D TMDs 물질의 높은 신축성, 접이식 전자 장치로의 응용을 위한 기계적 내구성의 확보는 아직까지 잘 실현되고 있지 않다.

본고에서는 대면적 2D TMDs 물질 중 PtSe₂ 층상구조 및 PtTe₂ 층상구조의 성장거동과 이와 관련된 구조적, 전기적 특성에 대해서 집중한다. 또한 2D TMDs 물질의 전송과 통합 방법과 3차원 (3D) 패터닝(patterning) 기술을 이용한 미래 전자 장치로의 2D TMDs 물질의 적용 가능성에 대한 연구를 다룬다.

첫 번째 장에서는 대면적 화학증기전이(CVT) 방법으로 성장한 PtSe₂ 와 PtTe₂ 층의 성장거동에 대하여 관찰 및 규명하였으며, 성장거동에 따른 전기적 특성의 변화에 대하여 관찰하여 그에 미치는 영향을 규명하였다. 저온 합성 공정(400°C)에서 성장한 PtSe₂와 PtTe₂층은 초기 플래티넘 (Platinum, Pt) 막의 두께가 증가함에 따라 수평에서 수직으로의 전이를 나타낸다. 이러한 PtSe₂층과 PtTe₂ 층의 성장방향 전이는 성장 과정에서 생성된 내부 변형률에 따른 열역학적, 물리적 에너지에 따라 형성되며 투과전자현미경 (TEM)을 통한 변형률 분산 분석을 통해 정량적으로 입증하였다.

두 번째 장에서는, 물을 사용한 대면적 2D TMDs 물질의 박리와 결합에 대한 새로운 방법에 대하여 탐구하였으며, 첫 번째로 물만을 사용한 2D TMDs 물질의 박리와 다양한 기판으로의 전사에 관한 손쉽고 신뢰할 수 있는 접근 방식을 보고하였다. 이 새로운 이차원 물질의 통합 방법은 다른 화학 물질을 사용하지 않고 물만 사용하므로 재료 속성 보존 및 통합 크기 대면적화 측면에서 기존 접근 방식에 비해 뚜렷한 이점을 제공한다. 두번째로는, “수용성” 단결

정 소금 기판 위에 다양한 2D TMDs 층상 물질을 직접 성장시키고 화학적으로 무해한 방식으로 물 속으로 넣어 기판을 물에 녹게 함으로써 2D TMDs 물질만을 정확하게 박리하는데 성공하였다. 이러한 방법은 전사 기판의 종류와 모양에 구애받지 않으며, 다양한 종류의 2D TMDs 물질뿐 아니라 수직으로 정렬된 물질의 박리와 전사도 가능하게 한다. 또한 추가 성장을 위해 원래 소금 기판을 재활용할 수 있으므로 높은 공정 지속 가능성과 확장성을 확인할 수 있다. 이러한 연구를 통하여 산업적으로 요구되는 대규모에서의 다양한 구조의로의 장치를 개발하기 위한 2D TMDs 구조 물질의 적용 가능성을 확인할 수 있다.

세 번째 장에서는, 제한된 기계적 물성의 특징을 나타내는 2D TMDs 물질을 전기적, 구조적, 광학적 성질을 유지하면서 매우 큰 기계적 신축성을 나타내게 하는 3차원 구조로의 변환에 대한 연구를 보고한다. 우리는 키리가미 패터닝과 뱀 모양 패터닝의 종이 절단 예술에서 영감을 얻은 변형 기술을 사용하여 2D TMDs 물질 기반의 신축성 전자 장치를 개발하였다. 수직으로 정렬된 금속 PtTe_2 및 PtSe_2 물질은 고분자 기판에서 저온 직접 성장 방법을 사용하여 고성능 전자 히터 및 2000% 가 넘는 고신축성 전도체에 사용되었으며, 반도체 물성을 나타내는 PtSe_2 및 MoS_2 물질은 대면적 신축성 전계 효과 트랜지스터(FET) 전자 장치 및 고성능 감도를 나타내는 이산화 질소(NO_2) 가스 센서에 사용되었다. 3D 형태를 나타내


는 이러한 다기능 2D 재료의 변환은 새로운 전자 및 광전자 기술에 2D TMDs 물질의 적용 가능성에 대한 기회를 제공한다.


핵심어: 이차원 전이금속 디칼코제나이드, 화학증기전이방식, 수용성 기판, 신축성 전자장비, 키리가미 패터닝

학번: 2013-20631


APPENDIX: COPYRIGHT PERMISSIONS

Figure 1.1





Home
Help
Email Support
SangSub Han ▾



Two-dimensional flexible nanoelectronics

Author: Deji Akinwande et al
 Publication: Nature Communications
 Publisher: Springer Nature
 Date: Dec 17, 2014

Copyright © 2014, Nature Publishing Group, a division of Macmillan Publishers Limited. All Rights Reserved.

Order Completed

Thank you for your order.

This Agreement between UCF ("You") and Springer Nature ("Springer Nature") consists of your license details and the terms and conditions provided by Springer Nature and Copyright Clearance Center.

Your confirmation email will contain your order number for future reference.

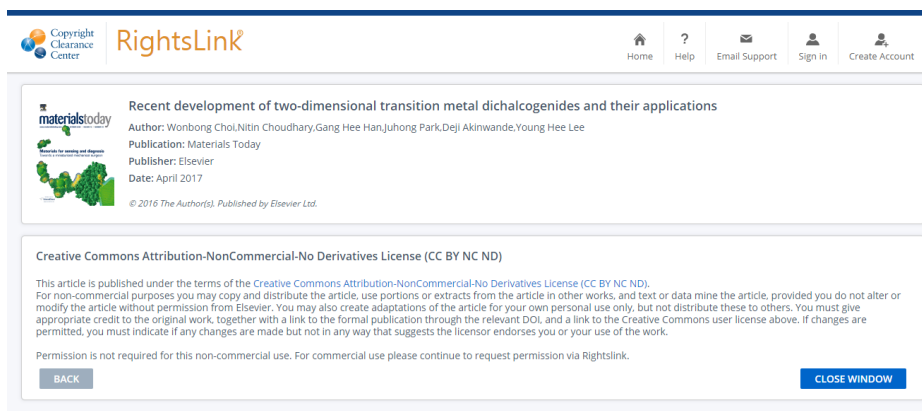
License Number 4965580560502

License date Dec 10, 2020

[Printable Details](#)

Licensed Content	Order Details
Licensed Content Publisher	Springer Nature
Licensed Content Publication	Nature Communications
Licensed Content Title	Two-dimensional flexible nanoelectronics
Licensed Content Author	Deji Akinwande et al
Licensed Content Date	Dec 17, 2014
Type of Use	Thesis/Dissertation
Requestor type	non-commercial (non-profit)
Format	print and electronic
Portion	figures/tables/illustrations
Number of figures/tables/illustrations	1
High-res required	no
Will you be translating?	no
Circulation/distribution	1 - 29

Figure 1.2



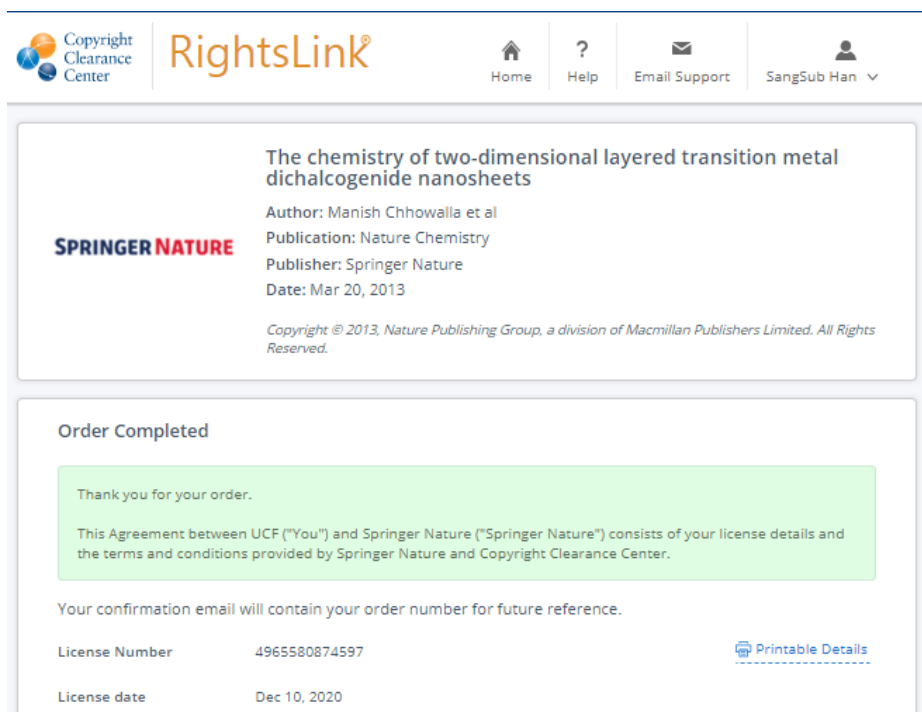
Copyright Clearance Center RightsLink® Home ? Email Support Sign In Create Account

Recent development of two-dimensional transition metal dichalcogenides and their applications
 Author: Wonbong Choi, Nitin Choudhary, Gang Hee Han, Juhong Park, Deji Akinwande, Young Hee Lee
 Publication: Materials Today
 Publisher: Elsevier
 Date: April 2017
 © 2016 The Author(s). Published by Elsevier Ltd.

Creative Commons Attribution-NonCommercial-No Derivatives License (CC BY NC ND)
 This article is published under the terms of the Creative Commons Attribution-NonCommercial-No Derivatives License (CC BY NC ND). For non-commercial purposes you may copy and distribute the article, use portions or extracts from the article in other works, and text or data mine the article, provided you do not alter or modify the article without permission from Elsevier. You may also create adaptations of the article for your own personal use only, but not distribute these to others. You must give appropriate credit to the original work, together with a link to the formal publication through the relevant DOI, and a link to the Creative Commons user license above. If changes are permitted, you must indicate if any changes are made but not in any way that suggests the licensor endorses you or your use of the work.
 Permission is not required for this non-commercial use. For commercial use please continue to request permission via Rightslink.

BACK CLOSE WINDOW

Table 1.1



Copyright Clearance Center RightsLink® Home ? Email Support SangSub Han

The chemistry of two-dimensional layered transition metal dichalcogenide nanosheets
 Author: Manish Chhowalla et al
 Publication: Nature Chemistry
 Publisher: Springer Nature
 Date: Mar 20, 2013
 Copyright © 2013, Nature Publishing Group, a division of Macmillan Publishers Limited. All Rights Reserved.

Order Completed

Thank you for your order.

This Agreement between UCF ("You") and Springer Nature ("Springer Nature") consists of your license details and the terms and conditions provided by Springer Nature and Copyright Clearance Center.

Your confirmation email will contain your order number for future reference.

License Number	4965580874597	Printable Details
License date	Dec 10, 2020	